

FUNDAMENTALS OF MATERIALS MODELLING
FOR HOT STAMPING OF UHSS PANELS WITH
GRADED PROPERTIES

by

NAN LI

A thesis submitted for the degree of Doctor of Philosophy of Imperial College London
and the Diploma of Imperial College London

Department of Mechanical Engineering
Imperial College London
November 2013

DECLARATION OF AUTHORSHIP

I, Nan Li, declare that the work presented in this thesis titled ‘fundamentals of materials modelling for hot stamping of UHSS panels with graded properties’ is my own, all else is appropriately referenced.

The copyright of this thesis rests with the author and is made available under a Creative Commons Attribution Non-Commercial No Derivatives licence. Researchers are free to copy, distribute or transmit the thesis on the condition that they attribute it, that they do not use it for commercial purposes and that they do not alter, transform or build upon it. For any reuse or redistribution, researchers must make clear to others the licence terms of this work.

ABSTRACT

The aim of this study is to develop the fundamentals of materials modelling to enable effective process control of hot stamping for forming UHSS panels with graded properties for optimised functional performance. A selective heating and press hardening strategy is adopted to grade the microstructural distribution of a press hardened component through differential heat treatment of the blank prior to forming. Comprehensive material models, to enable prediction of austenite formation and deformation behaviours of boron steel under hot forming conditions, as well as the dynamic response of a press hardened part with tailored properties in collision situations, have been developed based on experimental investigations and mechanism studies. The research work is concerned with four aspects: feasibility of the selective heating and press hardening strategy, austenite formation in boron steel during selective heating, thermo-mechanical properties of boron steel under hot stamping, and mechanical properties of boron steel with various microstructures at room temperature.

Feasibility studies for the selective heating and press hardening strategy were carried out through a designed experimental programme. A lab-scale demonstrator part was designed and relevant manufacturing and property-assessment processes were defined. A heating technique and selective-heating rigs were designed to enable certain microstructural distributions in blanks to be obtained. A hot stamping tool set was designed for forming and quenching the parts. Test pieces were formed under various heating conditions to obtain demonstrator parts having variously graded microstructures. Microstructural distributions in the as-formed parts were determined through hardness testing and microstructural observation. Ultimately, the structural performance of the parts was evaluated through bending tests.

Heat treatment tests were performed to study the formation of austenite in boron steel during selective heating. Characterisation of the effects of heating rate and temperature on transformation behavior was conducted based on the test results. A unified austenite formation model, capable of predicting full or partial austenite formation under both isothermal and non-isothermal conditions, was developed, and determined from the heat treatment test results.

Hot tensile tests were performed to study the thermo-mechanical properties of the austenite and initial phase (ferrite and pearlite) of boron steel. The viscoplastic deformation behaviours of the both phase states were analysed in terms of strain rate and temperature dependence based on the test results. A viscoplastic-damage constitutive model, capable of describing the thermo-mechanical response of boron steel in a state corresponding to hot stamping after selective heating, was proposed. Values of constants in the model for both the austenite and initial phase were calibrated from the hot tensile test results.

Dynamic and quasi-static tensile testes combined with hardness testing and microstructural observation were carried out to study the mechanical properties of press hardened boron steel with various microstructures at room temperature. Based on the results, the strain rate sensitivity of the martensite and initial phase of boron steel was characterised; the relationships between mechanical properties (true ultimate tensile strength, 0.2% proof stress, elongation, and hardness) and phase composition (volume fraction of martensite), for boron steel with various microstructures, were rationalised. Finally, a viscoplastic-damage constitutive model, capable of predicting the mechanical response of a press hardened boron steel part with graded properties being subjected to crash situations in automobiles, were developed, and determined from the test results.

ACKNOWLEDGEMENTS

First and foremost, I would like to express my deep gratitude to my supervisors Professor Jianguo Lin and Dr Daniel S. Balint for their continuous guidance, support, and encouragement throughout my PhD study. Their discipline, expertise, and inspiration have been indispensable to my growth as a researcher. I am also very grateful to Professor Trevor A. Dean of the University of Birmingham for his valuable advice and great help on my work, papers, and thesis.

Financial support from the industrial sponsor SAIC Motor UK Technical Centre is acknowledged. I would like to thank Dr Damian Dry and Mark Hillier of SAIC for their advice on my PhD project and provision of material. I am also indebted to my previous supervisor Professor Weimin Gao of Tongji University for facilitating the project and being willing to help all the time. Financial support from the ‘UK-China Scholarships for Excellence’ scheme is also acknowledged.

Sincere thanks to the technical staff of Department of Mechanical Engineering, Imperial College London: Hugh MacGillivray, Dr Leonard Wanigasooriya, Suresh Viswanathan Chettiar, Amit Choda, and Mark Holloway. Their assistance was important for the success of my experimental work. Very many thanks to my previous and current colleagues and officemates: Dr Awang Ngah, Shamsiah, Dr Qian Bai, Dr Jingqi Cai, Guicai Chen, Shouhua Chen, Thomas Dunnett, Xuetao Li, Dr Ali Mehmanparast, Dr Mohamed Saad Kamel Mohamed, Aditya Narayanan, Dr Panagiotis Sphicas, Zhutao Shao, Dr Liliang Wang, Yi Wang, Dr Xiaoyu Xi, Dr Haoliang Yang, Kailun Zheng and all who helped me and encouraged me in any respect during my PhD study. My special thanks are given to my lovely PhD-Village members: Qi Cao, Lei Ding, Ran Fei, Yeyi Liu, Yijiang Wu and Lingling Zheng. The four-year journey has not been easy, but I have been

lucky to have them accompany. I would also like to express my appreciation to Dr Mengnan Shen and Xiaofeng Ju for providing me support and strength from China.

Last but not least, I wish to express a heartfelt gratitude to my beloved parents for their endless trust, understanding, patience, and support. They hope me around, but they set me free and taught me to be strong. Without this, my PhD would not have been possible. Thank you, my father and mother, I own you so much.

NOMENCLATURE

α	Ferrite
θ	Cementite
ψ	Initial phase (ferrite and pearlite)
γ	Austenite
A_{e1}, A_{e3}	Temperature to start and complete austenite formation under equilibrium conditions, K
A_{c1}, A_{c3}	Temperature to start and complete austenite formation during continuous heating, K
v	Relative volume change
$v_{\psi0}, v_{\psi}(T)$	Relative volume change of the initial phase at 873K and at any temperature
$v_{\gamma0}, v_{\gamma}(T)$	Relative volume change of austenite at 873K and at any temperature
C_{ψ}, C_{γ}	Thermal expansion coefficient of the initial phase and austenite, /K
\dot{N}	Austenite nucleation rate
\dot{G}	Austenite growth rate
R	Gas constant, J/ mol·K
T	Absolute temperature, K
\dot{T}	Heating rate, K/s
T_x	Temperature corresponding to certain volume fraction of austenite, K

e.g. $T_{50\%}$ is the temperature when volume fraction of austenite reaches 50%

t Instantaneous time, s (origin: time at temperature of 873K)

t_{Ac1} Time to start austenite formation, s (same origin as t)

t_x Time corresponding to certain volume fraction of austenite, s (same origin as t)

e.g. $t_{80\%}$ is the time when volume fraction of austenite reaches 80%

Δt Soaking time increment, s

Δt_{x1-x2} Time to increase volume fraction of austenite from $x1$ to $x2$ during soaking, s

e.g. $\Delta t_{80\%f_s-90\%f_s}$ is the time to increase volume fraction of austenite from 80% of f_s to 90% of f_s during soaking

$\Delta t'$ Time increment during continuous heating, s

$\Delta t'_{Ac1-X}$ Time increment from starting austenite formation to reaching certain volume fraction of austenite during continuous heating, s

f_M Volume fraction of martensite

f_A Volume fraction of austenite

f'_A Extended volume fraction of austenite

f_{As} Saturated volume fraction of austenite

f_P Volume fraction of pearlite

N Nuclei quantity of austenite per unit sample volume

Q_N	Activation energy related to nucleation of austenite, J/mol
\dot{v}	Volume growth rate of an austenite nucleus
V_e	Extended volume of austenite in a unit of real sample volume
\dot{V}_e	Growth rate of the extended volume of austenite
Q_v	Activation energy related to volume growth of austenite, J/mol
m, n	Parameters related to the impingement mechanism of austenitization
T_m	Melting temperature, K
σ_E, σ	Engineering stress and true stress/flow stress, MPa
$\varepsilon_E, \varepsilon_T$	Engineering strain and true strain
ε_f	True strain to failure/elongation
σ_{UTS}	True ultimate tensile strength, MPa
$\sigma_{0.2\%}$	0.2% proof stress, MPa
σ_v	Viscous stress, MPa
$\varepsilon^T, \dot{\varepsilon}^T$	Total (true) strain and total (true) strain rate
$\varepsilon^P, \dot{\varepsilon}^P$	Plastic (true) strain and plastic(true) strain rate
$\varepsilon^E, \dot{\varepsilon}^E$	Elastic (true) strain and elastic (true) strain rate
E	Young's modulus of elasticity, MPa
H	Isotropic strain hardening, MPa
k	Initial yield stress, MPa
ρ	Dislocation density

ρ_0	Initial dislocation density of material
L	Mean dislocation free path
$\bar{\rho}$	Normalised dislocation density
$\omega, \dot{\omega}$	Damage and damage evolution rate
n_V	Viscous exponent
n_R	Isotropic hardening exponent
m'	Parameter related to strain rate hardening
Q_E	Activation energy related to elastic modulus, J/mol
Q_k	Activation energy related to initial plastic slip, J/mol
Q_K, Q_n	Activation energy related to viscosity , J/mol
Q_B	Activation energy related to isotropic hardening, J/mol
Q_β	Activation energy related to damage, J/mol
A	Parameter/material constant related to evolution of dislocation density
B	Parameter related to isotropic hardening, MPa
C	Parameter related to static recovery of dislocation density
K	Parameter related to viscous stress, MPa
β	Parameter related to damage
$A_\#, B_\#, C_\#$	Material constants
$\gamma_\#, \beta_\#, \phi_\#$	Material constants
k_0, k_x, K_0, K_x	Material constants, MPa

m_0, n_0, n_{v0}, v_0	Material constants
E_0	Material constant, MPa
N_0, G_0	Material constants

CONTENTS

DECLARATION OF AUTHORSHIP.....	I
ABSTRACT	II
ACKNOWLEDGEMENTS.....	IV
NOMENCLATURE	VI
CONTENTS	XI
LIST OF FIGURES	XVII
LIST OF TABLES.....	XXIII
CHAPTER 1 INTRODUCTION	1
1.1 Project driving force	1
1.1.1 Automotive industrial background	1
1.1.2 Hot stamping of automotive UHSS parts	2
1.1.3 New strategies and challenges in hot stamping	6
1.2 Aim and objectives of research	8
CHAPTER 2 HOT STAMPING TECHNOLOGIES AND DEVELOPMENT	10
2.1 Introduction to hot stamping	10
2.1.1 Boron steel – 22MnB5	11
2.1.2 Process parameters.....	17
2.1.3 Advantages and limitations of conventional hot stamping processes.....	19
2.2 Tailored solutions in hot stamping	21
2.2.1 Manufacturing of hot stamped parts with tailored properties	21
2.2.1.1 Additional operations to hot stamping.....	21

2.2.1.2 Selective heat treatment strategies integrated in hot stamping	24
2.2.2 Technologies for process control of thermal conditions	27
2.2.2.1 Selective cooling solutions	27
2.2.2.2 Advanced techniques for selective heating.....	29
2.2.3 Analysis of the selective heating and press hardening strategy	32
2.3 Microstructural control during heating.....	34
2.3.1 Studies on austenite formation.....	34
2.3.2 Modelling of austenite formation	35
2.4 Final properties of hot stamped panels.....	36
2.5 Summary	39
 CHAPTER 3 FEASIBILITY STUDIES FOR THE SELECTIVE HEATING AND PRESS	
HARDENING STRATEGY	41
3.1 Introduction	41
3.2 Experimental design.....	41
3.2.1 Concept illustration.....	41
3.2.2 Material and demonstrator part.....	43
3.2.3 Test programme	43
3.3 Heating technique.....	44
3.4 Hot stamping	49
3.4.1 Design of hot stamping tool set	49
3.4.2 Hot stamping experiments	52
3.5 Microstructural distribution analysis.....	53
3.5.1 Hardness testing.....	53
3.5.2 Microstructural observation.....	55

3.5.3 Discussion	56
3.6 Structural performance assessment	57
3.6.1 Three point bending tests	57
3.6.2 Results and discussion	57
3.7 Summary	59
CHAPTER 4 EXPERIMENTAL PROGRAMME OF FUNDAMENTAL TESTS	60
4.1 Introduction	60
4.2 Austenite formation	60
4.2.1 Test equipment and specimen design	61
4.2.2 Test programme	63
4.3 Thermo-mechanical properties at elevated temperatures	64
4.3.1 Test equipment and programme	64
4.3.2 Specimen design and test procedure	67
4.3.2.1 Specimen design	67
4.3.2.2 Temperature gradients in the longitudinal direction	67
4.3.2.3 Control of strain rate	68
4.4 Mechanical properties at room temperature	71
4.4.1 The first group: tensile testing over a range of strain rates	71
4.4.1.1 Design of experiment and specimen	72
4.4.1.2 Specimen preparation	74
4.4.1.3 Set-up and procedure for quasi-static tensile testing	75
4.4.1.4 Set-up and procedure for dynamic tensile testing	78
4.4.2 The second group: tensile testing over a series of phase compositions	81

4.4.2.1 Specimen design and preparation	81
4.4.2.2 Test procedure	83
CHAPTER 5 EXPERIMENTAL RESULTS AND DISCUSSION.....	84
5.1 Introduction	84
5.2 Austenite formation.....	84
5.2.1 Mechanisms of austenite formation in hypoeutectoid steels	85
5.2.2 Experimental results	87
5.2.3 Analysis of full austenite formation.....	92
5.2.3.1 Effects of heating rate on non-isothermal austenite formation.....	93
5.2.3.2 Effects of heating rate on isothermal austenite formation	97
5.2.4 Analysis of intercritical annealing	101
5.2.4.1 Saturated volume fraction.....	101
5.2.4.2 Effects of temperature on isothermal austenite formation.....	102
5.3 Thermo-mechanical properties of boron steels under hot stamping conditions.....	105
5.3.1 Results: flow stress-strain curves.....	105
5.3.1.1 Strain rate and temperature dependence of austenite.....	105
5.3.1.2 Strain rate and temperature dependence of initial phase	108
5.3.2 Characterisation of flow stress response.....	109
5.3.2.1 Effects of strain rate.....	110
5.3.2.2 Effects of temperature.....	112
5.4 Mechanical properties of boron steels at room temperature	113
5.4.1 Dynamic tensile behaviour of the martensite and initial phase for boron steel	113
5.4.1.1 Results: flow stress-strain curves.....	113

5.4.1.2 Strain rate sensitivity of the phase states	115
5.4.2 Effects of microstructure on tensile behaviour of boron steel	116
5.4.2.1 Relationships between mechanical properties and phase composition.....	116
5.4.2.2 Effects of phase composition on tensile properties	117
5.5 Summary	120
CHAPTER 6 MATERIALS MODELLING	122
6.1 Introduction	122
6.2 Development of austenite formation model for the boron steel during selective heating..	122
6.2.1 Model development	123
6.2.1.1 Extended volume of austenite.....	123
6.2.1.2 Real volume fraction of austenite	126
6.2.1.3 Saturated volume fraction of austenite	128
6.2.2 Formulation of unified constitutive equations	129
6.2.3 Determination of the equations.....	130
6.2.3.1 Calibration of the constants from experimental data	130
6.2.3.2 Validation and analysis.....	133
6.3 Viscoplastic-damage constitutive model.....	135
6.3.1 Flow rule.....	136
6.3.2 Isotropic work hardening	138
6.3.3 Evolution of dislocation density	139
6.3.4 Evolution of damage.....	140
6.3.5 Modified flow rule and Hooke's law	142
6.4 Unified viscoplastic-damage constitutive equations for boron steels under hot stamping conditions	143

6.4.1 Formulation of unified viscoplastic-damage constitutive equations	143
6.4.2 Determination of the equations.....	145
6.4.2.1 Calibration of the constants from experimental data	145
6.4.2.2 Analysis on the modelling results	150
6.5 Unified viscoplastic-damage constitutive equations for multiphase boron steels for crashworthiness analysis	151
6.5.1 Formulation of unified viscoplastic-damage constitutive equations	151
6.5.2 Determination of the equations.....	153
6.6 Summary	155
CHAPTER 7 CONCLUSIONS AND SUGGESTIONS FOR FUTURE WORK	156
7.1 Conclusions	156
7.1.1 Feasibility of the selective heating and press hardening strategy	156
7.1.2 Austenite formation in boron steel during selective heating	157
7.1.3 Thermo-mechanical properties of boron steel under hot stamping	159
7.1.4 Mechanical properties of boron steel with various microstructures at room temperature	160
7.2 Suggestions for future work	161
REFERENCES	164
APPENDIX 1 CALCULATION OF AUSTENITE VOLUME FRACTION	177
APPENDIX 2 STRAIN CORRECTION AT NECKING STAGE	180

LIST OF FIGURES

Figure 1.1 Mechanical properties of boron steel before, during, and after hot stamping, compared with other types of AHSS steels and Mild steels used for cold forming [15, 27]	4
Figure 1.2 Forming capabilities of different forming techniques for automotive applications, in terms of material strength and geometric complexity of formed parts [27]	5
Figure 1.3 Components manufactured by hot stamping (press hardening) in the Body-in-White (BIW) of the 3rd generation of the ultra-light Audi A3, utilising different types of steel [30]	6
Figure 2.1 Hot stamping processes: (a) direct method (b) indirect method [53]	11
Figure 2.2 Experimental data and numerical predictions of 22MnB5 flow behaviours at different temperatures from 923K to 1173K at the strain rate of (a) 0.1/s and (b) 10/s [22]	14
Figure 2.3 Experimental (symbols) and numerical predicted (solid curves) flow behaviours of boron steel (USIBOR 1500P, ArcelorMittal) at (a) different temperatures from 873K to 1073K (strain rate: 0.1/s) and (b) different strain rates from 0.01/s to 10/s (deformation temperature: 973K) [16]	15
Figure 2.4 CCT diagram of a typical 22MnB5 boron steel (USIBOR 1500P, ArcelorMittal) under the undeformed (solid lines) [24] and deformed (dashed lines) states	16
Figure 2.5 Schematic of the typical temperature profile of blanks in hot stamping processes.....	18
Figure 2.6 Schematics illustrating the manufacturing of hot stamped B-pillars from (a) tailored welded blanks (TWB) [29, 74], and (b) tailored rolled blanks (TRB) [79, 80].....	22
Figure 2.7 hot stamping of a B-Pillar with graded microstructures by selective heat treatment: (a) Image of a hot stamped B-pillar being partially hardened [40], with a temperature profile of a selective cooling process in a continuous cooling transformation (CCT) diagram (b) An as-formed B-pillar with graded properties, and the typical tensile properties of the martensite and	

initial phase of boron steel (c) Image of a blank being partially austenitized, with a temperature profile of a selective heating process in a continuous heating transformation (CHT) diagram.....	25
Figure 2.8 Textures on die surfaces [86]	28
Figure 2.9 Principle of selective heating of a steel sheet using bypass resistance heating [35] ...	30
Figure 2.10 Principle of contact heating [90]	31
Figure 2.11 (a) Ultimate tensile strength (σ_{UTS}) and 0.2% yield stress ($\sigma_{0.2\%}$) and (b) Uniform elongation versus Vickers hardness from the quasi-static tension tests conducted at a strain rate of 0.003 /s (The error bars represent +/- the standard deviation of repeated test results) [37]	38
Figure 3.1 Schematics illustrating the manufacturing process and experimentation for function assessment (a) Selective heating of the work-piece (b) An as-formed part after hot stamping and cold die quenching (c) Three point bending of the as-formed part.....	42
Figure 3.2 Cross-section of a demonstrator beam (dimensions are in mm)	43
Figure 3.3 Selective heating technique (a) Set-up of facilities for selective heating and temperature measurement (b) 3-D diagram of the selective heating rig (c) Location of thermocouples attached to a work-piece (dimensions in the figure are in mm)	45
Figure 3.4 Temperature profiles of different positions of a work-piece under selective heating conditions: (a) S-60mm, (b) S-100mm	48
Figure 3.5 Temperature profiles for 4 different test conditions.....	49
Figure 3.6 Schematics illustrating the working mechanism of the tool set and material flow of the work-piece (a) Start of forming (b) during forming, middle groove has been formed (c) final stage of forming	51
Figure 3.7 Isometric view of the hot stamping and cold die quenching tool set	51
Figure 3.8 Set-up of facilities for hot stamping experiment	52
Figure 3.9 View of the cross-section of a formed product	53
Figure 3.10 Hardness distribution through a cross-section of an S-320mm as-formed part	54

Figure 3.11 Hardness distributions along the longitudinal direction of S-60mm and S-100mm as-formed parts	55
Figure 3.12 Typical SEM micrographs of boron steel from different microstructure zones (sampled from flange edge) of an S-100mm as-formed part.....	56
Figure 3.13 Failure modes under bending for boron steel parts having different microstructural topographies.....	58
Figure 3.14 Load bearing performance of boron steel parts having different microstructural topographies: (a) Load deflection curve (b) Stroke at the onset of instability against the proportional length of full martensite phase	58
Figure 4.1 Gleeble 3800 thermo-mechanical materials simulator	61
Figure 4.2 Test set-up and specimen design	62
Figure 4.3 Test programme of heat treatments with different heating rates and soaking temperatures.....	63
Figure 4.4 Temperature-time profiles for isothermal tensile testing of boron steels in both austenite (soaked at 1173K) and the initial phase (soaked at 923K)	65
Figure 4.5 Specimen design (dimensions are in mm) with schematic dilatometer and three pairs of thermocouples attached	67
Figure 4.6 Temperature distributions along the specimen in the longitudinal direction at different testing temperatures	68
Figure 4.7 Deformation on a fractured specimen	70
Figure 4.8 Specimen design (dimensions are in mm) with a schematic strain gauge attached	73
Figure 4.9 Set-up of facilities and specimen for low rate tensile testing	76
Figure 4.10 Set-up of facilities and specimen for dynamic tensile testing	77
Figure 4.11 Design of specimens (dimensions are in mm) for quasi-static tensile testing (solid line) and Gleeble heat treatments (dash line).....	82

Figure 4.12 Test-pieces for different testing.....	83
Figure 5.1 The formation of austenite in a hypoeutectoid steel (containing less than 0.76 wt% C)	85
Figure 5.2 Experimental curves showing the width change of specimen against (a) temperature and (b) time during the heat treatment process (heating rate: 5K/s, soaking temperature: 1173K)	89
Figure 5.3 Width changes of specimens tested at different (a) heating rates (soaking temperature: 1173K), and (b) soaking temperatures (heating rate: 5K/s).....	90
Figure 5.4 Variations of volume fraction of austenite with temperature and time for different (a) heating rates (soaking temperature: 1173K) and (b) soaking temperatures (heating rate: 5K/s) ..	92
Figure 5.5 Continuous heating transformation (CHT) diagram	94
Figure 5.6 Effects of heating rate on austenite formation under continuous heating conditions...	95
Figure 5.7 Effects of heating rate on the transformation time to increase austenite volume fraction by 5% from 80%, 85% and 90% during soaking at 1173K.....	98
Figure 5.8 Volume fractions of austenite for different heating rates with time normalised by the soaking time increments for different austenite volume fractions, during soaking at 1173K	100
Figure 5.9 Saturated volume fractions of austenite at different soaking temperatures.....	101
Figure 5.10 Effects of soaking temperature on the transformation time to increase austenite volume fraction by 10% of f_{As} from 80% of f_{As}	103
Figure 5.11 Evolution curves of austenite volume fraction for different temperatures under isothermal transformation conditions	104
Figure 5.12 Experimental flow stress-strain relationships for austenite for different strain rates at a deformation temperature of 973K.....	105
Figure 5.13 Experimental flow stress-strain relationships for austenite for different deformation temperatures (designed strain rate: 0.50/s)	107

Figure 5.14 Experimental flow stress-strain relationships of the initial phase for different strain rates at a deformation temperature of 923 K	108
Figure 5.15 Experimental flow stress-strain relationships of the initial phase for different deformation temperatures (designed strain rate: 0.50/s).....	109
Figure 5.16 Flow stress at different strain levels (0.005, 0.05, and 0.1) for different strain rates	111
Figure 5.17 Flow stress at different strain levels (0.005, 0.05, and 0.1) for different deformation temperatures (designed strain rate: 0.50/s)	112
Figure 5.18 True stress-strain curves of the martensite and initial phase of boron steels for different strain rates tested at room temperature	114
Figure 5.19 Effects of strain rate (0.001/s, 0.05/s, 5/s, 50/s, 200/s, and 500/s) on the tensile properties of the martensite and initial phase of the boron steel.....	116
Figure 5.20 The relationships of true ultimate tensile strength and martensite volume fraction with hardness for heated treated boron steel with various phase compositions	117
Figure 5.21 True stress-strain curves of heat treated boron steel with various volume fractions of martensite (quasi-static tests for the strain rate of 0.001/s at room temperature)	118
Figure 5.22 Effects of martensite volume fraction on tensile properties of heat treated boron steels (quasi-static tests for the strain rate of 0.001/s at room temperature).....	119
Figure 6.1 Comparison of experimental (symbols) and computed (solid curve) saturated volume fraction of austenite at intercritical annealing temperatures using equation (6.21)	131
Figure 6.2 Comparison of experimental (symbols) and numerical integrated (solid curves) volume fractions of austenite formation under different heating conditions for calibration	132
Figure 6.3 Comparison of experimental (symbols) and predicted (solid curves) volume fractions of austenite formation for validation (Heating rate: 2K/s, soaking temperature: 1273K)	133

Figure 6.4 Comparison of experimental (symbols) and predicted (solid curves) continuous heating transformation (CHT) data, which are shown for different volume fractions of austenite (10%–70%) with various heating rates (1–25K/s).....	134
Figure 6.5 Comparison of experimental (symbols) and predicted (solid line) relationships of time increment to attain 80%–90% austenite volume fraction under an isothermal condition (1173K) with various heating rates (1–25K/s).....	135
Figure 6.6 Flow stress-strain responses of viscoplastic solids.....	136
Figure 6.7 Comparison of experimental (symbols) and numerical integrated (solid curves) true stress-strain curves for austenite at elevated temperatures	148
Figure 6.8 Comparison of experimental (symbols) and numerical integrated (solid curves) true stress-strain curves for the initial phase at elevated temperatures	149
Figure 6.9 Comparison of experimental (symbols) and numerical integrated (solid curves) true stress-strain curves for boron steels with various phase compositions at room temperature	154
Figure A1.1 Conversion from width change curve to relative volume change curve	178
Figure A2.1 Strain correction method at necking stage.....	181
Figure A2.2 An example true stress-strain curve showing the correction at necking stage	182

LIST OF TABLES

Table 2.1 Chemical composition of a typical 22MnB5 boron steel (mass in % min-max) [55] ...	12
Table 2.2 Mechanical properties of 22MnB5 boron steels [20, 21, 54, 55]	12
Table 3.1 Chemical composition (Max value - ladle analysis in %) [21].....	43
Table 3.2 Test programme ('√' represents the selected test conditions)	44
Table 4.1 Test programme ('√' represents the selected test conditions)	66
Table 4.2 Matrix of test programme and facilities.....	74
Table 6.1 Material constants for equations (6.17) – (6.23).....	133
Table 6.2 Material constants for equations (6.38) – (6.49) for the austenite and initial phase of boron steels	147
Table 6.3 Temperature dependent parameters for the austenite and initial phase of boron steels	150
Table 6.4 Material constants for equations (6.50) – (6.59).....	155

CHAPTER 1 INTRODUCTION

1.1 Project driving force

1.1.1 Automotive industrial background

A huge global challenge that the modern automotive industry is facing as of today is to improve energy efficiency and accordingly reduce environmental pollution from vehicle emissions. In the European Union (EU), to help consumers choose vehicles with low fuel consumption, a directive 1999/94/EC was issued in December 1999, which ensures useful information on fuel consumption and carbon dioxide (CO₂) emissions of new passenger cars is available to potential buyers [1]. In the United Kingdom, it came into force in November 2001 [2]. Since cars are responsible for around 12% of total EU emissions of CO₂, the main greenhouse gas, EU legislation adopted in 2009 sets mandatory targets for new cars, to achieve 18% and 40% of emission reduction by 2015 and 2020 respectively [3]. Also, in the United States, the Environmental Protection Agency (EPA) and National Highway Traffic Safety Administration (NHTSA) issued a joint final rule in May 2011, establishing new requirements for a fuel economy and environment label that is mandatory for all new passenger cars and trucks starting with model year 2013 [4]. In this context, lightweight technology plays a key role.

Another critical functional element for the design of modern car body structures is safety [5]. Significant steps towards improved protection of occupants of cars have been made since 1990s [6]. A study in the United Kingdom concluded that improved vehicle crash protection (also known as passive safety) for car occupants and pedestrians would have the greatest effect, out of all new policies under consideration, in reducing road casualties in Great Britain [7]. Also, a review by the European Transport Safety Council estimated that improved standards for crash

protection could reduce deaths and serious injuries on European roads by as much as 20% [6]. As a result, both legislative standards and market forces, produced by different authorities on a global scale such as the United Nations Economic Commission for Europe, Insurance Institute for Highway Safety (IIHS) and New Car Assessment Program (NCAP) in the United States, are making increasingly tight requirements on the vehicle crash protection. The concept of ‘crashworthiness’, termed as the ability of a structure to protect its occupants during an impact, has been well understood and incorporated into current car design [6]. The most straightforward and effective solution to improve crashworthiness is increasing the strength and ability to absorb energy of safety components.

The apparent contradictory requirements for reducing weight and increasing crashworthiness have greatly stimulated technological innovation in materials and manufacturing processes. As a consequence, lightweight alloys such as aluminium and magnesium and high yield strength steels such as advanced high strength steels (AHSS), are being used and accordingly, new forming techniques, have been significantly developed [8-12]. Nevertheless, steel, because its strength has been improved at a relatively low cost, is still the dominant material adopted for manufacturing automobiles nowadays [13, 14].

1.1.2 Hot stamping of automotive UHSS parts

According to metallurgical designation, automotive steels can be classified into [15]:

- Low-strength steels (LSS), such as interstitial-free (IF) and mild steels;
- Conventional high strength steels (HSS), such as carbon-manganese (CM), bake hardenable (BH), and high-strength, low-alloy steels (HSLA);
- Advanced high strength steels (AHSS), such as dual phase (DP), transformation-induced plasticity (TRIP), complex phase (CP), and martensitic steels (M).

Different from conventional HSS, which are usually hardened by solid solution, precipitation or grain refining, the AHSS are hardened by phase transformation [16]. For example, martensitic steel (M) is produced by fast quenching from austenite temperature to obtain lath martensite, and shows the ultra-high tensile strength level, typically between 900MPa–1500 MPa or even higher [17]. Normally, this type of steel is termed as ultra-high strength steels (UHSS).

Because of its high yield strength UHSS sheet can be used in thinner gauges than lower strength steel, whilst retaining structural rigidity and strength. Therefore, it can be used to lighten the weight of car bodies leading to reduced fuel consumption and enhanced passenger safety. However, forming UHSS at room temperature is limited by low formability and considerable spring-back [18, 19]. Thereby, hot stamping (also termed as press hardening) of quenchable steel sheets for ultra-high strength components has been developed and widely used as an effective solution to the problem.

Boron steel, as an alloy with splendid harden ability, is adopted for press hardening [20]. As shown in Figure 1.1, the ultimate tensile strength (UTS) and elongation of typical as-delivered boron steel lie between those of DP 450 and DP 600, which are about 550MPa and 20%, respectively [21]. When it is heated to full austenitization, the flow stress dramatically drops, and the ductility jumps to about 40%–50% [22-24]. This enables austenitic boron steel sheets to be formed with remarkably reduced forming load, consequently minimised spring-back, and greatly improved formability [18]. By quenching within cold dies in the same operation, the deformed boron steel transforms from austenitic phase to martensite. Thus, UHSS parts having a tensile strength of approximately 1500 MPa are obtained [21]. By contrast, for other cold formed AHSS steels, high forming forces are needed to achieve plastic deformation, and large spring-back and excessive tool wear arise as a consequence [25, 26]. In addition, due to limited formability, conventional cold forming of high strength steels is limited to the production of relatively simple

geometries [25]. Figure 1.2 summarises the forming capabilities of different forming techniques used in car body manufacturing, in terms of achievable strength and geometries of formed parts. Again, hot stamping shows the unmatched ability to produce highly complicated components with ultra-high strength.

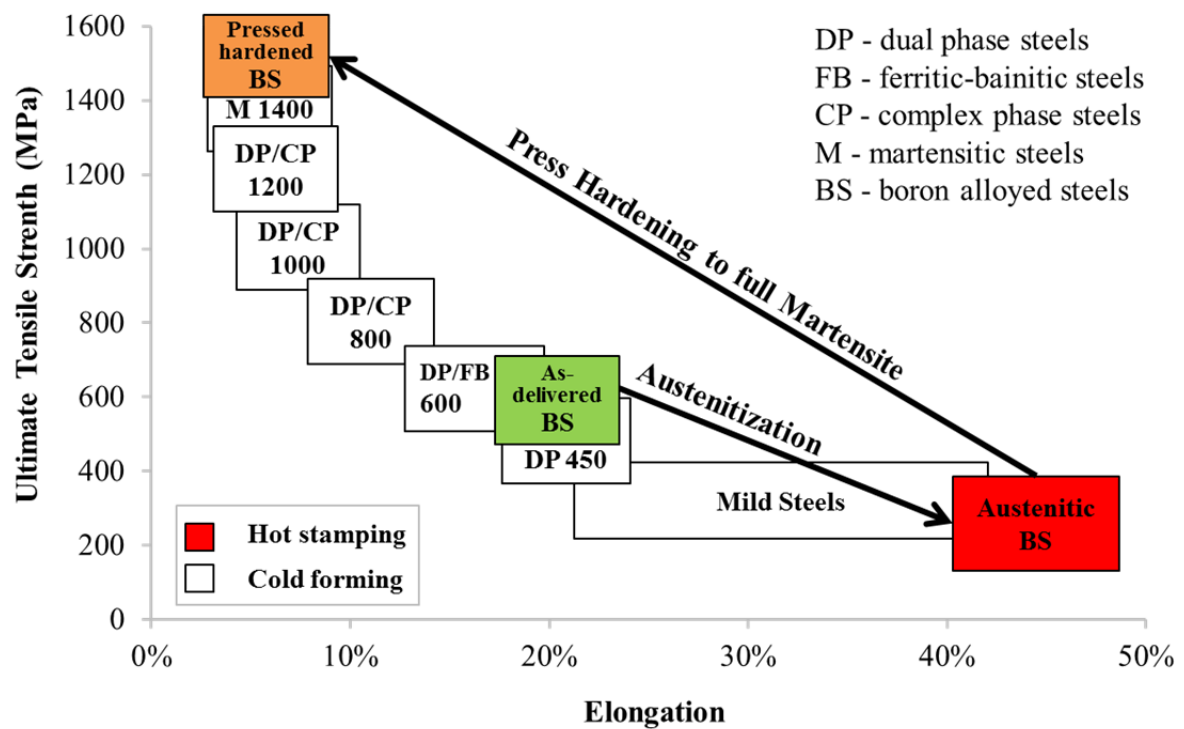


Figure 1.1 Mechanical properties of boron steel before, during, and after hot stamping, compared with other types of AHSS steels and Mild steels used for cold forming [15, 27]

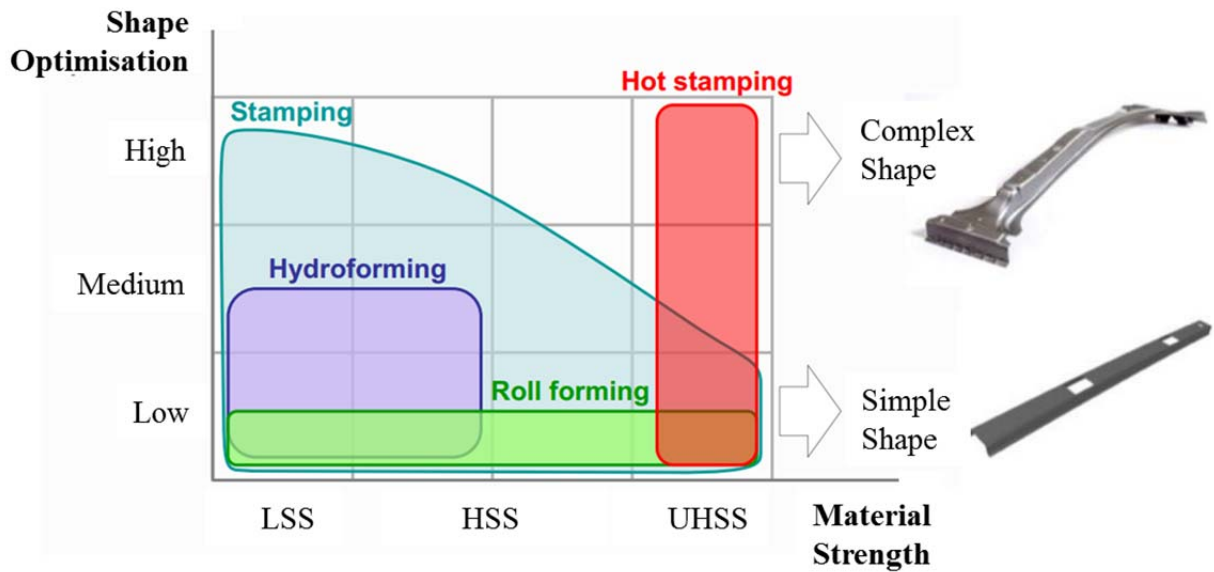


Figure 1.2 Forming capabilities of different forming techniques for automotive applications, in terms of material strength and geometric complexity of formed parts [27]

Due to its outstanding advantages, the adoption of hot stamping has been experiencing an exponential increase, coming from 3 million parts per year in 1987 to 8 million parts per year in 1997 to 95 million parts per year in 2007, and is expected to achieve 450 million parts per year in 2013 [28, 29]. At the same time, as the technology evolved, forming more complex geometries has been realised. For example, transmission tunnels can be formed by using complex hot stamping tools with multiple-point hydraulic cushions. Thereby, the number of hot stamped parts per vehicle has increased from 4 in the 1990s to 20–30 today [28], and 20% body weight of some vehicles is composed of press hardened steel. One example is the 3rd generation of the Audi A3 developed for ultra-light design in 2012, in which the mass percent of boron steel is 21.7%. The Body-in-White (BIW) of this model is illustrated in Figure 1.3, showing the hot stamped UHSS components. These are mainly safety relevant components, such as roof rail reinforcements, sill reinforcements, and B-pillars. The proportions of different types of automotive steels adopted in the BIW are also given, where hot stamped UHSS accounts for 26.4%.

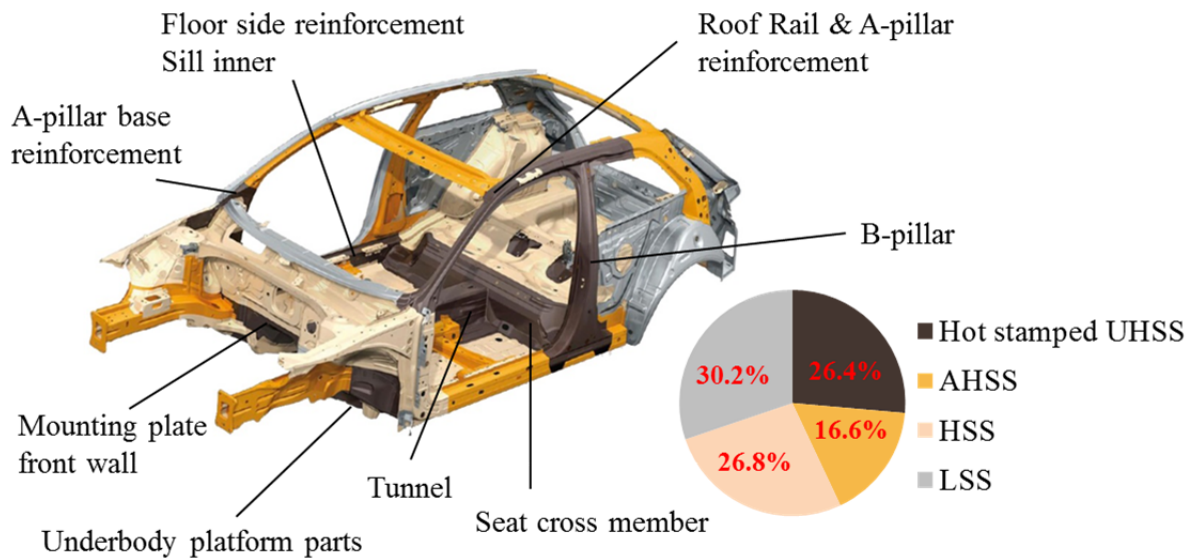


Figure 1.3 Components manufactured by hot stamping (press hardening) in the Body-in-White (BIW) of the 3rd generation of the ultra-light Audi A3, utilising different types of steel [30]

1.1.3 New strategies and challenges in hot stamping

Since a car body is a complex structure subject to complicated load situations, increasing the strength of a whole component uniformly does not always produce the optimum condition [5]. Now, great attention is being paid to developing new strategies in hot stamping, so as to produce parts with tailored distribution of mechanical properties, which introduces the potential for making parts conforming more fully to functional requirements [31-33]. For example, in safety critical beams, instead of utilising a full martensite phase, soft regions of ductile phases, such as ferrite and pearlite, can be incorporated to enhance energy absorption or tune crash deceleration pulses [31]. This is a concept about optimising structural performance by means of microstructural design, which can be realised by controlling thermal conditions, during heating or quenching, in hot stamping processes. To implement the concept for functional-optimisation-driven forming, process control analysis based on computer simulation is an invaluable tool and comprehensive material models to describe the behaviour of boron steel under forming

conditions and crash situations in automobiles are vital. To establish material models for simulation, knowledge of fundamentals of phase transformation kinetics and deformation mechanisms of boron steel in hot stamping, as well as the mechanical properties of boron steel in various microstructural states after hot stamping is essential.

In recently years, there has been great interest in forming tailored parts through selective quenching strategy [12, 34-40]. As a result, extensive studies have been carried out on austenite decomposition in boron steel during cooling [41, 42]. However, because a long cooling time is required to achieve ductile phases, there is an intrinsic conflict with the industrial requirement for short cycle times. This shortcoming can be overcome by another strategy, which is termed as selective heating and press hardening and is investigated in this study. In the operation, a blank is heated under tailored thermal conditions, which enables part of the steel to be fully or partially austenitized and the other part with its phase untransformed. Subsequently, the blank is formed and quickly quenched in cold dies, as for conventional hot stamping operations. Thus, a part with graded microstructure can be formed without sacrificing production efficiency, where the fraction and distribution of martensite in the as-formed part is determined by the extent of austenitization.

The selective heating and press hardening strategy is a promising technology for hot stamping, about which systematic studies have not yet been undertaken. Austenite formation in boron steel, a key aspect of this new strategy, has not drawn much attention compared with its decomposition [43, 44]. In addition, deformation in this strategy involves boron steel in various phase states rather than only austenite, as in the conventional process, yet no published work on the thermo-mechanical properties of boron steel in ferritic/pearlitic state under hot stamping conditions has been found. Therefore, there is large gap of knowledge to fill for the effective control of the selective heating and press hardening process. Moreover, only few studies have been conducted

on the mechanical properties of as-formed boron steels [45, 46], and a literature search has revealed no developed material model or characterisation linked to heating condition. An efficient structural optimisation cannot be realised unless the relationship between mechanical properties of as-formed boron steels and the corresponding microstructures achieved by certain thermal conditions is quantitatively determined.

1.2 Aim and objectives of research

The aim of this research is to develop fundamental material models, to enable effective process control of hot stamping, by adopting selective heating and press hardening strategy, for forming UHSS panels with graded properties for optimised functional performance. To realise this goal, four objectives need to be achieved:

- Validate the selective heating and press hardening strategy and demonstrate its potential for structural optimisation.
- Gain a better understanding of the kinetics of the austenite formation in boron steels, and evaluate the influence of heating rate and soaking temperature on the progress. Based on these, develop a set of unified equations which can effectively describe the austenite formation in boron steel, under both non-isothermal and isothermal conditions, within or above intercritical temperatures, for hot stamping processes.
- Characterise the effects of temperature and strain rate on deformation of boron steel in a state corresponding to hot stamping after selective heating, and develop unified constitutive models for both the austenite and initial phase (ferrite and pearlite) of boron steel under hot stamping conditions.

- Characterise stress-strain relationships for boron steel having various microstructures under various strain rates at room temperature, so as to develop a unified constitutive model which is capable of predicting the mechanical response of press-hardened boron steel parts with graded microstructures being subjected to crash situations in automobiles.

CHAPTER 2 HOT STAMPING TECHNOLOGIES AND DEVELOPMENT

2.1 Introduction to hot stamping

Hot forming and hardening of steel is not a new invention. The technology was used in China from the Tang Dynasty (618-907) for producing swords [47]. A skilled smith was able to create complex forms and also harden the detail in water or oil [48]. The hot stamping and cold die quenching process (termed hot stamping for short or press hardening) was invented and industrialised 40 years ago in Sweden [49]. It was patented in 1974 by a local Swedish steel works, Norrbottens Järnverk AB (NJA) which later merged into the Swedish Steel AB (SSAB), to manufacture products with high strength and wear resistance, such as shovel blades, cutting knives for lawn-mowers, cutting discs for stone cutting, etc. [48, 49] This technology has been verified and further developed at Luleå University of Technology from 1975, with their first research project calibrated with NJA and Volvo Truck. The first press hardened component on automobiles were intrusion door beams with reduced gauge and ultra-high strength, adopted by Saab Automobile AB for their year model Saab 9000 in 1984 [48]. In the next three decades, due to the advantages in meeting light weight and safety requirements, the press hardening technology has experienced tremendous development in global in automotive applications [19, 29, 50, 51], as described in chapter 1.

Conventional hot stamping processes can be classified into two main variants: direct and indirect [19, 52]. Figure 2.1 schematically presents the production lines of the two hot stamping methods. In direct hot stamping, the main method being used, as-delivered hardenable boron steel blanks cut from a coil are heated over austenitization temperature in a furnace, and subsequently

transferred to a press by an automated system, stamped and simultaneously quenched in closed cold dies. Taken out from the press, the as-formed parts are usually trimmed to obtain the net shape. In the indirect method, blanks are firstly cold preformed near to their final shapes; then, the preformed parts are heat treated for austenitization, followed by calibration and quenching in the pressing operation. The additional forming step in this method is to extend the forming limits for highly complex components which are not achievable through direct hot stamping processes [52, 53].

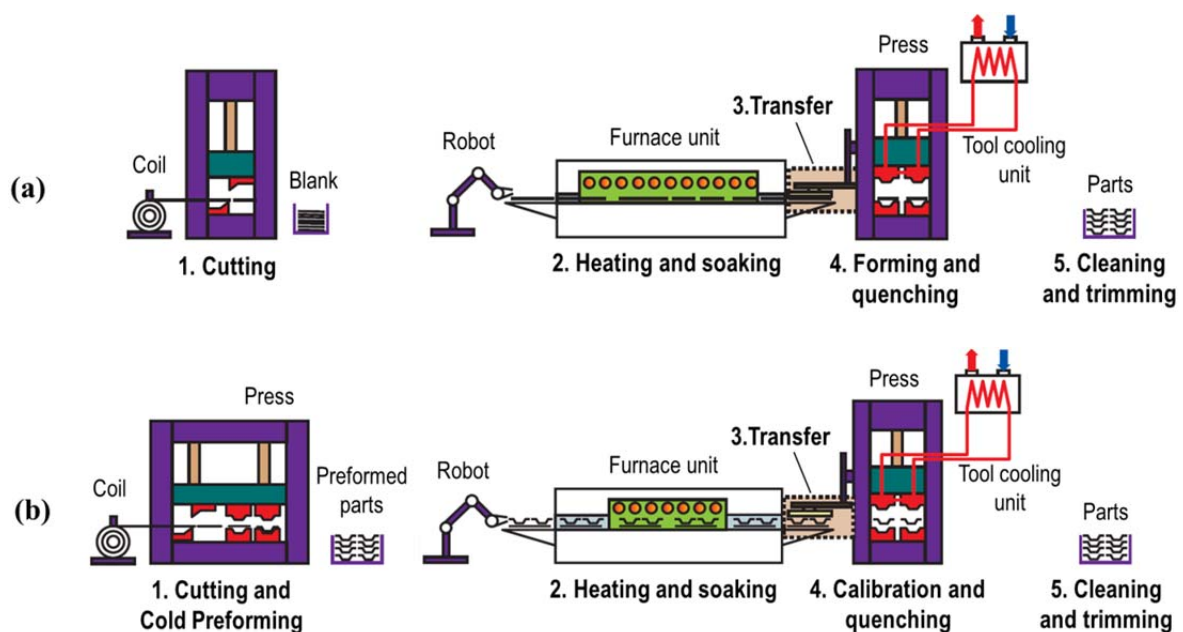


Figure 2.1 Hot stamping processes: (a) direct method (b) indirect method [53]

2.1.1 Boron steel – 22MnB5

- Material information

The most commonly used steel grade in hot stamping processes is 22MnB5 boron steel [29], which is widely produced by various steel suppliers, such as ArcelorMittal, ThyssenKrupp, SSAB, etc., under different commercial names. Although the 22MnB5 steel grade is not standardised [54], targeting the same material properties for hot stamping and applications, steel

products from different suppliers have similar chemical compositions. Representative data on the composition ranges of alloys in the boron steel, provided by SSAB for Docol 22MnB5, are given in Table 2.1.

Table 2.1 Chemical composition of a typical 22MnB5 boron steel (mass in % min-max) [55]

C	Si	Mn	P	S	Cr	B
0.20–0.25	0.20–0.35	1.00–1.30	0.030	0.010	0.14–0.26	0.0015–0.005

As delivered boron steel, with microstructure of ferrite and pearlite, has relatively low strength and high ductility; the boron steel after press hardening, with microstructure of full martensite, has ultra-high strength and reduced ductility. Data on the mechanical properties of boron steel 22MnB5 provided by different suppliers are slightly different, probably caused by the variations in chemical compositions or testing methods. A set of data on the property ranges of 22MnB5 under different conditions is summarised and listed in Table 2.2.

Table 2.2 Mechanical properties of 22MnB5 boron steels [20, 21, 54, 55]

Condition	Yield strength (MPa)	Tensile strength (MPa)	Elongation (%)
As-delivered	320-550	500-700	10-26
Annealed	310-400	480-560	20-28
Hardened in water	1000-1100	1500-1650	5-7

- Coating

Boron steel blanks are generally pre-coated with a protective layer, so as to reduce surface oxidation and decarburization. The most widespread protection on the 22MnB5 boron steel is Al-Si based coating which is transformed into a Fe-Al-Si layer during heating, preventing the formation of scales. The hot-dip aluminized blanks are not applicable for indirect hot stamping processes, which is due to the lower ductility of the Al-Si layer compared to the boron steel at room temperature [19, 29].

- Thermal-mechanical properties

Under hot stamping conditions, the influence of rolling direction and defining anisotropy, which are usually important parameters in cold forming, are diminished, while the effects of temperature and strain rate play a prominent role [16, 56]. Thus, investigation on the thermo-mechanical properties of austenitic boron steel are mainly focused on the characterisation of its viscoplastic behaviour in dependence of temperature and strain rate [23, 52, 57, 58]. Figure 2.2 and Figure 2.3 present typical stress-strain curves (symbols) of austenitic boron steel varying with test conditions. It can be clearly seen that the flow stress level increases with decreasing deformation temperature and increasing strain rate.

Extensive studies on materials modelling of the thermo-mechanical hot stamping process have been carried out [25, 59, 60]. Various semi-empirical and physically based material models have been proposed to describe the flow stress of boron steel during forming, which has been reviewed by Karbasian et al. [29]. Figure 2.2 shows that good numerical predictions have been achieved through Molinari-Ravichandran model and Voce-Kocks model adopted by Naderi et al. [22]. Voce-Kocks model has produced slightly better results in this figure, but Molinari-Ravichandran is more robust because of its capacity to reproduce history effects, through the evolution law of internal parameters [22, 29]. However, both models have described only part of the stress-strain

curves up to stress saturation. A set of viscoplastic-damage constitutive model based on Lin's modelling theories [61-63] has been adopted by Cai [16] who worked on boron steel prior to the author's work in the same research group. Figure 2.3 shows the whole stress-strain curves of boron steel USIBOR 1500P provided by ArcelorMittal, where the reduction in stress due to damage until material failure can be predicted through the material model. Thus the feature that the material exhibits different levels of ductility at different testing conditions can be well described. These achievements have shown that the modelling of deformation behaviour of austenitic boron steel under hot stamping conditions is realistic.

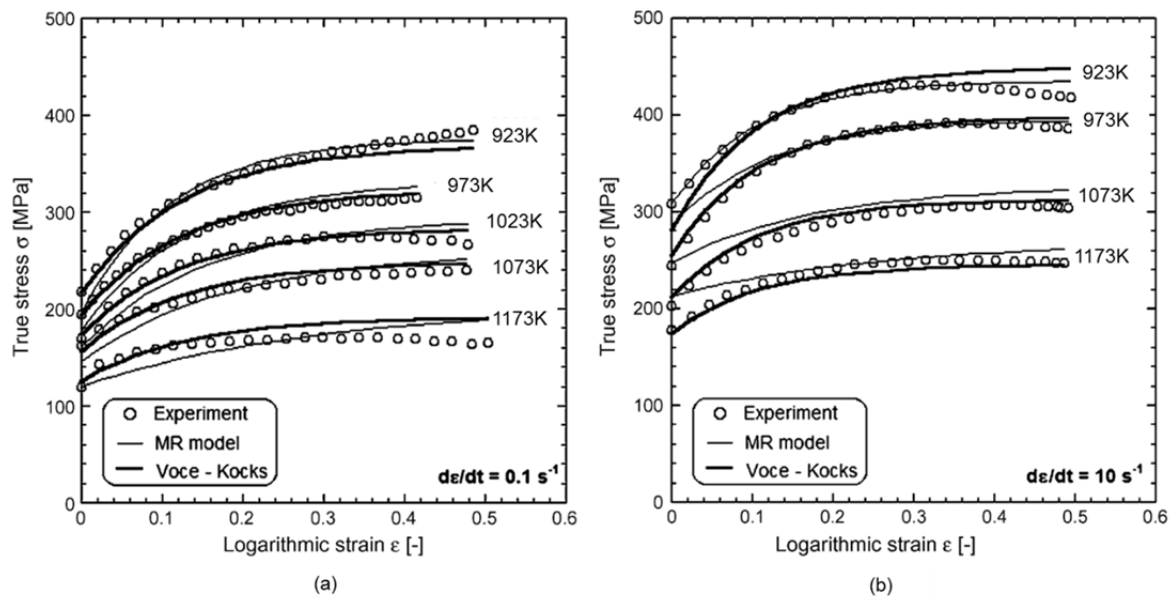


Figure 2.2 Experimental data and numerical predictions of 22MnB5 flow behaviours at different temperatures from 923K to 1173K at the strain rate of (a) 0.1/s and (b) 10/s [22]

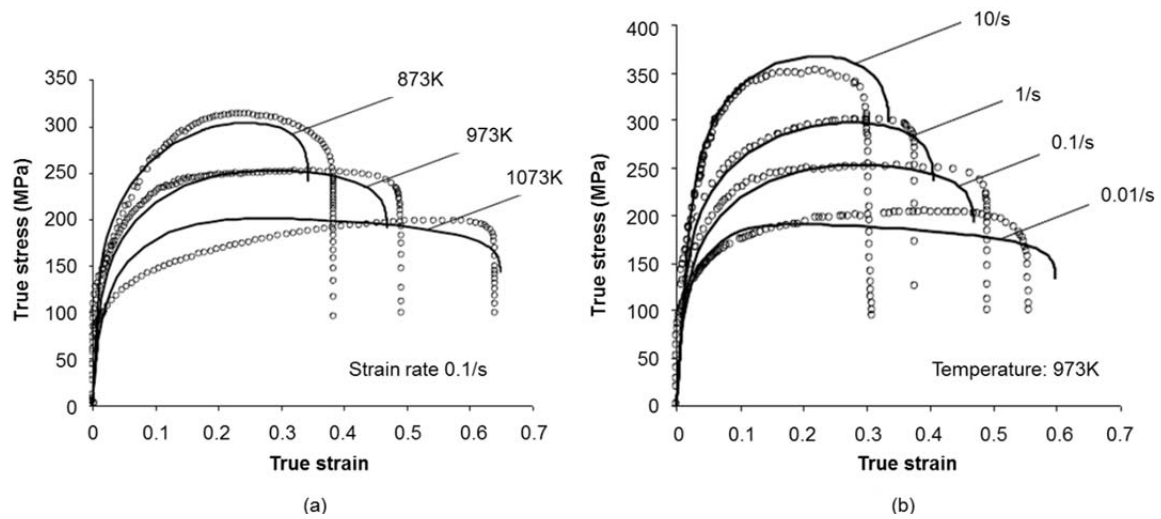


Figure 2.3 Experimental (symbols) and numerical predicted (solid curves) flow behaviours of boron steel (USIBOR 1500P, ArcelorMittal) at (a) different temperatures from 873K to 1073K (strain rate: 0.1/s) and (b) different strain rates from 0.01/s to 10/s (deformation temperature: 973K) [16]

- Phase transformation during quenching

Phase transformation from austenite to martensite during quenching is crucial in hot stamping processes. Press hardening cannot be a realistic technology without the development of metals with high quenchability. Systematic research on the phase transformation mechanisms of boron steels started from 1970's [64]. It was found that a small amount of boron (0.002%–0.004%) could have a significant effect on quenchability (i.e. the critical quenching rate for martensitic transformation) of steels; in addition, a similar level of boron can confer hardenability in low carbon steels, so as to enable high strength components to be formed [60]. Thus, realization of desired phase transformation and hardenability by technically feasible cooling rates became possible. The maximum hardenability of the materials is ensured by retaining the boron in solution within the grains, without sufficient time for diffusion [65].

Figure 2.4 shows the continuous cooling transformation (CCT) diagram (in solid lines) of USIBOR 1500P (a typical 22MnB5 boron steel with Al-Si coating produced by ArcelorMittal). The minimum cooling rate required for complete martensitic transformation is 27K/s [24].

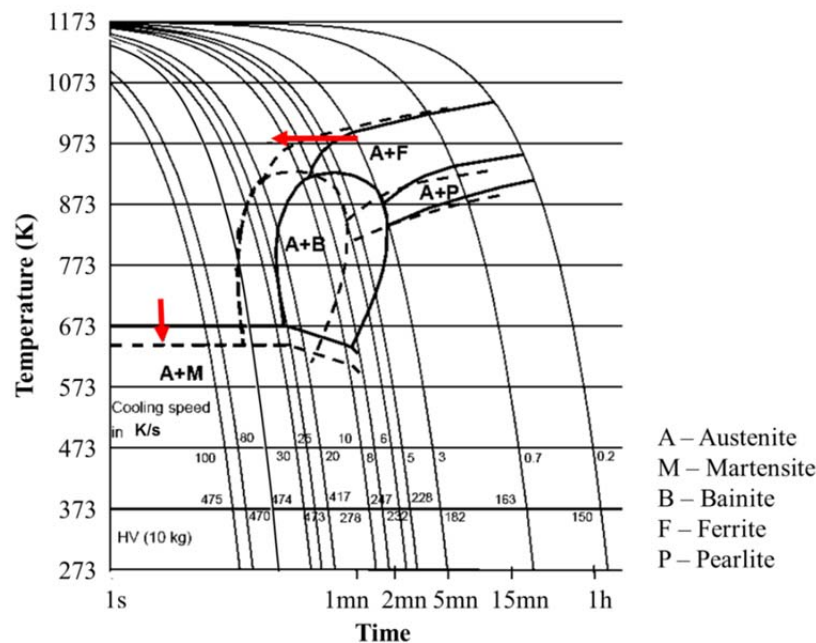


Figure 2.4 CCT diagram of a typical 22MnB5 boron steel (USIBOR 1500P, ArcelorMittal) under the undeformed (solid lines) [24] and deformed (dashed lines) states

It has been reported that the plastic deformation of austenite can influence its decomposition in steels. A high density of defects in strained austenite results in acceleration of diffusion-controlled phase transformations, such as the formation of ferrite and pearlite, and prevents martensitic transformation compared to non-deformed condition [66, 67]. This is an important problem to be addressed in press hardening processes, since the critical cooling rate for full martensite formation varies with the extent of pre-deformation and the requirement in quenching the parts becomes more severe. Great attention has been given in the last few years to the effect of plastic deformation on the phase transformations in hot stamped boron steel during cooling [34, 37, 68]. Barcellona et al. [69] and Naderi et al. [70] have drawn similar conclusions that the imposed deformation facilitates the formation of bainite and ferrite in 22MnB5 steel and the

continuous cooling transformation (CCT) diagram shifts towards left and down (the trend is illustrated in Figure 2.4). Min et al [71] have studied the mechanism of the phenomena and concluded that: the plastic deformation increases the stored energy in austenite, so as to increase the driving force and shorten the incubation time for diffusional phase transformations. At the same time, Abbasi et al. [72] have investigated the effects of deformation temperature and strain rate on austenite decomposition in boron steel and concluded that: dislocations in austenite halt the motion of glissile interfaces for the coordinated movement of atoms, which results in the impediment of martensitic transformation. To characterise the plastic strain effects, Cai [16] has modelled the bainite transformation in deformed boron steel by taking dislocation density into account, thus the influence of deformation conditions, such as temperature, strain rate and strain level, can be rationalised as one factor in the model. The bainite transformation model can also be extended to describe other diffusion-controlled phase transformations. Having the volume fractions of bainite, ferrite, and pearlite quantified, the martensite fraction in as-quenched parts is able to be predicted, for various hot stamping conditions.

2.1.2 Process parameters

Critical operations in a typical direct hot stamping process are heating blanks, and forming and quenching the parts in cold dies. The temperature profile applied to boron steel sheet, corresponding to the steps 2–4 in Figure 2.1 (a), is schematically presented in Figure 2.5. Important process parameters during the industrial processing are discussed below:

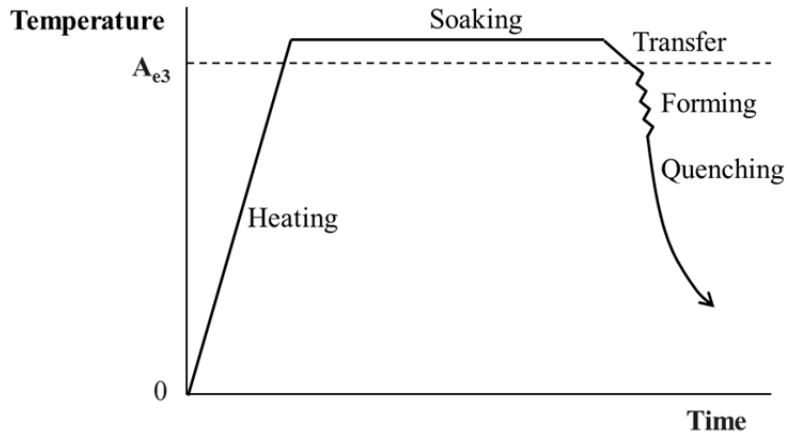


Figure 2.5 Schematic of the typical temperature profile of blanks in hot stamping processes

To achieve desired austenitic microstructure, boron steel has to be heated above full austenite formation temperature A_{e3} (about 1103K–1123K for 22MnB5 [21, 56]) and soaked for a certain time length. For the state of technology, blanks are usually heated in roller hearth furnaces to 1173K–1223K and soaked for 3–10 minutes [16, 56]. Due to the need for large volume, some furnaces of the existing hot stamping lines are 40m in length, which requires much floor space and is costly, and makes reducing heating time a most pressing demand on heating system [29]. Two main approaches to solve the problem are seeking alternative heating technologies and improving process control of thermal conditions. The former one has been under development in recent years, which is described in subsection 2.2.2.2. The latter one requires characterisation of the effects of thermal conditions on austenitization in boron steel. It has been found that both the increase in soaking temperature and the reduction in blank thickness enable a homogenous austenitization to be achieved within shorter heat treatment time [29]. The influence of blank thickness can be attributed to the effect of heating rate on the transformation, which means a higher heating rate facilitates the austenite formation. To determine the optimised thermal condition, further studies on the characterisation of austenite formation behaviour is desirable. A review on austenitization in boron steel and discussion is given in detail in section 2.3.

The forming process has to be completed before the decomposition of austenite. Thereby, short transfer time as well as a fast tool closing and forming operation, to minimise heat loss, are preconditions for successful process control. On the other hand, the heat has to be extracted from the as-formed part efficiently to ensure full martensitic transformation, which requires excellent cooling capacity of the tool. To avoid possible thermal distortions, as-formed parts are usually maintained in closed dies until the temperature down to 423K [56]. This further addresses the importance of the ability of dies in extracting heat, since cooling time is the key to drive the productivity of hot stamping in mass production. To shorten the cycle time, there are various ways that efforts can be made. The most widely used approach is to improve the water cooling efficiency through proper design of cooling duct in dies [29]. At the same time, tool steels with improved heat conductivity can be adopted to accelerate the cooling rate [19]. In addition, design of hydraulic presses with special cushions, which enables best possible contact between the part and dies, can enhance the heat transfer due to high contact pressure over the part [73].

2.1.3 Advantages and limitations of conventional hot stamping processes

The advantages and current limitations of the conventional hot stamping processes are listed below based on comprehensive literature review and understanding of the forming technology:

- Advantages

- 1) Compared with conventional multi-stage forming processes, the hot stamping process is more efficient as the forming and hardening are done in the same operation; in addition, the equipment is relatively simple in both design and technology [74].
- 2) Forming force required for hot stamping is relatively low, only approximately 20–40 % of that of cold forming of high strength steels [26].

- 3) Complex geometries can be formed due to the high formability of hot alloys, which can enable the number of components necessary to form a part to be reduced [26].
- 4) Components are formed with high dimensional accuracy and good reproducibility; no spring-back and thermal distortion, no additional modifications required [73].
- 5) Press hardened parts have ultra-high strength, which can enhance structure integrity as safety components and reduce weight and cost due to less material input [73].
- 6) As-formed material properties are not dependent on forming depth, since there is no residual strain after press hardening [27].
- 7) Since the hot stamping process involves with phase transformations during both heating and cooling operations, there is great potential in technology innovation for microstructural control.

- Limitations

- 1) The increasing demand for a higher efficiency of forming processes inevitably leads to the question of how to shorten the process cycle time [29], however, the productivity of hot stamping processes is limited by the cooling time of the parts in press [73].
- 2) The safety component with uniformly ultra-high strength does not always well meet energy absorption requirements.
- 3) Dies for cutting of the press hardened UHSS steel are expensive and have high maintenance costs; the current solution to trimming the parts with laser is slow and also very expensive [56].
- 4) Heating of blanks to high temperatures in furnaces increases the cost of hot stamping [29].

2.2 Tailored solutions in hot stamping

The previously mentioned limitations of a conventionally press hardened UHSS part, in crash performance and trimming operations, can be overcome by locally introducing regions with increased ductility and decreased strength in the part. As discussed in Chapter 1, great attention is being paid to produce parts with tailored distributions of physical characteristics through technology innovation in hot stamping. The solutions to this at the state of art are reviewed in this section.

2.2.1 Manufacturing of hot stamped parts with tailored properties

2.2.1.1 Additional operations to hot stamping

To produce a part with tailored mechanical properties, in principle, effort can be made by varying the three physical characteristics: material, thickness, and microstructure, which have all been implemented in hot stamping processes through additional operations.

- Tailored welded blanks (TWB)

Forming parts using tailored welded blanks (TWB) is widely used in cold sheet metal forming, but it is a recent technology for hot stamping [75]. Usually, heat-treatable and non-heat-treatable steel steels are trimmed and laser welded together as the blank for hot stamping. The strength of the heat-treatable steel increases due to the formation of martensite in an as-formed part, contrary to that of the non-heat-treatable one, thus tailored properties of the part are obtained. For example, ArcelorMittal has developed a hot stamping material, DUCTIBOR 500P, which is designed to maintain high ductility after forming and quenching, with a UTS of 500 MPa and elongation at fracture over 15%. Therefore, by using TWB consisting of USIBOR 1500P and DUCTIBOR 500P in hot stamping, a part with both high strength and high ductility regions can

be produced [37, 39, 76, 77]. A schematic illustration of the technology applied in producing a B-pillar is shown in Figure 2.6 (a). In addition, TWB can be a combination of sheets in different thickness, which has also been used to produce safety critical components in cars, such as rear side members [78]. Besides, another new technique related to TWB is called patchworks: patch blanks are welded on top of a mother blank as local reinforcements, so as to distribute the thickness according to the structural requirement [76]. This concept has been implemented on mass production of B-pillar by Benteler, by using USIBOR 1500P 2mm thick blank as master part and 1mm thick blank as the patch [79].

It has to be noted that the welded seam in TWB has limited formability, which decreases the complexity of shapes achievable. At the same time, since any surface coating has to be removed before welding, oxidation around welding areas during heating is another problem. In addition, for TWB with varying thickness, including patchworks, the thickness discontinuity should be allowed for in tool design.

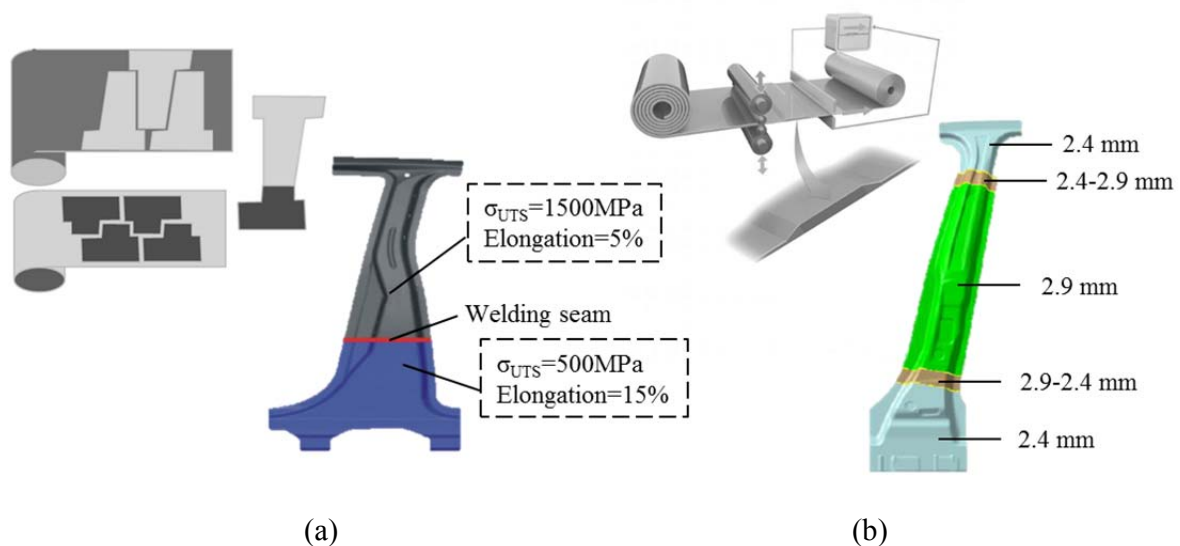


Figure 2.6 Schematics illustrating the manufacturing of hot stamped B-pillars from (a) tailored welded blanks (TWB) [29, 75], and (b) tailored rolled blanks (TRB) [80, 81]

- Tailored rolled blanks (TRB)

Tailored rolled blanks (TRB) are made of the same material with variable thickness profiles by rolling processes within the same blank [75, 79]. Due to the potential in reducing weight and locally adjusting part behaviour [79], TRB has been applied in hot stamping for automotive applications since 2006 and the TRB hot stamped parts have been used in at least 12 recent automobiles, including Ford focus, VW Golf, BMW 3/X5/X6, and Audi A3 [82]. The technology applied in producing a B-pillar is schematically shown in Figure 2.6 (b).

Compared with TWB, more precise tuning of the shape can be achieved by TRB due to the possibility to get many stepped changes in the thickness of the part, with a smooth transition at each change instead of weld seams. But, again, the variation in blank thickness is a concern in tool design, since the precision of the formed shape and good contact between the blank and dies for complete martensite transformation are required. In addition, the cost for TRB is adversely affected by a potentially lower material utilisation ratio due to nesting constraints in the strip [76].

- Post tempering

The application of this technology in hot stamping is concerned with a tempering treatment conducted on portions of a fully press hardened part, in order to locally change the martensite to ductile phases with lower strength [76]. It has also been applied in producing automotive safety critical part, such as rear side members [83]. Compared with TWB and TRB solutions, post tempering is more locally adjustable in tuning the properties, capable of taking care of small features. But it can take as long as several minutes to treat a part [37].

In addition to the shortcomings previously discussed for each solution, the common downfall for all of them is the addition of another operation (welding, rolling, and tempering) in the

production chain, which increases the cost and weakens the advantage of hot stamping for being capable of producing products within one operation.

2.2.1.2 Selective heat treatment strategies integrated in hot stamping

Due to the intrinsic advantage of hot stamping for its potential in microstructural control, new strategies, to obtain a tailored part from a single blank through tailored process control in a single hot stamping operation, are more promising solutions compared with the ones discussed in the previous subsection. Two main strategies, to control phase transformation in boron steel by selective heating or cooling, are introduced below:

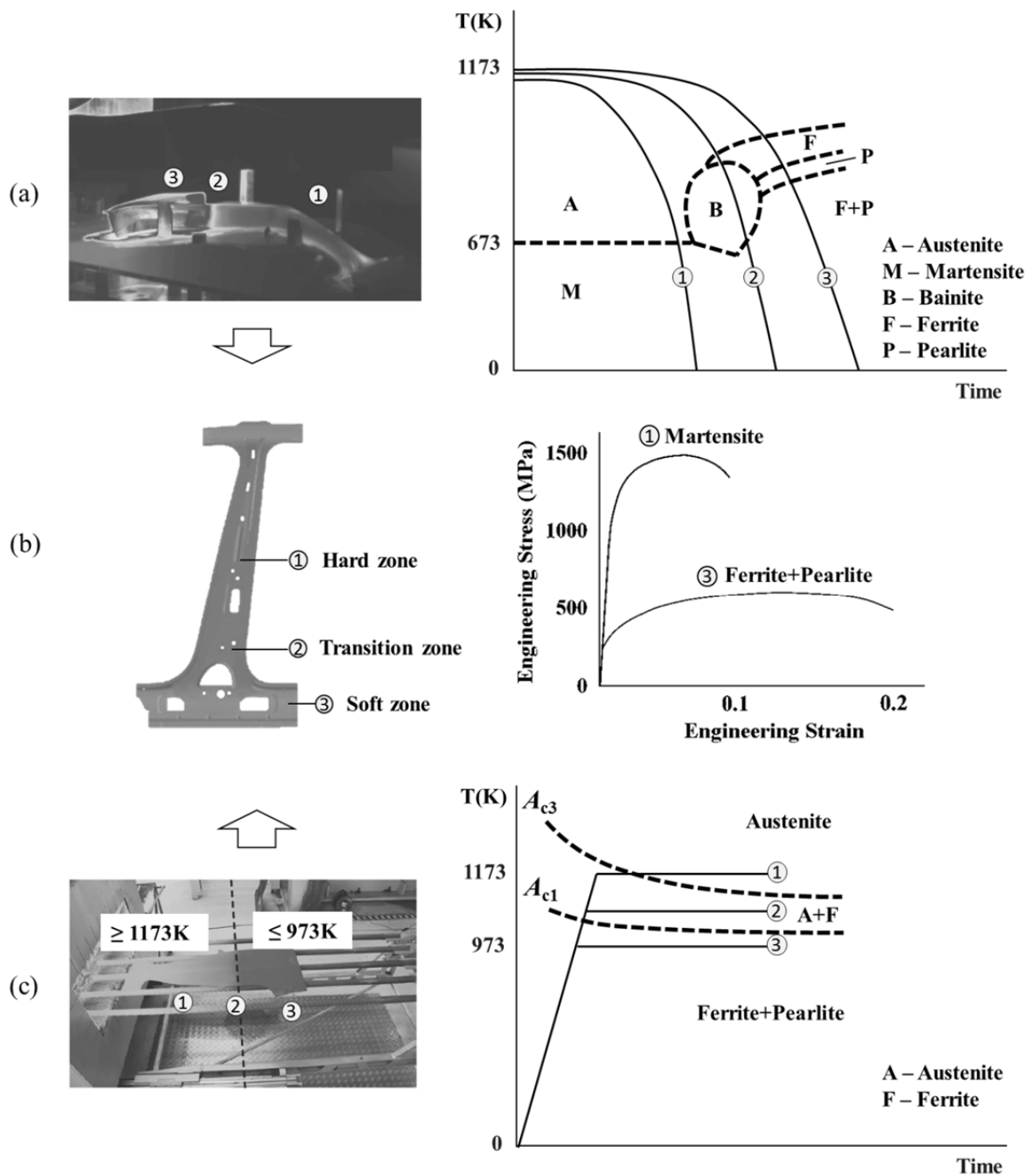


Figure 2.7 hot stamping of a B-Pillar with graded microstructures by selective heat treatment: (a) Image of a hot stamped B-pillar being partially hardened [40], with a temperature profile of a selective cooling process in a continuous cooling transformation (CCT) diagram (b) An as-formed B-pillar with graded properties, and the typical tensile properties of the martensite and initial phase of boron steel (c) Image of a blank being partially austenitized, with a temperature profile of a selective heating process in a continuous heating transformation (CHT) diagram

- Selective cooling for partial press hardening

In this concept, the whole boron steel blank is fully austenitized but only a part of it is quenched to martensite during cooling. The mechanism of the strategy is illustrated through an example of the production of a tailored B-pillar in Figures 2.7 (a) and (b). Figure 2.7 (b) shows the different regions in the B-pillar desiring different mechanical properties: ① is a hard zone with martensite to provide high intrusion resistance, ③ is a soft zone with ferrite and pearlite phases for high energy absorption, and ② is the transition zone where the mechanical properties vary with the microstructural phase compositions. To achieve this, in Figure 2.7 (a), thermal conditions for the hot stamped B-pillar in dies are controlled to enable a high cooling rate in zone ① for martensite transformation and a low cooling rate in zone ③ for ferrite and pearlite transformation. With respect to the transition zone, a representative cooling curve ② is presented in the continuous cooling transformation (CCT) diagram of boron steel in Figure 2.7 (a), where multiple phase states can be obtained. The length and microstructural distribution of the transition zone are determined by applied cooling rate gradient. The process control of cooling conditions can be realised in various ways. For example, ‘tailored tempering’ is currently a popular technology patented by ThyssenKrupp: by partially heating the stamping dies, the temperature difference between the hot blank and the stamping die in the heated zones is lower, thus the blank cools more slowly in these areas [40]. A detailed review about the implementation of the selective cooling strategy is given in subsection 2.2.2.1.

- Selective heating and press hardening

In this concept, only a part of the boron steel blank is austenitized for subsequent hardening, whereas the other part remains the initial phase state throughout the hot stamping process. To match the discussion about selective cooling, the mechanism of the selective heating strategy is also illustrated in Figure 2.7, taking the production of the same B-pillar as an example. Figure 2.7

(c) shows the selectively heated blank before forming, as well as different temperature profiles applied on the different regions of the blank. In the continuous heating transformation (CHT) diagram of boron steel, there are three regions of phase states: full austenite, partial austenite combined with partial untransformed phase, initial phase. Hard zone ① desiring full martensite is heated and soaked to the full austenite region (about 1173K) in the CHT diagram, and soft zone ③ is heated to medium temperature (about 973K) to retain the initial phase of boron steel (ferrite and pearlite). The transition zone ② soaked at the intercritical temperature region is partially austenitized. Provided the quenching is sufficient, the portion of austenite in the hot blank determines the portion of martensite in the press hardened B-pillar part. The length and microstructural distribution of the transition zone in the final part depend on the applied temperature gradient on the hot blank. It is noted that, different from the transition zone produced by selective cooling which can consist a large fraction of bainite, the transition zone produced by selective heating is mainly composed of the austenite and initial (ferrite and pearlite) phases, the mechanisms of which is illustrated by the CCT and CHT diagrams in Figure 2.7. The approaches to realise the selective heating control are discussed in subsection 2.2.2.2.

2.2.2 Technologies for process control of thermal conditions

2.2.2.1 Selective cooling solutions

The key mechanism for achieving desired cooling rates within selected regions of the dies and the part therein is heat transfer control. The concepts introduced in subsection 2.1.2 for improving the quenching efficiency can be implemented adversely to obtain a lower cooling rate. All approaches available in literature can be summarised as the control of temperature difference and heat transfer coefficient (HTC) between the blank and dies [45, 84]. Specific technologies are introduced below:

- Differential die temperatures

The cooling rate of a part can be reduced by increasing the temperature of the die. Heat transfer between the blank and dies will decrease due to a lower temperature difference. Therefore, by heating or cooling different tool zones to different temperatures, the properties of the produced part can be selectively adjusted in terms of graded microstructure. HONDA MOTOR has proposed this concept in a patent for microstructural optimisation of automotive structures [85]. The implementation of the concept by ThyssenKrupp, as introduced in subsection 2.2.1.2, is currently being tested under production conditions [40]. Extensive studies on the efficient control of this process have also been conducted [34, 38, 86].

- Differential die surfaces

The cooling rate of a part can be affected by the contact conditions with dies. Since boron steel is not hardened by air cooling, the strength distribution in the part can be controlled by limiting the contact with dies to certain portions [18]. A problem for the design of partial contact gaps is that the shape accuracy of the part corresponding to the gap areas cannot be guaranteed. A solution to the problem is to make textures on die surfaces, so that the heat transfer coefficient (HTC) is reduced due to the clearance between the blank and dies [23, 87]. Figure 2.8 schematically shows the different types of tool surface textures, which has been patented by Gestamp Hardtech [87].

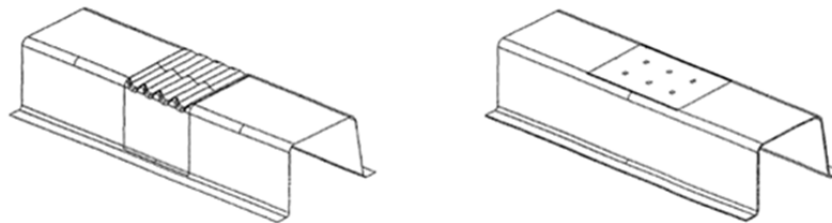


Figure 2.8 Textures on die surfaces [87]

- Differential thermal conductivities

Selective cooling of a part can be achieved by having tools with varying thermal conductivities. For example, Steatite plates, with very low thermal conductivity, were embedded in the blank holder and die by Mori et al. [18] to prevent hardening of the flanges of a part. The recently developed nanocasting technology enables tools with complex cooling strategies to be realised at a reasonable cost and any desired conductivity variations ranging from 7 to 66 W/m·K [19].

- Differential applied pressures [34]

Since HTC is a function of pressure between the contacted surfaces, heat transfer between the blank and dies can be controlled by applied contact pressure. Selective cooling of a part can thus be realised by applying differential pressures through special tool design and process control. This concept has been studied by Merklein et al. under laboratory conditions [34].

2.2.2.2 Advanced techniques for selective heating

Different from the selective cooling solutions which have been well developed, the development of technologies in heating for tailored solutions are still at the preliminary stage. Novel attempts and potentials in implementing the selective heating concept into different types of heating systems are reviewed and discussed below:

- Furnace - radiation and convection heating

On conventional hot stamping production lines, blanks are heated by radiation and convective flow of heat in continuous furnaces [29, 88]. For blanks with certain properties and thickness, the heating rate is determined by the speed of transport (by rollers or walking beams) and the temperatures in different consecutive chambers [88]. Tailored solutions can be realised in

furnaces, for example, by partially shielding the blank from thermal radiation, or setting selective heating zones which are isolated from each other by a wall [76].

- Resistance heating

In resistance heating, the heated part is connected in series with a power source. The electric resistance of metal part causes the heating of itself. The heat generated is proportional to the loss of power. For a higher efficiency factor, the resistance heating is mainly used for long components, such as pipes, rods, wire and bands. The problem limiting its industrial application is the difficulty in getting homogeneous heating temperature fields over the components [29]. Nevertheless, this technology has its potential in sheet metal forming for specific selective heating. Mori has conducted extensive studies on the resistance heating for a few years [18, 35, 89, 90], and developed a selective heating technique called ‘bypass resistance heating’. Figure 2.9 shows the principle of the heating technique. In the heating system, the zone in contact with the copper bypasses has a large cross-sectional area and low resistance. Due to the passage of the current through the copper bypasses, the zone is not heated. Thus, specific portions desiring low strength can be targeted through the bypass resistance heating. In addition, the power loss by adopting bypasses is minor because the copper bypasses are thick and short [35]. This technique is currently at a laboratory level.

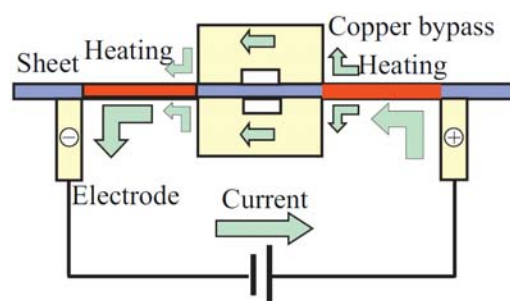


Figure 2.9 Principle of selective heating of a steel sheet using bypass resistance heating [35]

- Induction heating

When an electrical-conducting metal component enters the inductor of induction heating system, the electric current is induced in the component and consequently heat is generated [19]. Induction heating can provide very high energy supply rates and thus meets industrial requirements for mass production [91]. It is currently at the stage from laboratory investigation to industrial applications in hot stamping, which would be a promising alternative heating technology due to its ability to significantly reduce the heating time, resulting in lower investment costs and reduced floor space for the heating device [88, 92]. The combination of induction heating with other heating techniques can be used to realise selective heating of boron steel blanks. Maikranz-Valentin et al. [5] have produced tailored components by uniformly heating 22MnB5 boron steel blanks to medium temperatures without phase transformation in a furnace, and partially re-heating above A_{c3} in intended high strength areas by using induction heating. Ploshikhin et al. [91] has proposed a contact heating technique called ‘contact heat treatment’, for the application in preconditioning of boron steel blanks for press hardening. In this technique, the induction heating is employed to supply energy to two contact plates, and the contact plates are used to heat the boron steel blank through conductive heat transfer, as shown in Figure 2.10. By making blanks partially contact the hot heating plates, or changing the contact conditions for varying heat transfer coefficient between blanks and heating plates, differential temperature regions can be obtained, so as to create parts with desired tailored properties.

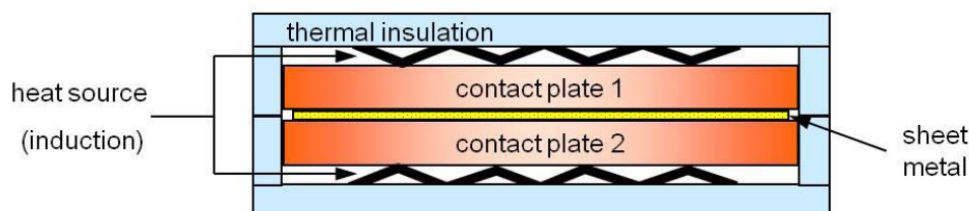


Figure 2.10 Principle of contact heating [91]

2.2.3 Analysis of the selective heating and press hardening strategy

Based on the above review and discussion, it can be appreciated that the tailored solutions for structural optimisation through selective heat treatment are advantageous and achievable for industrial applications. Compared with selective cooling, the selective heating and press hardening strategy lacks development. The possible reasons might be: the fundamental understanding of boron steel decomposition (subsection 2.1.1) and practical implementations for cooling process control have drawn great attention since the development of conventional hot stamping processes, for the purpose of efficient martensite transformation. The knowledge and techniques can be directly used or adapted to selective cooling solutions. By contrast, the selective heating and press hardening process involves intercritical annealing of boron steel and deformation of boron steel in multiple phase states, with which the conventional hot stamping process is not concerned. As a result, there are gaps existing in the relevant knowledge base.

However, attention to the selective heating and press hardening strategy is encouraged. The significant and unique advantages of the new strategy are discussed below:

1) Compared with selective cooling, the most critical advantage of selective heating is the ability to shorten process cycle time. The demand for short cooling time to improve manufacturing efficiency and the requirement for slow cooling rate to ensure ductile phase transformation is the intrinsic contradiction and vital drawback of selective cooling solutions. The proposed process, during which the blank is fully quenched, can avoid that problem; at the same time, lower heat (due to lower temperatures in partial regions) in the blank to extract can facilitate the cooling efficiency further.

2) Compared with selective cooling solutions which are all associated with design of tool features (e.g. tool cooling and heating tunnels, tool surfaces and materials, etc.), the selective heating strategy can directly be applied using the conventional hot stamping tool, and it has the flexibility

in tuning microstructural distributions in a part for optimised structural properties without remaking or modifying the tool.

3) By applying selective heating and press hardening strategy, development of advanced heating technologies will be stimulated; at the same time, lower heat is required by the partial heated blank. Thus improvement in energy efficiency is possible.

Thereby, it can be concluded that the selective heating and press hardening strategy is a promising forming technology, which has the potential in substituting selective cooling solutions, or as least expand the applicable range of hot stamping, for tailored components. Whereas, for the new forming process, concerns exist about formability and possible spring-back of the partially austenitized boron steel blank [29]. Nevertheless, no proof for the problems or assessment of the strategy was found in current literature. Therefore, a feasibility study on this strategy is necessary. At the same, fundamental studies of the thermo-mechanical behaviour of boron steel in the initial phase state under hot forming conditions are also needed.

Provided the feasibility of the selective heating and press hardening strategy is validated, its potential can only be maximised by optimising the structural performance of a part through effective process control. This is concerned with grading the microstructural distribution (including martensite zone, multiphase zone, and ferrite and pearlite zone) in a part by controlling the austenitization process during selective heating, which can only be realised when the relationship between mechanical properties of as-formed boron steels and the corresponding microstructures achieved by certain thermal conditions is quantitatively determined. Therefore, understanding and modelling the formation of austenite in boron steel under selective heating conditions, as well as the mechanical response of boron steel with various microstructures in a collision situation are critical. The studies on the two aspects in current literature are reviewed in the next two sections.

2.3 Microstructural control during heating

In the selective heating and press hardening process, the transformation of austenite during heating is of primary importance in deciding the final properties for a given part. Therefore, understanding and modelling the kinetics of austenite formation have great significance in optimising the design of heat treatment conditions.

2.3.1 Studies on austenite formation

Studies on austenite formation in steels have been carried out by many researchers [43]. Robert and Mehl established the nucleation and growth character of the transformation in steels with different starting microstructures [43, 93, 94]. However, compared with the number of investigations into decomposition of austenite during cooling, studies on austenite formation have been few [43, 44, 93, 95-97]. This is primarily because it is difficult to retain austenite at room temperature for inspection and characterisation, which makes observation of the progress of austenite formation difficult [43, 95, 97].

Stimulated by automotive applications, the development of advanced high strength steels has recently revived interest in the heating stage of the heat treatment cycle [93, 98-101]. Initially, attention was focused on partial austenite formation in intercritical annealing practices, since this offers a means of optimising the mechanical properties of dual-phase steels [42, 97, 99, 102-104]. More extensive and systematic research on the formation of austenite has been conducted during the last decade, in order to achieve quantitative understanding of microstructural evolution during transformation and the mechanisms that control it under different conditions [41-43, 95, 103-111].

However, the influence of temperature and heating rate on the progress of the transformation to austenite has always been studied separately under isothermal conditions [42, 103-105, 112] and non-isothermal conditions [16, 101, 106, 107, 113], respectively. In a real situation, the

conditions for work-piece preheating for hot pressing are first increasing temperature followed by steady-state temperature. This should be recognised if an accurate evaluation of austenite evolution is to be obtained.

Information on austenite formation in boron steels for hot stamping applications is sparse. Cai et al. [16, 114] have carried out some relevant research but it focused on only full austenite formation required by conventional hot stamping processes. Little research has been carried out on the intercritical soaking of boron steels.

2.3.2 Modelling of austenite formation

Based on the efforts in the last decades, there are various types of austenitization models having been developed. According to calculation methods, they can be generally classified as probabilistic models and deterministic models [109]. The former type introduces stochastic variables into calculation process, which can account for the stochastic character of the phase transformation and give qualitative representation of the microstructure [42, 109, 113]; the latter type is based on the time-integration of equations consisting of certain state variables, so as to characterise the microstructural evolution, in various length scales depending on the features of interest, throughout the phase transformation. The deterministic models have been predominant for describing the austenite formation in literatures. The main development methods are analytical approaches and phenomenological approaches [43].

Analytical approaches are mainly based on the analysis of mechanisms which control the austenite front migration, which requires assumptions (e.g. on growth modes) being strictly defined in advance. However, it may not be easy when the phase transformation mode is of a complex character [43, 94, 95, 101, 103, 109, 115, 116]. For austenitization in a manganese-boron steel with the ferritic-pearlitic starting microstructure, depending on heating conditions, the

growth of austenite phase can be controlled by interface reaction or volume diffusion[95], and the latter one could be carbon diffusion in austenite or manganese diffusion in ferrite [43, 117]. In this case, the analytical approach may not be an efficient way to adopt in this study.

Phenomenological approaches are mainly conducted by relating the transformation progress to the change of austenite volume fraction with time. The Avrami's equation plays an critical role in the fundamental understanding of the transformation [118]. But it is too simple to adapt to any specific case, e.g. a transformation has mixed nucleation or alternate growth mode. Thereby extensive studies have been conducted to further develop of the equation, so as to fit it to different transformation conditions [42, 96, 101, 106, 113, 119]. However, same as the problem pointed out in the previous subsection, it is found that the transformations of austenite under isothermal and non-isothermal conditions have been always modelled separately. Thus possible influence of heating rate on the subsequent isothermal transformation cannot be accounted for.

Efforts for adapting the modelling knowledge to the austenite formation in boron steel have been few. An attempt has been conducted by Cai [16] by developing a set of unified equations with an incubation factor and austenite volume fraction as state variables, taking the heating rate into account. However, this model is applicable to only continuous heating conditions. For the hot stamping practice, the boron steel is treated with continuous heating followed by steady soaking; in addition, intercritical annealing for partial austenitization is involved under selective heating conditions. Therefore, an austenite formation model which can be applied to the complex heating conditions is highly demanded.

2.4 Final properties of hot stamped panels

One precondition to introduce tailored parts in automobiles is the development of predictive models for crashworthiness analysis, which requires the identification of the mechanical

characteristics of as-formed boron steels with various microstructures, under a wide range of strain rates. Therefore, a study on the final properties of hot stamped boron steels is critical to the implementation of the selective heating and press hardening strategy.

The mechanical properties of martensitic boron steel, achieved through conventional press hardening processes, are well known and usually provided as product information by steel suppliers (given in Table 2.2 in subsection 2.1.1). Relevant studies are not many, mainly about fracture analysis [120], cooling rate effects [45], and strain rate effects [121] on the mechanical response of boron steel with full martensite.

Only due to the popularity of tailored concept, interests in hot stamped boron steels have been stimulated in the very recent years. But the information is still scattered in current literature. The most intensive research has been conducted by Bardelcik et al. [36, 37, 45, 122, 123] in the University of Waterloo. In their work, the approach to achieve tailored parts was based on the selective cooling concept. A variety of as-quenched material conditions were produced for tensile testing with various strain rates, hardness testing, and microstructural analysis. A set of representative test results are given in Figure 2.11 [37]. ‘FAQA’ and ‘Quench/Def.’ were two types of as-quenched boron steel samples obtained through different process control. ‘FAQA’ was composed of only martensite and bainite; ‘Quench/Def.’ was composed of martensite, bainite, and ferrite, with the ferrite fraction in each sample measured and shown in the figures. It was found that, due to the presence of ferrite, there was little change in material strength, but a dramatic increase in the uniform elongation for a given hardness level less than about 350 HV. It indicates that more fractions of ferrite would benefit the energy absorption of a hot stamped part with graded microstructures. In addition, as can be seen in Figure 2.11 (b), the lowest value of uniform elongation didn’t correspond to the highest hardness value, but some point between

350HV and 450 HV, which suggests the multiphase boron steel with a certain phase composition may have the worst ductility.

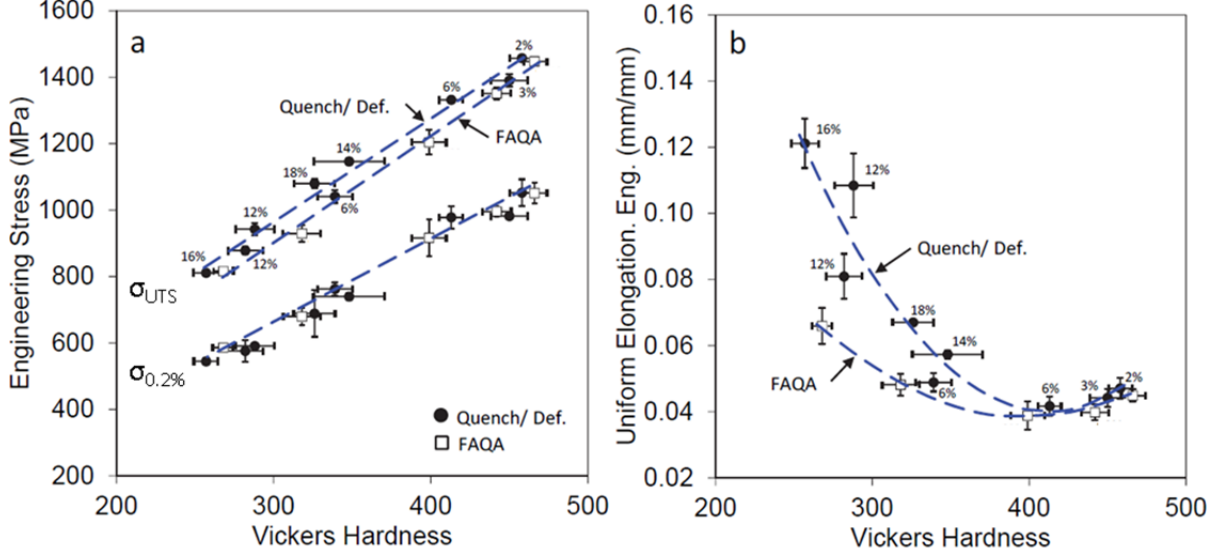


Figure 2.11 (a) Ultimate tensile strength (σ_{UTS}) and 0.2% yield stress ($\sigma_{0.2\%}$) and (b) Uniform elongation versus Vickers hardness from the quasi-static tension tests conducted at a strain rate of 0.003 /s (The error bars represent +/- the standard deviation of repeated test results) [37]

Bardelcik et al. have also developed several constitutive models to enable a part with graded microstructures, produced by selective cooling, to be simulated in a crash situation [36, 37, 122]. The most advanced one, termed ‘Tailored Crash Model II’, is given below:

$$\sigma = f(\varepsilon, \dot{\varepsilon}, [\frac{M}{M+B}], F) = \left[A([\frac{M}{M+B}], F) + \left[B([\frac{M}{M+B}], F) - A([\frac{M}{M+B}], F) \right] e^{(-\varepsilon/C([\frac{M}{M+B}], F))} \right] \cdot [1 + \dot{\varepsilon}]^D \quad (2.1)$$

where D is a constant, parameters A , B , and C are functions of martensite-bainite fraction relationship $[M/(M+B)]$ and ferrite fraction F . The model is based on the Voce hardening law with exponential-type strain rate sensitivity, capable of describing the strain rate effects, strain hardening response and overall energy absorption behaviour of a part with varying volume fractions of martensite, bainite and ferrite.

The above mentioned work is an appreciable research effort. However, the investigation was conducted on boron steel obtained from selective cooling processes, with bainite, instead of ferrite, as the dominant soft phase. For multiphase boron steel achieved from selective heating processes, with ferrite as the dominant soft phase, the previous results and deformation mechanisms may not be applicable. In addition, an accurate prediction of material failure is critical for crashworthiness simulation. But the ‘Tailored Crash Model II’ is not capable of capturing the damage characteristic of material. Consequently, the important feature of reduced ductility for multiphase boron steel with certain phase compositions, shown in Figure 2.11 (b), cannot be described. It is critical to characterise the ductility of boron steel in various phase compositions, so as to avoid unexpected failure at transition zones. Therefore, the development of a more functional constitutive model is demanded.

Studies on the final properties of boron steels produced from selective heating and press hardening processes are much fewer and preliminary. Li et al. [124] and He et al. [46] both tested the hardness and quasi-static tensile properties of boron steel samples, which were heated to different soaking temperatures and fully quenched. However, in their studies, the mechanical properties were related to only soaking temperatures and no microstructural analysis was conducted. Thus, a further study to quantitatively determine the relationship between the microstructural and mechanical characteristics of boron steel is desired. In addition, the characterisation of the strain rate sensitivity of boron steel with ferrite and pearlite phases has never been done in literature, but it is necessary for the calibration of appropriate constitutive models.

2.5 Summary

Conventional hot stamping processes, advanced technologies in hot stamping of tailored parts, as well as the associated studies on boron steel properties have been comprehensively reviewed. It

is found that the selective heating and press hardening strategy can well extend the limitations of the conventional hot stamping technology and selective cooling solutions, but there are large gaps in the relevant knowledge basis for the development of this technology. By identifying the research deficit in literature, the necessity of the fundamental studies, on the austenite transformation and deformation behaviour of boron steel under selective heating and press hardening conditions, as well as on the mechanical properties of press hardened boron steel with various microstructures, has been addressed.

CHAPTER 3 FEASIBILITY STUDIES FOR THE SELECTIVE HEATING AND PRESS HARDENING STRATEGY

3.1 Introduction

In this chapter, feasibility studies for the proposed strategy, termed as selective heating and press hardening, carried out through a set of specially designed experimental programme are described. The objectives were validation of the strategy and demonstration of its potential for structural optimisation. In the work, a lab-scale demonstrator part was designed and relevant manufacturing and property-assessment processes were defined. A heating technique and selective-heating rigs were designed to enable certain microstructural distributions in blanks to be obtained. A hot stamping tool set was designed for forming and quenching the parts. Test pieces were formed under various heating conditions to obtain demonstrator parts having variously graded microstructures. Microstructural distributions in the as-formed parts were determined through hardness testing and microstructural observation. Ultimately, structural performance of the parts was evaluated through bending tests.

3.2 Experimental design

3.2.1 Concept illustration

The concept in the study is the optimisation of structural performance of press-hardened parts by means of microstructural design, realised by controlling thermal conditions during preheating in hot stamping processes. Figure 3.1 schematically shows in simplified form, the disposition of

microstructure in work-piece and formed part and the method of assessing mechanical properties. Figure 3 (a) illustrates a portion S/L of a work-piece, the hot zone, fully austenitized by heating to and soaking at a temperature of 1173K. The two ends, the warm zones, are heated to a temperature below austenitization start temperature, 993K [21]. Thereby a warm zone is composed of the initial phase, and multiphase in the transition regions adjacent to the hot zone. Figure 3 (b) shows the pressed shape, representing an impact beam, which has been die quenched and is fully martensitic in the prior hot zone. Figure 3 (c) shows load bearing assessment of the as-formed part through three point bending test. The performance of the part would vary with the length of full martensite zone (hard zone) and this can be optimised in the selective heating operation to comply with a particular design specification.

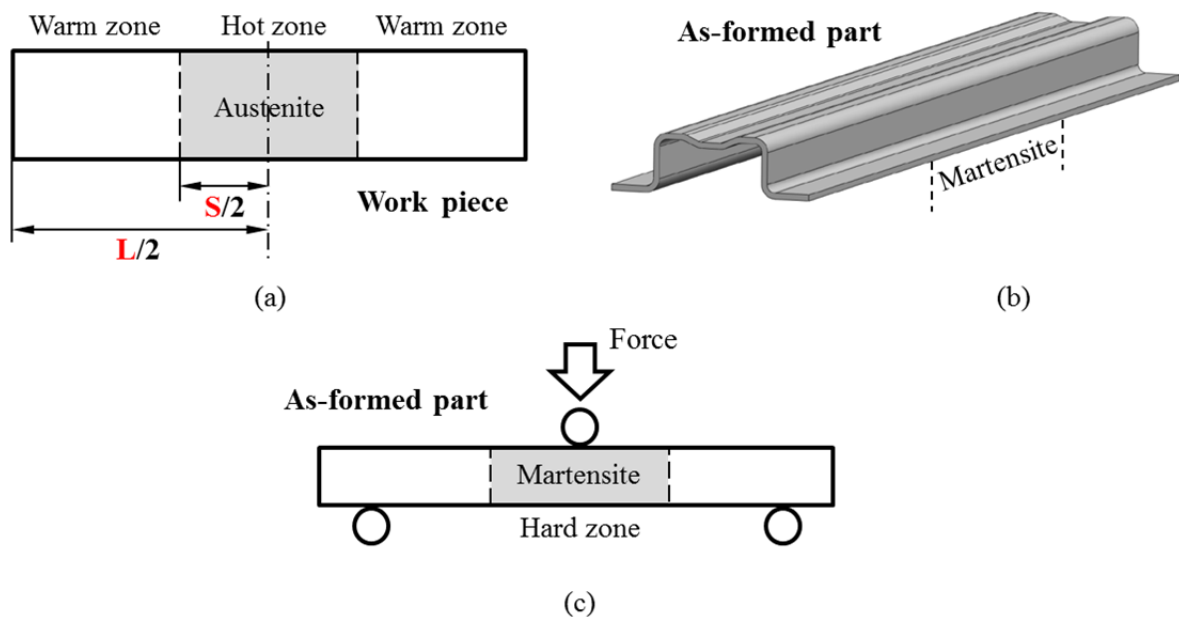


Figure 3.1 Schematics illustrating the manufacturing process and experimentation for function assessment (a) Selective heating of the work-piece (b) An as-formed part after hot stamping and cold die quenching (c) Three point bending of the as-formed part

3.2.2 Material and demonstrator part

The material used in this study was a 22MnB5 manganese-boron steel provided by the project sponsor SAIC MOTOR. It was cold rolled and hot-dip aluminized. Product information provided by steel supplier: the initial microstructure contained about 78/22 mixture of proeutectoid ferrite and pearlite; the chemical composition of the investigated steel is listed in Table 3.1. All work-pieces used for the experiment were machined from the same batch of as-delivered, 1.6mm thick, boron steel sheet.

Table 3.1 Chemical composition (Max value - ladle analysis in %) [21]

C	Si	Mn	P	S	Cr + Mo	Ti	B
0.25	0.40	1.40	0.025	0.010	0.50	0.05	0.005

Figure 3.2 shows the cross-section of a lab-scale demonstrator part, the length (L) of which was 320 mm. The dimensions of the initial blank were 80mm \times 320mm.

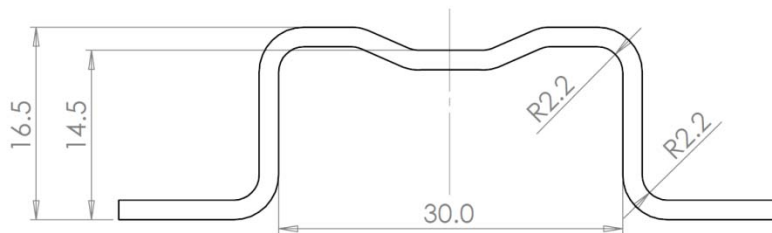


Figure 3.2 Cross-section of a demonstrator beam (dimensions are in mm)

3.2.3 Test programme

By taking the length of hot zone, S , as a variable, four test conditions were defined and they are listed in Table 3.1, where S-60mm and S-100mm are two conditions designed for selective heating with 60mm and 100mm hot zones respectively, and S-0mm and S-320mm represent

uniform heating without a hot zone and with full hot zone respectively. In addition, assessment of both microstructural and structural properties of as-formed parts was conducted for conditions presented in Table 3.2.

Table 3.2 Test programme ('√' represents the selected test conditions)

Test condition	Hot forming	Hardness distribution		Microstructure observation	Bending tests
		Sectional	Longitudinal		
S-0mm	√				√
S-60mm	√		√		√
S-100mm	√		√	√	√
S-320mm	√	√			√

3.3 Heating technique

Selective heating is an essential part of the strategy. In this work, it was realised by local contact heat treatment in a furnace under laboratory conditions. The implementation is shown in Figures 3.3 (a) and (b). A selective heating rig, consisting of two heating blocks made of stainless steel, served as an energy reservoir for locally heating a blank in a hot zone. It was prepositioned in a furnace and preheated to a temperature above 1173K. Heat transfer in the hot zone took place when a cold work-piece was positioned between two hot blocks. At the same time, the two ends of the work-piece, the warm zones, mainly heated by radiation and convection within the furnace were thus heated at a lower rate and their maximum temperature was controlled to just below 993K.

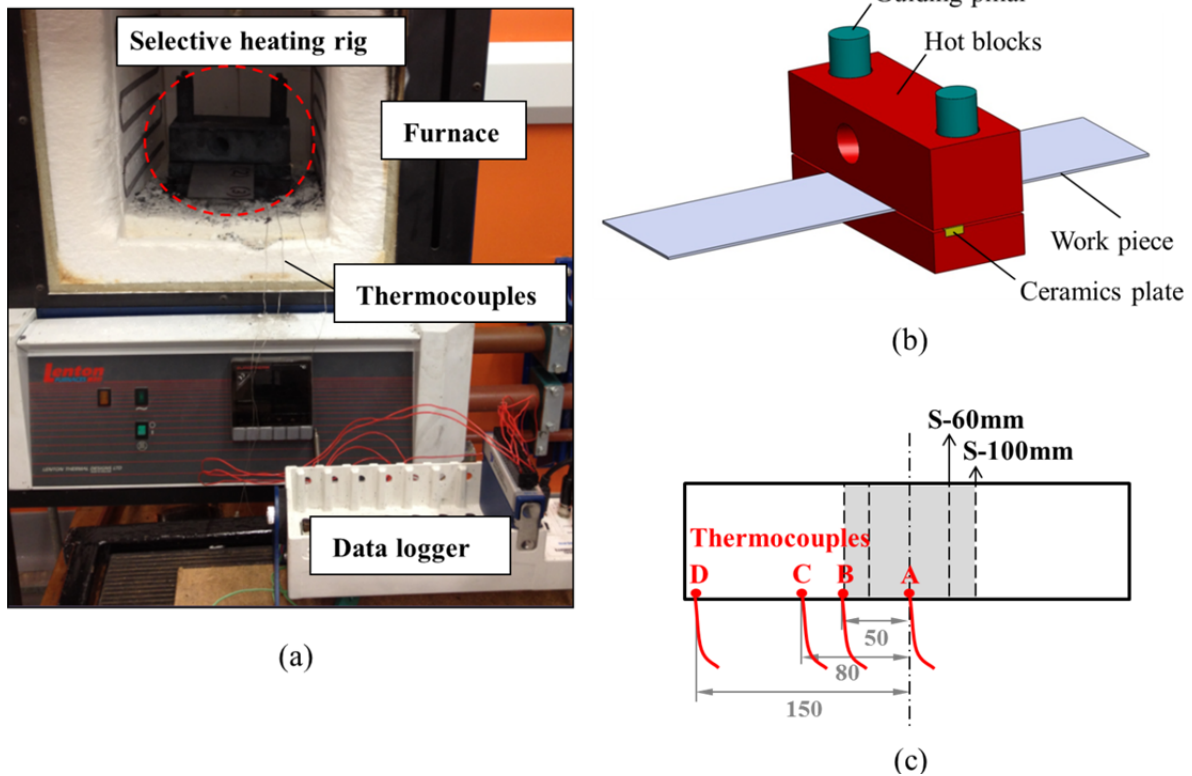


Figure 3.3 Selective heating technique (a) Set-up of facilities for selective heating and temperature measurement (b) 3-D diagram of the selective heating rig (c) Location of thermocouples attached to a work-piece (dimensions in the figure are in mm)

With respect to the selective heating rig, in Figures 3.3 (b), the blocks were massive to ensure sufficient heat capacity. In addition, the top block was designed to be larger to provide higher pressure between work-piece and blocks and enhance heat transfer. Ceramic plates were inserted between the blocks to give them 1mm gap during preheating, in order to enable easy separation before positioning the work-piece. Two pairs of hot blocks were made for 60mm and 100mm of hot zones. To enable the two selective heating conditions, S-60mm and S-100mm, to share a unified process control, the heating rig should be of the same heat capacity for both conditions. Since hot blocks for S-100s were wider, an additional block was placed beneath the selective heating rig for the S-60mm condition, so that the total volume of the heating blocks was the same as that for the S-100mm heating blocks.

The effective control of thermal conditions to ensure a desired temperature distribution in a work-piece was required. Therefore, thermocouples were attached to a work-piece to monitor temperature profiles and enabled a suitable heating procedure to be determined. Figure 3.3 (c) shows the location of thermocouples on the work-piece. In order to avoid possible influence on the contact between the work-piece and blocks, small holes were drilled perpendicular to through-thickness section to fix K-type thermocouples of 0.5mm in diameter. The output ends of the thermocouples were connected to a National Instruments data logger for data acquisition, as shown in Figure 3.3 (c).

For selective heating conditions, since the preheated rig was a massive heat resource in the small chamber, the reduction of environmental temperatures had to be realised by opening the chamber at intervals, to enhance air convection. The temperature profiles were decided by preheating temperature of the hot blocks and the time to increase and reduce air convection. Trial and error was adopted, aiming to get full austenitization in the hot zone with no phase transformation in the warm zones. The determined thermal parameters and operation procedure for the selective heating, which were used as standards for all following hot stamping tests, were given as follows:

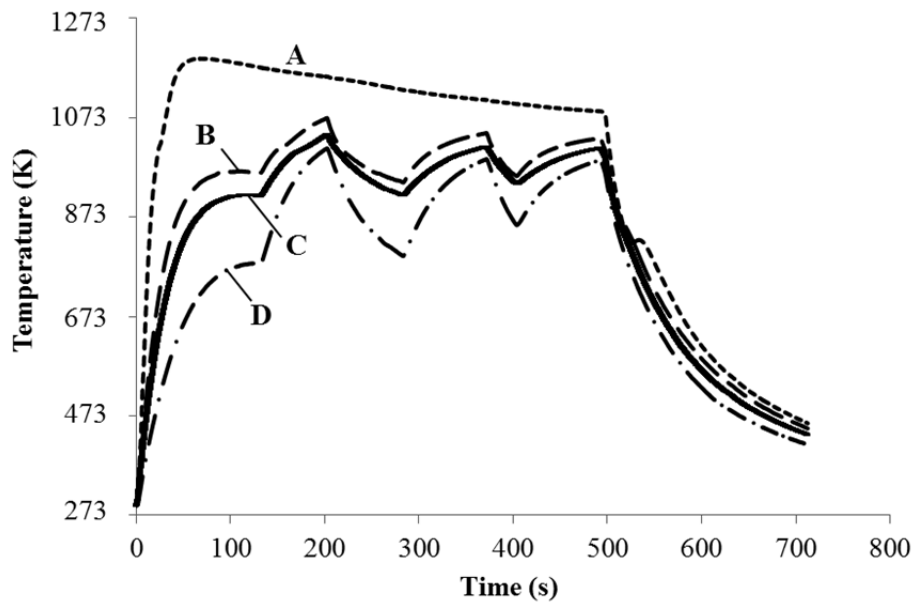
- 1) The selective heating rig was preheated to 1253K in the furnace;
- 2) The furnace control temperature was set to 943K right before positioning the work-piece;
- 3) The work-piece was positioned between hot blocks, and the furnace door was kept open for air convection for 140 seconds;
- 4) The furnace door was closed for no external air convection for 80 seconds;
- 5) External air convection was initiated for 60 seconds;
- 6) External air convention was prevented for 90 seconds;
- 7) External air convection was initiated for 30 seconds;
- 8) External air convection was prevented for 100 seconds.

9) The work-piece was removed from the furnace.

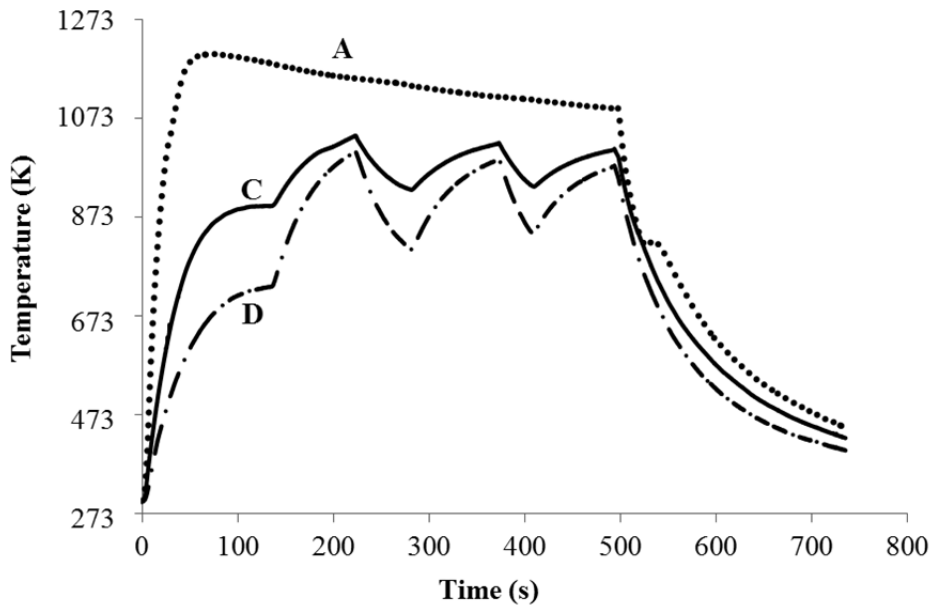
Figures 3.4 (a) and (b) respectively show the obtained temperature profiles of different positions of the work-piece under S-60mm and S-100mm conditions. For each condition, temperature gradients along the work-piece can be seen. The adjustment of air convection is revealed by the sawtooth-shape of temperature profiles for warm zones (i.e. thermocouples B, C, and D) in both figures. The amplitude of these temperature vibrations can be reduced by increasing the frequency and decreasing the time intervals of air convection. However, the feasibility of manual controlling the procedure limited the rate at which the operations could be undertaken.

For uniform heating, S-0mm and S-320mm, no hot blocks were used and the work-piece was put into the furnace with environmental temperatures of 973K and 1173K respectively for 500 seconds.

Figure 3.5 shows the summary of final temperature profiles obtained for the four test conditions. Representative positions are chosen, for example, 'S-100mm-A' represents the hot zone temperature measured by thermocouple A for S-100mm test condition. Good consistency for S-60mm and S-100mm was achieved. As seen in the figure, full austenitization was expected at the hot zone for selective heating conditions, as that for the uniform heating condition S-320mm; no phase transformation was expected at the portion D of warm zones, as that for S-0mm. In addition, if the time of transform of work-piece from furnace to tools after soaking is known, the natural cooling curves can be used to estimate the starting forming temperature for various conditions.



(a) S-60mm



(b) S-100mm

Figure 3.4 Temperature profiles of different positions of a work-piece under selective heating conditions: (a) S-60mm, (b) S-100mm

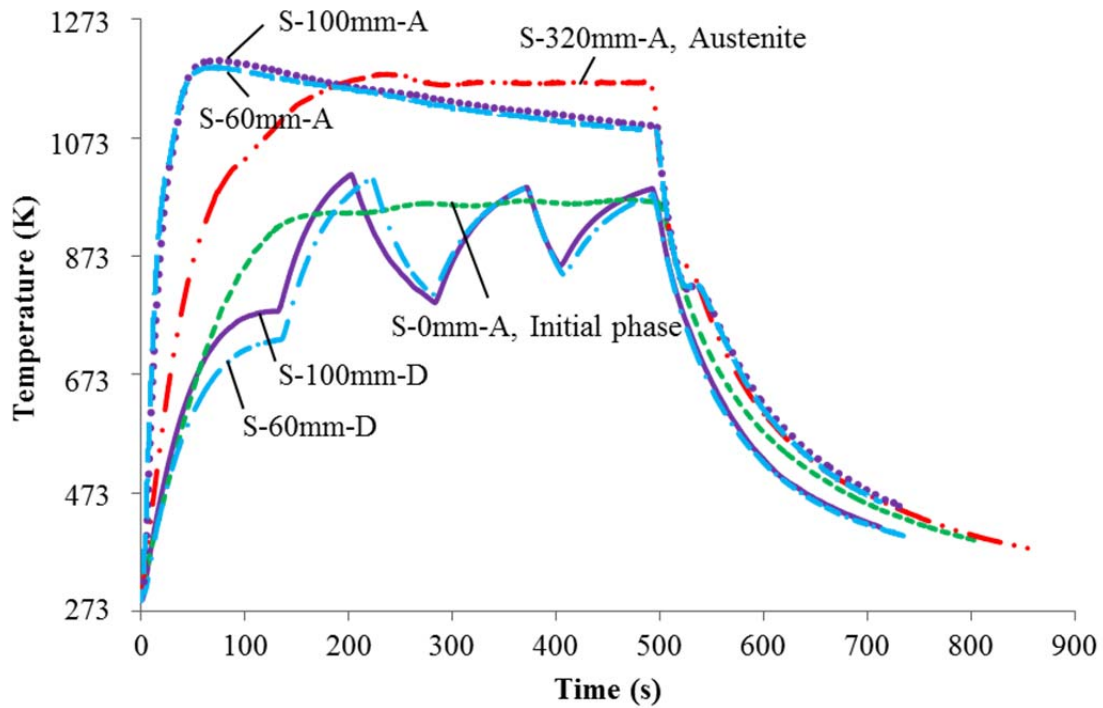


Figure 3.5 Temperature profiles for 4 different test conditions

3.4 Hot stamping

3.4.1 Design of hot stamping tool set

A hot stamping tool set was designed to be set on a hydraulic press for forming the demonstrator part. The two main functions of the tool are to form the work-piece and extract heat from it at a high rate [19]. For 22MnB5 manganese-boron steel, the minimum value of quenching rate required to achieve full martensite is for the undeformed state, and is 27K/s [16]. An additional attribute of a tool is that it should enable a part with, as near as possible, uniform thickness to be produced. Thus, tool design has to be associated with careful consideration of both material flow and heat transfer.

A section of the tool is presented in Figure 3.6 to schematically illustrate its working mechanism. To well arrange the material flow, the top die was designed to be composed of two parts. The

main part of the top die (sides in Figure 3.6) was fixed to the ram of the press and the punch was seated on gas springs, to allow it relative movement. Figure 3.6 (a) shows the start of forming when the work-piece was in contact with the punch. With the whole top die set moving down, the middle groove was formed and, as shown in Figure 3.6 (b), the punch was brought to rest by the counterpunch while the sides continued to move downwards until the part was fully formed, as shown in Figure 3.6 (c). Arrows in solid lines represent forming occurring under the particular tool part. Little stretching of the blank occurred and it was subjected to near pure bending. Since heat transfer coefficient depends on contact pressure, tight contact between work-piece and tool is essential. In this design, see Figure 3.6 (c), the flexible top die set guaranteed tight contact over the interfaces ①, ②, and ③. In addition, two side parts of bottom die were also adjustable, which made sure tight contact over the interfaces ④ and ⑤. An additional feature of the tool was that beams with different groove depths could be formed, by changing the thickness of a replaceable block in the counterpunch.

A 3-D drawing of the assembled tool set is given in Figure 3.7. Since the tool set was for laboratory application instead of mass production, no water cooling channels were needed in the dies. The dies were made of AISI type H13 hot work tool steel. The die clearance was 0.1mm (6.25%), for the work-piece in 1.6mm thickness.

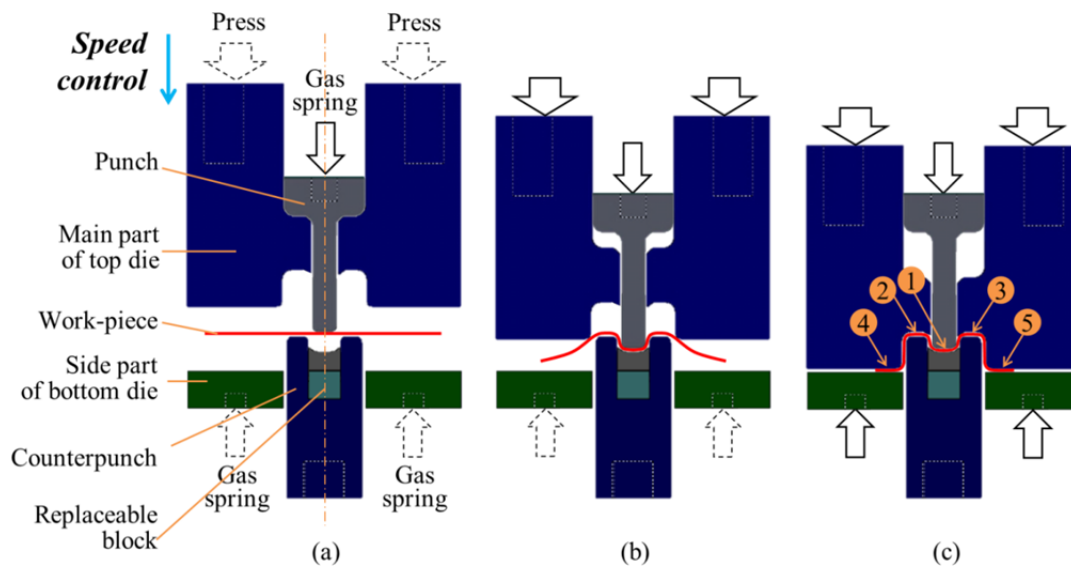


Figure 3.6 Schematics illustrating the working mechanism of the tool set and material flow of the work-piece (a) Start of forming (b) during forming, middle groove has been formed (c) final stage of forming

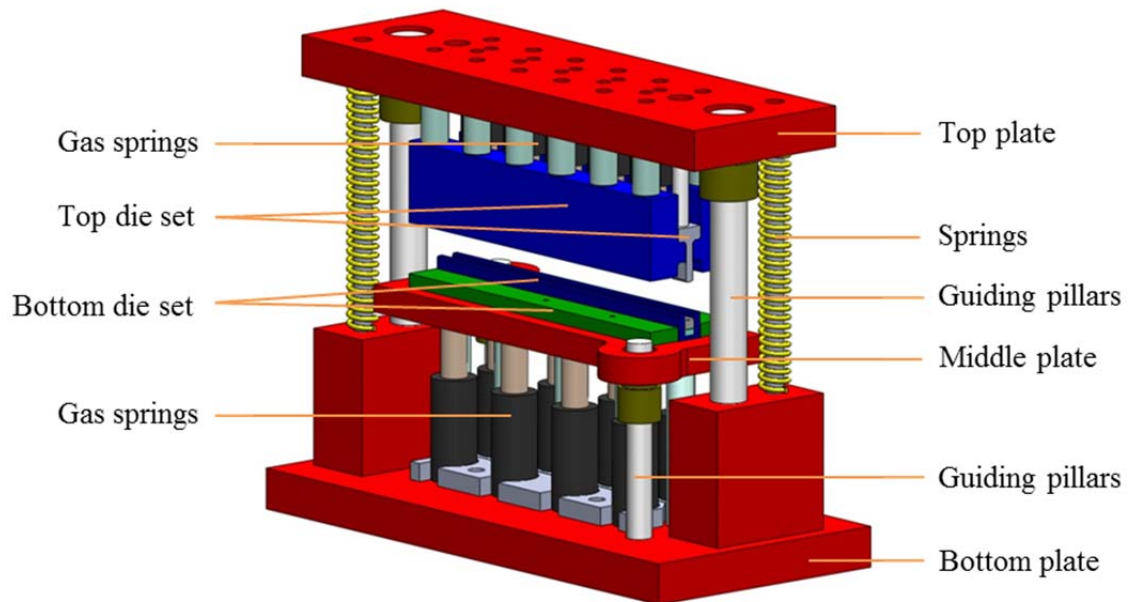


Figure 3.7 Isometric view of the hot stamping and cold die quenching tool set

3.4.2 Hot stamping experiments

Hot stamping experiments were carried out on a 1000kN hydraulic testing machine. The set-up of facilities is shown in Figure 3.8. The furnace was used for heat treatment of work-pieces determined as described in the previous section. The controller was used to operate the machine. A load cell was set on top of the tool set to measure the forming force. The forming speed was 150mm/s, which was determined to be appropriate to industrial processes, giving an average strain rate of 0.5/s approximately. Forming force and punch displacement were monitored through a digital work station, to ensure that the load provided by the machine was sufficient and the forming speed was accurate. The time for transferring blanks to the tool set was controlled at about 3 seconds. The times for positioning and forming were about 1 and 0.2 seconds respectively. Formed parts were held in dies for about 20 seconds.

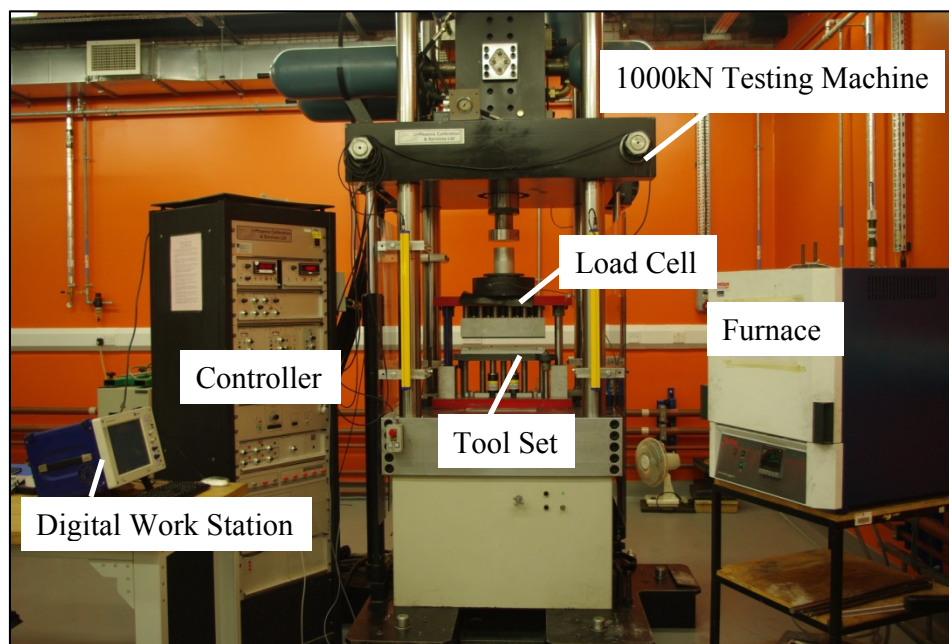


Figure 3.8 Set-up of facilities for hot stamping experiment

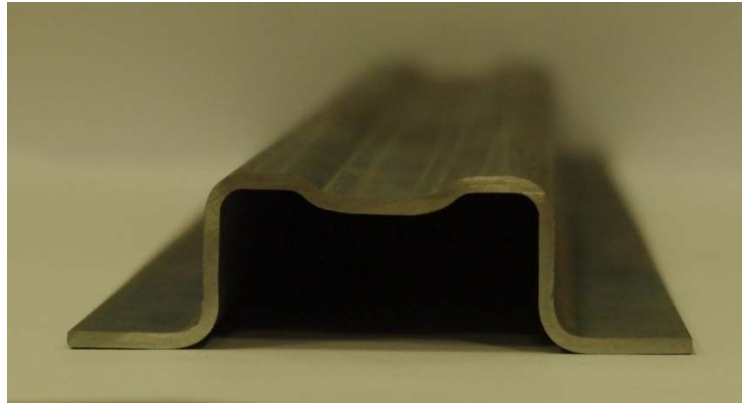


Figure 3.9 View of the cross-section of a formed product

Figure 3.9 shows the cross-section of a formed product. Products with different microstructural topographies all have good qualities without visible spring-back. This suggests that, even without a phase transformation, the residual stress in the part could be eliminated by holding and quenching within closed cold dies.

3.5 Microstructural distribution analysis

3.5.1 Hardness testing

Hardness testing was conducted on as-formed parts, to confirm complete martensitic transformation had been achieved through the cross-section of the prior hot zone, and to detect the microstructural distribution along the length of parts which have been selectively heat treated. The Vickers hardness values of the studied boron steel are ≥ 475 HV for martensite and 160 HV for as-delivered initial phase [21].

Hardness values from twenty positions through the cross-section of an S-320mm formed part are plotted in Figure 3.10. The numbering of locations for indentation on the half section (Side A) is shown in the figure. Due to the section being symmetrical, the numbering system is mirrored on side B. It can be seen that all hardness values are 520 ± 20 HV, indicating a full martensite distribution along the section. This implies good contact between the hot part and tool.

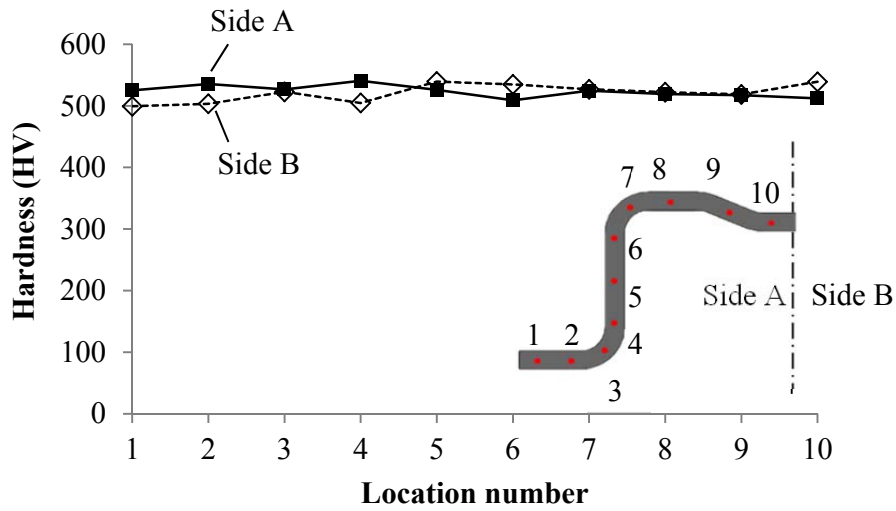


Figure 3.10 Hardness distribution through a cross-section of an S-320mm as-formed part

Hardness tests were undertaken along the lengths of the top surfaces of flanges, 1.5mm from the edges, of S-60mm and S-100mm formed parts. In Figure 3.11, values of Vickers hardness are plotted on a length scale, where the beam mid-length is taken as origin. For both the parts, full martensite was achieved in the prior hot zones with hardness values of 520 ± 10 HV, which suggests full austenitization have been achieved in pre-heating. Away from hot zone at both sides, the inter-zone regions with gradually decreasing hardness values are transition zones having graded multiphase microstructures. The region with almost constant hardness values of 175 ± 5 HV at left end indicates that the initial phase retained without phase transformation. Hardness values on the right side show a little higher level for each part. This was due to a higher temperature at the back of the heating blocks in the furnace resulting from reduced air convection.

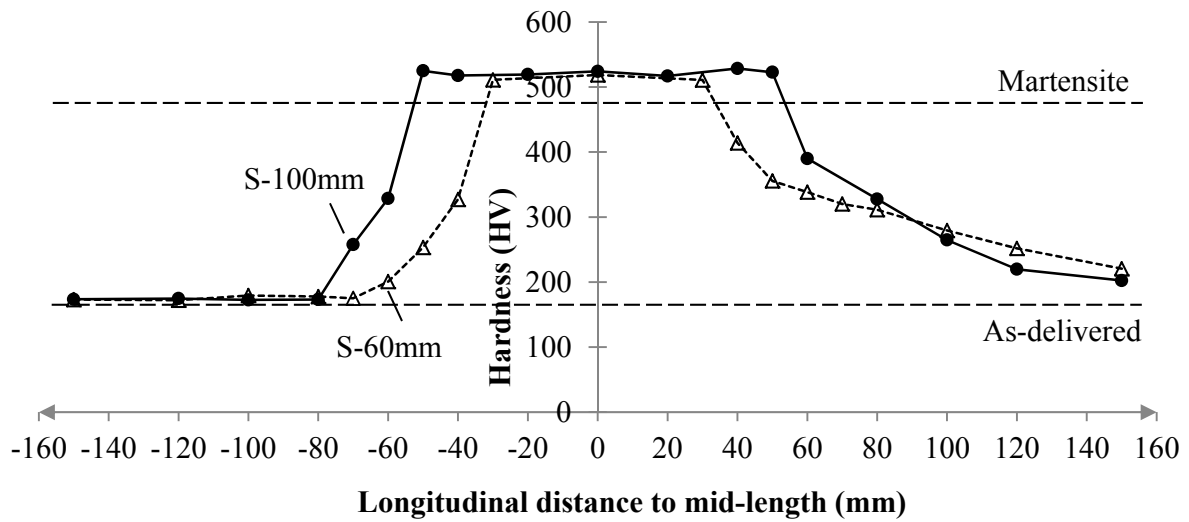


Figure 3.11 Hardness distributions along the longitudinal direction of S-60mm and S-100mm as-formed parts

3.5.2 Microstructural observation

In order to further confirm the tailored microstructural distribution, assumed from hardness tests, in the selectively heat treated parts, microstructural observation were carried out on an S-100mm as-formed part. According to the hardness distribution in Figure 3.11, the left side of the beam can be divided into three zones having different microstructures: initial phase zone (-160mm – -80mm), multiphase zone (-80mm – -50mm), and martensite zone (-50mm – mid-length). For each zone, a piece of steel was cut from the flange area and sectioned through thickness for SEM (Scanning Electron Microscope) observation. Typical micrographs for the three phase states are presented in Figure 3.12.

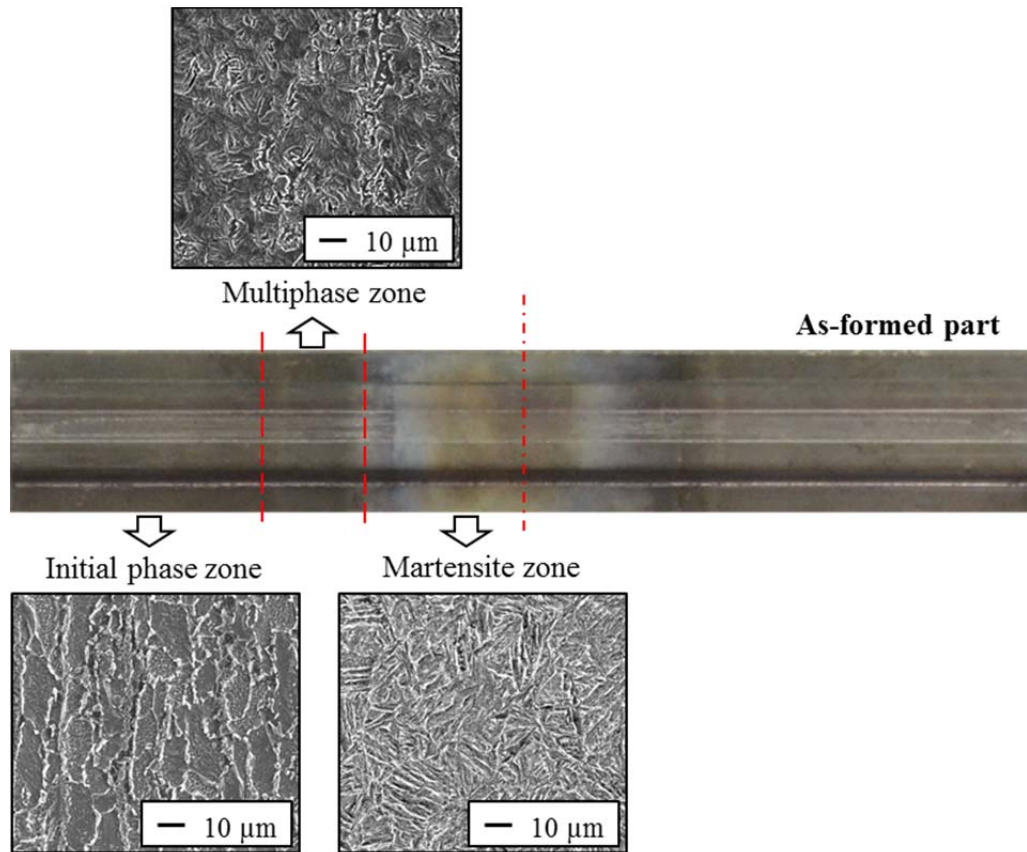


Figure 3.12 Typical SEM micrographs of boron steel from different microstructure zones
(sampled from flange edge) of an S-100mm as-formed part

3.5.3 Discussion

Microstructural distribution varies with many factors consisting of both material thermal properties and thermal conditions, such as thermal conductivity of the alloy, distribution of heating temperature, and soaking time. Besides control of the martensite and initial phase, there is much room to grade the microstructures in transition zones. For example, in this work, the gradient of hardness corresponding to warm zones was affected by air convection.

In this section, graded microstructural distribution in as-formed parts achieved through the selective heating and press hardening strategy are presented qualitatively, and the feasibility of microstructural design by tuning thermal conditions is demonstrated. This provides the basis for

optimising structural properties of a part. To attain the tight quantitative process control required to optimise mechanical property distribution, the relationships between thermal conditions and microstructure, as well as microstructure and mechanical properties, must be known. This is achieved in the studies of fundamental mechanics of austenite formation reported in following chapters.

3.6 Structural performance assessment

3.6.1 Three point bending tests

To assess the load bearing performance of the as-formed parts, three point bending tests were conducted on an INSTRON (5585H) 250KN universal test machine. The flex fixture can be seen in Figure 3.13. The beams were 320mm long, loaded in the middle by an indenter with 40mm diameter. The indenter speed was 0.5mm/s.

3.6.2 Results and discussion

Figure 3.13 shows the failure modes of as-formed boron steel beams with different microstructural topographies. For beams with a uniform microstructure, failure took place at the indenter, where the bending moment was the maximum. For beams with graded microstructures, the local instability initiated at a position away from the hard (martensite) zone, in a region associated with mixed microstructural phases and therefore a range of mechanical properties. This suggests that the deformation mode of a part can be adjusted through microstructural arrangement, for specific functional requirements.

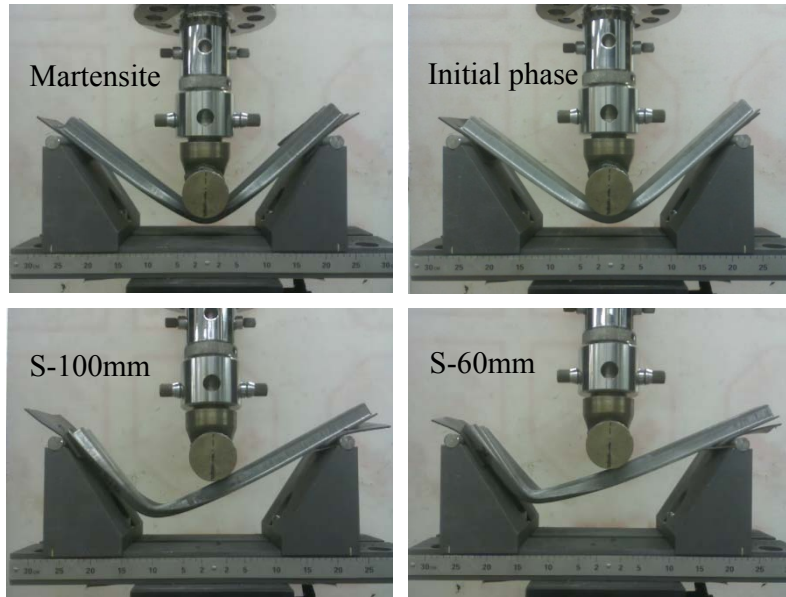


Figure 3.13 Failure modes under bending for boron steel parts having different microstructural topographies

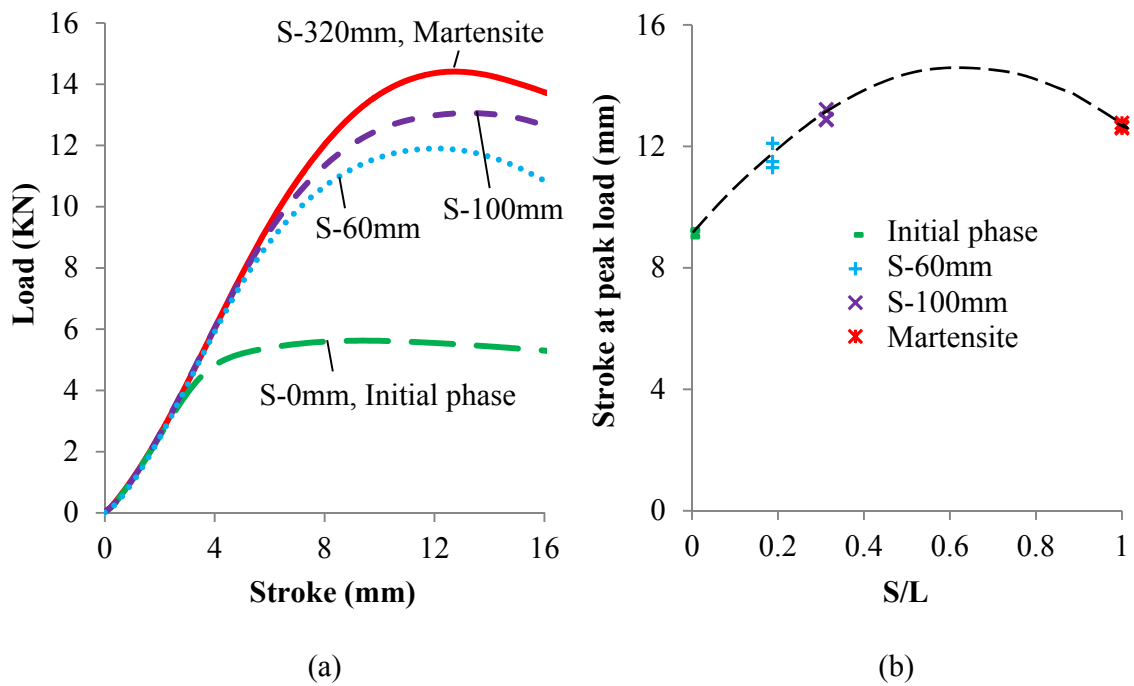


Figure 3.14 Load bearing performance of boron steel parts having different microstructural topographies: (a) Load deflection curve (b) Stroke at the onset of instability against the proportional length of full martensite phase

Figure 3.14 (a) shows the load deflection curves of the beams corresponding to the four microstructural topographies. The fully hardened beam (S-320mm) sustained the highest load which was about three times that for the beam with initial phase (S-0mm). The beam S-100mm endured a lower load than beam S-320mm but deformed more before onset of instability. This behaviour can be attributed to the existence of advantageous portions of strong and ductile regions in the beam. Figure 3.14 (b) shows the relation between degree of stable deformation and length of full martensite phase. Three data points are plotted for each condition. From the curve it can be inferred that the greatest energy absorption (high load and large stable deformation) is obtained for an S/L value of between 0.6 and 0.7. In addition, the performance of a beam with tailored properties might be improved if it contained a more symmetrical microstructural distribution and a better graded multiphase zone.

Since the functional requirements are various in a car-body, the implementation of tailored solutions should always be adapted to a specific requirement and load situation in applications. This will be facilitated by the accurate prediction of material behaviours through materials modelling, which again addresses the importance of further fundamental studies.

3.7 Summary

In this chapter, selective heating and press hardening strategy has been successfully implemented in a hot stamping operation. Demonstrator parts with either full martensite phase, full initial phase, or differentially graded microstructures, and of apparent high quality, have been formed. Microstructural distributions in as-formed parts have been exhibited by hardness testing and SEM microscopy. The structural performance of as-formed parts under three point bending has been determined.

CHAPTER 4 EXPERIMENTAL PROGRAMME OF FUNDAMENTAL TESTS

4.1 Introduction

In this chapter, following the experimental studies for proving the feasibility of the selective heating and press hardening strategy, three sets of fundamental tests are introduced. The first is heat treatment testing to investigate the austenite formation in the boron steel during heating; the second is hot uniaxial tensile testing to characterise the thermo-mechanical properties of the boron steel, in the austenite phase and initial phase, corresponding to hot stamping conditions; the last is uniaxial tensile testing at room temperature combined with hardness testing and microstructural observation, which is to study the effects of strain rate and phase composition on the mechanical properties of press-hardened boron steels.

All specimens used for the tests were machined from the same batch of as-delivered, 1.6mm thick, boron steel sheet. Information on properties of the sheet is provided in Chapter 3. The individual experimental programme and related testing facilities are introduced in the following sections. In order to prove the repeatability, at least three tests were completed for each test condition for all the three sets of experiments.

4.2 Austenite formation

The objective of this set of experiments is to gain a better understanding of the kinetics of the austenite formation in the boron steel, and evaluate the effects of heating rate and soaking temperature on the process. The formation of austenite under both continuous heating and isothermal soaking conditions, which were designed to accord with the thermal cycle of selective

heating for hot stamping processes, has been investigated through heat treatment tests and dilatometry.

4.2.1 Test equipment and specimen design

A Gleeble 3800 thermo-mechanical materials simulator was employed for the heat treatment tests. It consists of a control console, a test chamber (shown in Figure 4.1) and a control computer. The fully integrated digital closed loop controlled testing system ensures accurate process control, and has the capability for phase transformation to be monitored using a dilatometer.

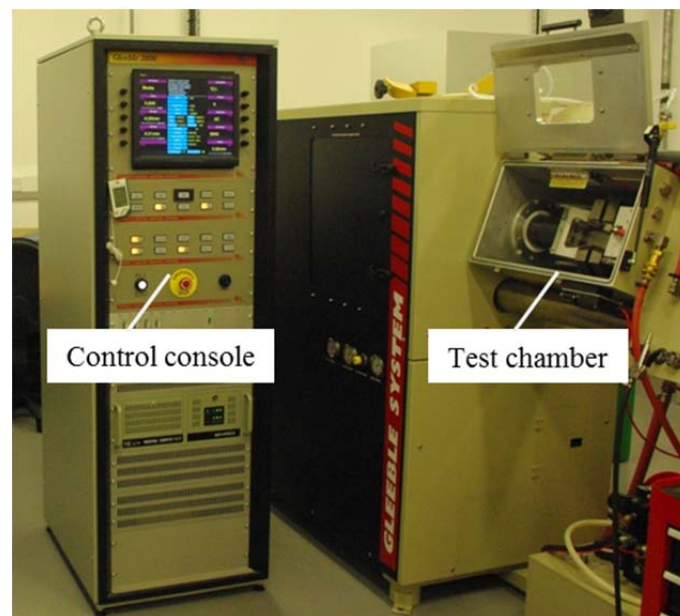
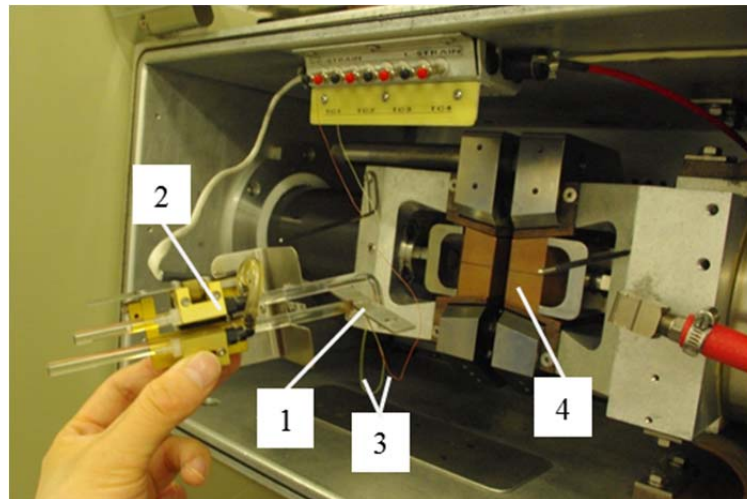


Figure 4.1 Gleeble 3800 thermo-mechanical materials simulator

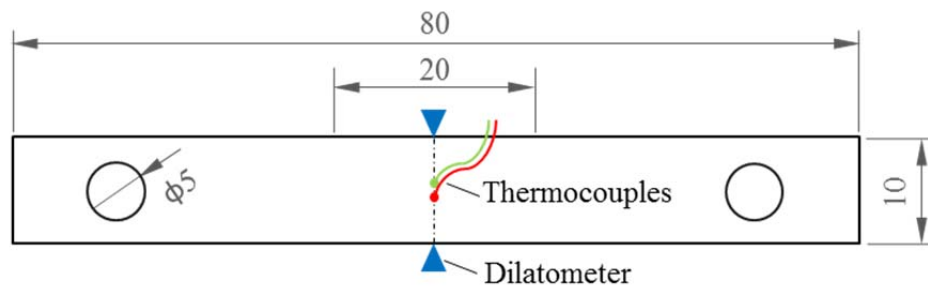
Figure 4.2 (a) illustrates the test set-up in the chamber. For testing, the strip specimen (No.1) was fixed between the grips (No.4), where it was resistance heated with a large alternating current at a low voltage. Copper grips (No.4) enabled fast quenching of specimen through contact heat transfer and ensured better stability than air/water quenching. For presentation in the figure, the specimen (No.1) was taken out from the grips, the attachment of the dilatometer (No.2) and thermocouples (No.3) can thus be seen. A high resolution dilatometer (No.2) was employed to

measure the width change of specimen during thermal cycles, from which the phase transformation can be detected. A pair of K-type thermocouples (No.3), which enables accurate temperature measurement up to 1573K, was used to provide signals for feedback control of specimen temperatures.



1-Specimen; 2-Dilatometer; 3-Thermocouples; 4-Grips

(a) Test chamber and specimen with dilatometer and thermocouples attached



(b) Specimen design (dimensions are in mm, gauge length is 20mm) with schematic dilatometer and a pair of thermocouples attached

Figure 4.2 Test set-up and specimen design

Figure 4.2 (b) schematically shows the specimen design and the location of attachments in detail: The initial width of the specimen was 10mm; subtracting a 30mm long gripping section at each side, the gauge length was 20mm. The reason for defining the short gauge length was to enable

quick heat transfer during the quenching process. The dilatometer was clamped in the middle of the specimen so as to measure width change. The thermocouples were welded on the centre of a specimen surface.

4.2.2 Test programme

Heat treatment conditions were designed to match the thermal cycle used in practice for hot stamping of boron steels, which comprises continuous heating, isothermal soaking and quenching. Figure 4.3 shows the test programme of heat treatments with different heating conditions.

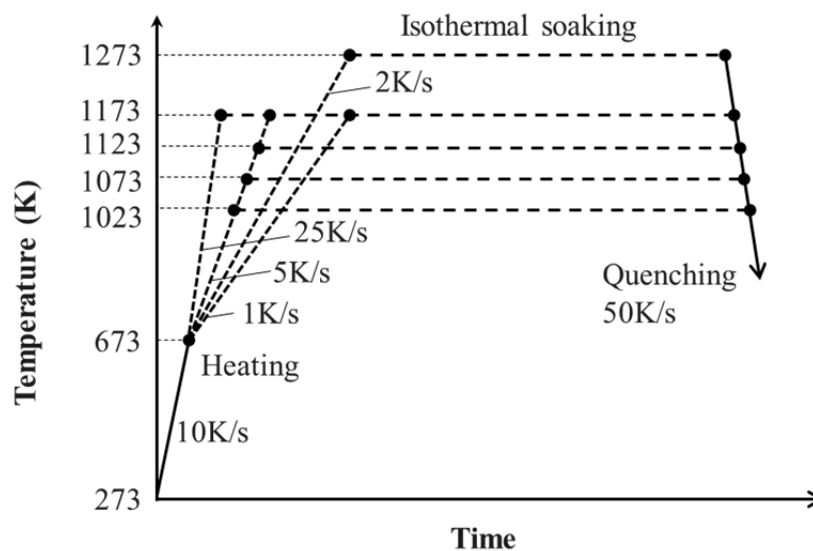


Figure 4.3 Test programme of heat treatments with different heating rates and soaking temperatures

Starting from a given initial microstructure, the heating rate and soaking temperature are the two critical factors which affect the kinetics of austenitization. In order to study the effects of them under both non-isothermal and isothermal conditions, two groups of test programmes were designed. In the first group, specimens were heated to 1173K at different heating rates from 673K (the heating rate has no influence at lower temperature). Long soaking periods were given

to enable thermodynamic equilibrium to be achieved. These were 10min for 1K/s and 15min for 5K/s and 25K/s. In the second group, specimens were heated at the heating rate of 5K/s to different soaking temperatures of 1023K, 1073K, 1123K, and 1173K, and soaked for 15mins to enable the austenite formation taking place.

In addition, a separate test programme was designed for the third group: a specimen is heated up to 1273K at a heating rate of 2K/s and soaked for 2 minutes without reaching saturation of austenite. This test was used for the validation of austenite formation model which is presented in Chapter 6.

After specimens were subjected to the designed heating and soaking periods, all of them were quenched at a cooling rate of 50K/s, which ensured complete transformation from austenite phase to martensite phase. The critical cooling rate for martensitic transformation from austenite is 27K/s, according to the material supplier.

4.3 Thermo-mechanical properties at elevated temperatures

The objective of performing this set of experiments was to simulate the deformation of the boron steel in a state corresponding to hot stamping after selective heating, so as to characterise the effects of temperature and strain rate on its viscoplastic behaviour. The thermo-mechanical properties of the boron steel in two representative microstructural states, austenite and the initial phase (ferrite and pearlite), have been studied through hot tensile tests.

4.3.1 Test equipment and programme

The Gleeble 3800 materials simulator was employed for the hot tensile tests. It has a load capacity of 100kN and a maximum stroke rate of 2m/s in tension. As for the set-up for heat treatment tests, specimens were mounted between grips in the chamber, heated and stretched.

The dilatometer and thermocouples were used to measure width changes and temperatures of specimens, respectively.

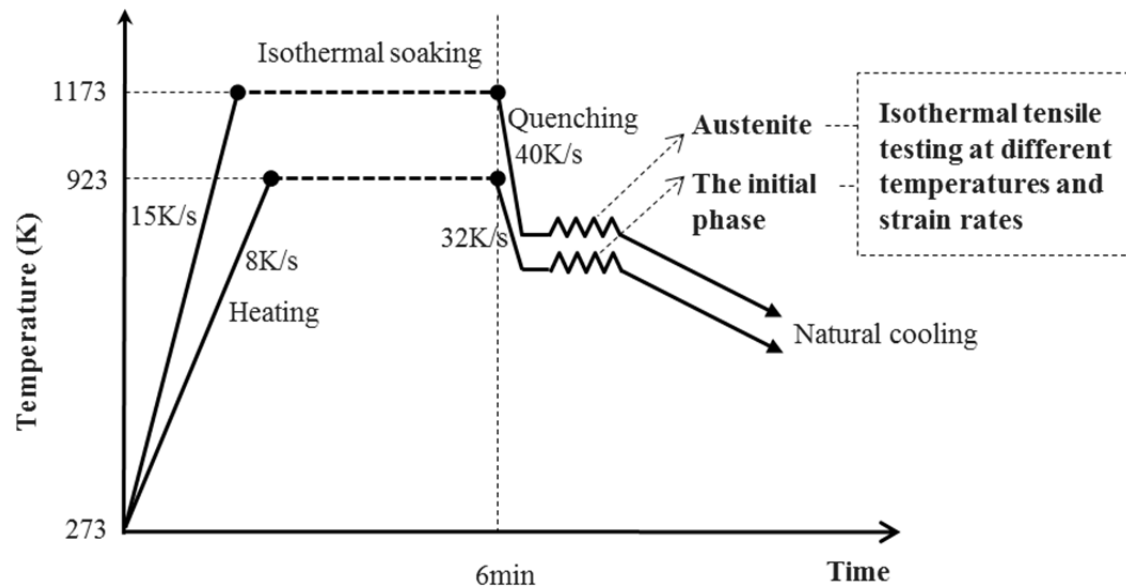


Figure 4.4 Temperature-time profiles for isothermal tensile testing of boron steels in both austenite (soaked at 1173K) and the initial phase (soaked at 923K)

Figure 4.4 presents two groups of temperature-time profiles designed for isothermal tensile testing of the boron steel in the austenite and initial phase at elevated temperatures. In the first group, the heating route was suggested by the steel supplier for full austenite formation: 15K/s heating rate, 1173K soaking temperature and 5 minutes soaking time. In the second group, the soaking temperature was defined as 923K, which ensured no phase transformation taking place during the heating process. According to the real condition of selective heating, a lower heating rate of 8K/s was defined. In order to make sure the heating periods of the two groups were of same length (6 minutes), soaking time was determined as 4 minutes and 38.75 seconds. After the heating step, specimens were quenched to a certain temperature for isothermal deformation. Cooling rates of 40K/s and 32K/s were defined for the austenite and the initial phase respectively,

which are similar to the real corresponding cooling rates during transfer of work-pieces to dies in practice.

The isothermal uniaxial tensile tests were conducted at various temperatures and strain rates, within a temperature range of 873K to 1073K for austenite and 723K to 923K for the initial phase, and a strain rate range of 0.005/s to 5/s for both, to cover the typical conditions for hot stamping of boron steels. Matrices of test programme for the two phase states are listed in Table 4.1.

Table 4.1 Test programme ('√' represents the selected test conditions)

	Temperature (K)	Strain rate (/s)			
		0.005	0.05	0.5	5
Austenite	1073			√	
	973	√	√	√	√
	873			√	
The initial phase	923	√	√	√	√
	823			√	
	723			√	

4.3.2 Specimen design and test procedure

4.3.2.1 Specimen design

The design of the dog-bone type specimen is shown in Figure 4.5. The width and parallel length of the gauge section were 6mm and 30mm, respectively. Specimens were machined from the same piece of as-delivered sheet in the rolling direction.

A dilatometer was clamped in the middle of the specimen to measure the width strain associated with deformation. Three pairs of thermocouples were welded on the mid-width line of the specimen along the gauge section: T1-mid-length, T2-5.5mm from mid-length, and T3-11mm from mid-length. T1 was used to control specimen heating, T2 and T3 were used to monitor the temperature distribution along the specimen in the longitudinal direction.

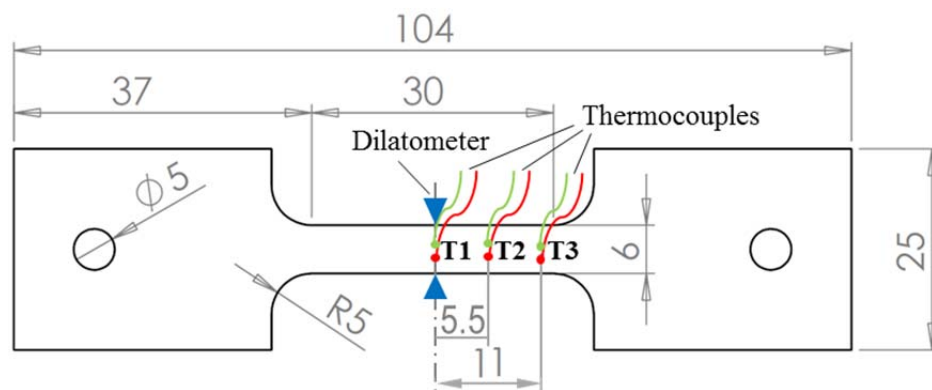


Figure 4.5 Specimen design (dimensions are in mm) with schematic dilatometer and three pairs of thermocouples attached

4.3.2.2 Temperature gradients in the longitudinal direction

Due to the resistance heating conditions on Gleeble, the temperature is not uniformly distributed along the gauge length. It reached the highest value, equal to the programme controlled temperature, at the midway and dropped gradually to both sides. Since the failure position for

many tests did not precisely lie on the middle of specimen, it was important to evaluate the error by detecting the temperature gradient.

Figure 4.6 (a) and (b) respectively present the temperature distributions measured using thermocouples T1, T2 and T3 for the deformation of austenite and the initial phase at different testing temperatures. For the testing on austenite in Figure 4.6 (a), assuming temperature distributions were symmetric with respect to the mid-length of a specimen for any testing temperature, the temperature drop of less than 10K could be achieved within ± 1 mm offset from mid-length. Thus, to ensure the accuracy of testing results, only tests with failure taking place within this offset were taken as valid. Similarly, the threshold for the testing on initial phase, in Figure 4.6 (b), was within ± 1.5 mm.

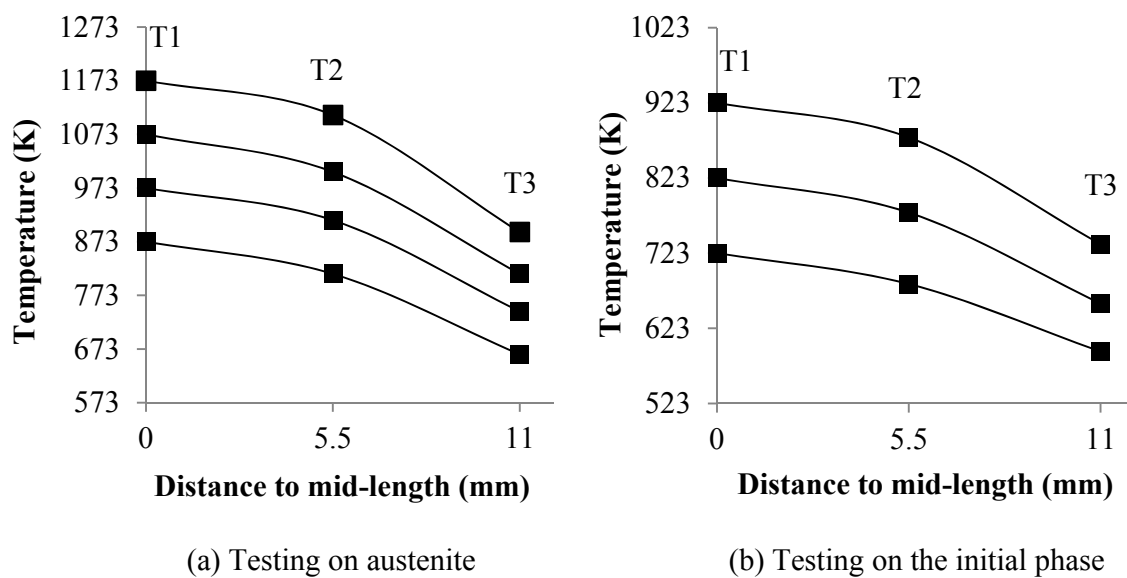


Figure 4.6 Temperature distributions along the specimen in the longitudinal direction at different testing temperatures

4.3.2.3 Control of strain rate

True (also called natural or logarithmic) strain is adopted for the analysis of large deformation at elevated temperatures in this study. Accurate control of true strain rate is vital for the

characterisation of strain rate effects on the viscoplastic behaviour of the boron steel. Efforts have been made to achieve high accuracy in two aspects:

- Ensure constant true strain rates

Constant testing speed cannot achieve constant true strain rate during deformation. The true strain in the longitudinal direction (effective true strain) can be determined from the dilatometric measurement by:

$$\varepsilon_T = -2\ln\left(\frac{W}{W_0}\right) = -2\ln\left(1 + \frac{\Delta W}{W_0}\right) \quad (4.1)$$

where W_0 is the initial specimen width, W is the instantaneous width, and ΔW is the dilatometric measurement (the width change). However, real-time strain rate control based on the dilatometric measurement was not practical on the testing machine. Therefore, length control was made by defining a stroke-time curve in the test programme based on true strain definition. It was given as:

$$\Delta l = l_0 [\exp(t \cdot \dot{\varepsilon}_T) - 1] \quad (4.2)$$

where l_0 is the initial specimen gauge length, Δl is the stroke (the length change), t is time, and $\dot{\varepsilon}_T$ is the defined true strain rate. Thus the specimen could be tensioned at a constant true strain rate before necking took place.

- Determine effective gauge length for proper input

Due to temperature gradients, the steel experienced different extents of deformation at different sections. Figure 4.7 presents a fractured specimen. The locations of T1, T2, T3 and end of parallel length, which were initially 0, 5.5mm, 11mm, and 15mm from mid-length, reveal that larger deformation occurred closer to the mid-length. Therefore, if the stroke-time curve is given by taking the parallel length 30mm as l_0 in formula (4.2), the real strain rate measured in the mid-

length will be much larger than the defined $\dot{\epsilon}_T$. To realize the defined value of strain rate in the middle of specimen, a smaller l_0 should be defined, as the effective gauge length, to determine the input stroke-time curve.

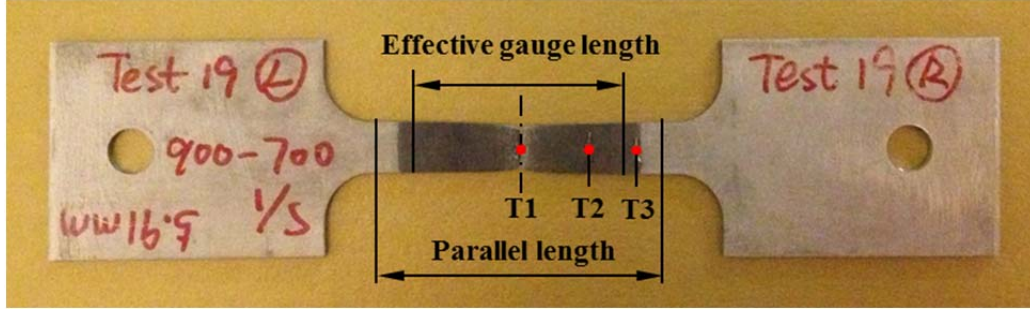


Figure 4.7 Deformation on a fractured specimen

A method to determine the effective gauge length by trial and error was proposed: for a test condition of defined true strain rate $\dot{\epsilon}_T$, firstly, the input stroke-time curve was determined by giving an initial value of effective gauge length l_0 (can be 30mm). Then, the real value of true strain rate $\dot{\epsilon}_T'$ was determined by linear regression of true strain and time (the section before necking), where the data of true strain with time was obtained from dilatometric measurement (equation (4.1)). Last, a corrected value of effective gauge length (l_0') was updated by: $l_0' = l_0 \dot{\epsilon}_T / \dot{\epsilon}_T'$. Higher accuracy can be achieved through more iteration. It is noted that a fixed value of effective gauge length could not meet all the test conditions. This was because the temperature gradient varied with the value of control temperature (see Figure 4.6); in addition, even for a same temperature gradient, the strain distribution varied with the deformation rate due to viscoplastic properties. With consideration of the efficiency, determination of l_0 for each test condition is not necessary. In this work, a value of 20mm was defined, whereby variations of strain rates from designed values were small for all tests. To enhance the accuracy of result analysis and materials modelling, the real value of strain rate that each specimen experienced could be calculated individually according to test measurements.

4.4 Mechanical properties at room temperature

This set of experiments was designed to investigate the mechanical properties of the boron steel consisting of different microstructural phases, for a large range of deformation speeds at room temperature. This was in order to evaluate the crashworthiness of press-hardened boron steel parts having graded microstructural distributions. The experimental work can be divided into two groups: the first group is to characterise the effect of strain rate on the tensile properties of the martensite phase and also the initial phase (ferrite and pearlite), of the boron steel via both quasi-static and dynamic tensile testing; the second group was to study the effect of phase composition (volume fraction of martensite) on the mechanical properties via quasi-static tensile testing, hardness testing and microstructural observation.

4.4.1 The first group: tensile testing over a range of strain rates

Boron steel in both martensite and the initial phase were tested over a wide range of strain rates from 0.001/s to 500/s which is relevant to a typical vehicle crash [125-127]. Common quasi-static material testing is in the range of strain rates 10^{-4} – 10^{-1} /s; dynamic testing starts at strain rates above 10^{-1} /s when inertia effects become important [126]. When strain rate is above 10^2 /s, which is normally classified as high rate testing, the effect of stress wave propagation should be considered [126, 128]. The stress oscillation caused by the impact of loading system increases with increasing strain rate [128, 129]. In order to obtain valid stress-strain data over the whole testing range, a careful selection or design of the testing machine, clamping system, specimen, and measurement method is critical.

4.4.1.1 Design of experiment and specimen

- Testing machines

For testing at quasi-static conditions, a screw-driven INSTRON testing machine was used. It had 250kN load capacity and 0.001–500mm/min speed range.

For dynamic testing, a servo-hydraulic high rate INSTRON testing machine was employed. It was capable of loads up to 20kN and velocities up to 25m/s.

- Stress measurement

Stress during tension was obtained by measuring load by different means. For quasi-static testing, the load was simply measured through the machine-inbuilt strain gauge load cell. For dynamic testing, a commercial piezoelectric load washer with higher response frequency was adopted. It was able to provide accurate measurement when the testing rate was relatively low. With increasing testing speed, in order to reduce the stress wave propagation effect, the load cell should be placed as close as possible to the specimen [126]. Thus, for the strain rate of 50/s and more, a strain gauge was attached to a gripping section of a specimen to create a transducer and directly measure the load. This measurement method resulted in reduced load oscillations and provided increased frequency response.

- Strain measurement

Conventional contact strain measurement (e.g. extensometer) is not applicable for high rate tensile testing due to inertia effects and low response characteristics [130]. Therefore, an optical technique of DIC (digital image correlation), in which the movement of coloured spatters sprayed on a specimen are recorded with a camera, was adopted in this work. For dynamic tensile testing, a PHOTRON SA-1 digital high speed camera was employed. It was capable of 5,400 fps (frames

per second) for full resolution of 1024×1024 pixels, and up to 675,000 fps maximum by reducing resolution to 64×16 pixels [131].

- Specimen design

Figure 4.8 shows the geometry of the dog-bone type specimen for the tests: the gauge width was 3mm and the parallel length was 18mm. The reasons for designing a small specimen were: for a certain testing speed, a smaller parallel length enables a higher strain rate; since the martensitic boron steel is of ultra-high strength, the gauge width should be small enough to ensure the specimen fractured within the 20kN load capacity; with consideration of the second group of tests, a small gauge section was required to ensure uniform microstructural distribution (detailed explanation of this is given in section 4.4.2.1). For strain gauge attachment, the tensile specimen was designed with a longer grip section at one end. The position of the strain gauge on a specimen can be seen in the figure.

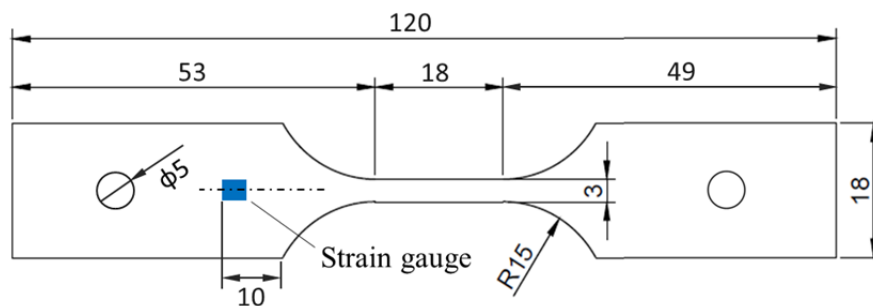


Figure 4.8 Specimen design (dimensions are in mm) with a schematic strain gauge attached

- Test programme

Boron steels in each of the two phase states were tested under the same conditions. For each one, the designed strain rates, as well as the corresponding testing machine and stress/strain measurement devices, are listed in Table 4.2. It is to be noted that all the defined strain rate values refer to initial strain rates under the constant speed control used in this set of tests.

Table 4.2 Matrix of test programme and facilities

Strain rate(/s)	Tensile Speed (mm/s)	Testing Machine	Stress measurement	Strain measurement
0.001	0.018	Screw-driven INSTRON	Conventional strain gauge load cell	Digital Image Correlation (DIC)
0.05	0.9			
5	90	Servo-hydraulic INSTRON	Piezoelectric load washer	DIC with high speed camera
50	900		Strain gauge attached on specimen	
200	3600			
500	9000			

4.4.1.2 Specimen preparation

The preparation of specimens was complicated and of great importance in this work. The procedure was divided into four steps as follows (step 3 was needed only for strain rates 50-500/s):

- Step 1 - Heat treatment

To obtain full martensite phase and the initial phase (ferrite and pearlite) equivalent to the press hardened state, as-delivered boron steel sheets were respectively heated in a furnace to 1173K and 993K for 5-minute soaking, and then quenched using cold steel blocks.

- Step 2 - Machining

The heat treated sheets were machined into tensile specimens using Wire EDM (Electrical Discharge Machining). The edges of gauge sections were polished to remove machining affected material or geometric defects.

The manufacturer applied coating on one surface of the specimen gauge section was removed using a sandblaster (the reason is explained in step 4). The influence on material strength was negligible.

- Step 3 - Strain gauge attachment

To measure the load during tensile testing at high rates, a strain gauge was mounted on the specimen. The procedure is outlined: First, strain gauge was positioned in the gauging area of specimen (shown in Figure 4.8), which had been carefully cleaned, and adhesive was applied. Perfect alignment along the midline was required for data accuracy. Second, the specimen, with pressure applied on the gauging area using a spring clamp, was cured in a furnace at 383K for 4 hours for thorough bonding of the strain gauge. Last, lead-wires were soldered to the strain gauge tabs in order to make electrical connections to strain gage circuits for testing.

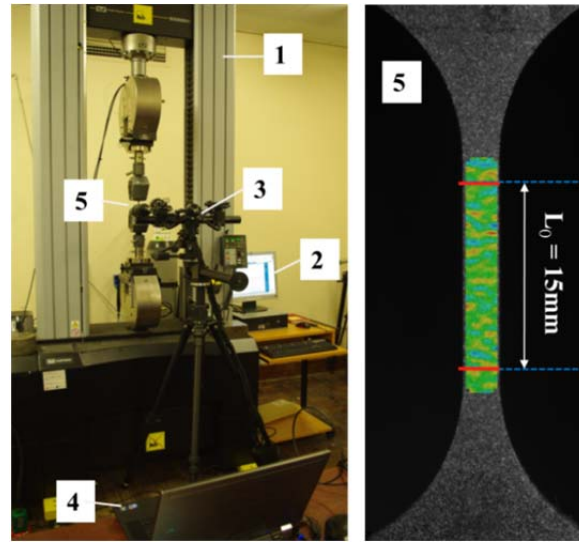
- Step 4 - Painting

To measure the strain during testing, the specimen surface was stochastically marked by a white spray against a black painted background. The speckle patterns provided grey scale contrast for the image correlation method [132]. The paint was applied to the steel surface with the manufacturer's coating removed, because the coating tended to become detached under large deformations, due to its low ductility at room temperature.

4.4.1.3 Set-up and procedure for quasi-static tensile testing

Figure 4.9 shows the set-up for quasi-static tensile testing. Tests were performed on the screw-driven INSTRON testing machine. The INSTRON control system was used to determine the strain rate by controlling the crosshead speed, and record the load data measured by the strain gauge load cell equipped in the machine. A DIC (Digital Image Correlation) integrated system was set up to measure the strain field during the testing. For the flat specimen, just one camera

was needed for two-dimensional DIC. The frame rate of camera was set as 1 fps and 25 fps for the strain rate of 0.001/s and 0.05/s, respectively. Two LED lights were employed for illumination. In the DIC control system, the analytical tool ARAMIS was used to run the sensor and controller, and process strain measurements.



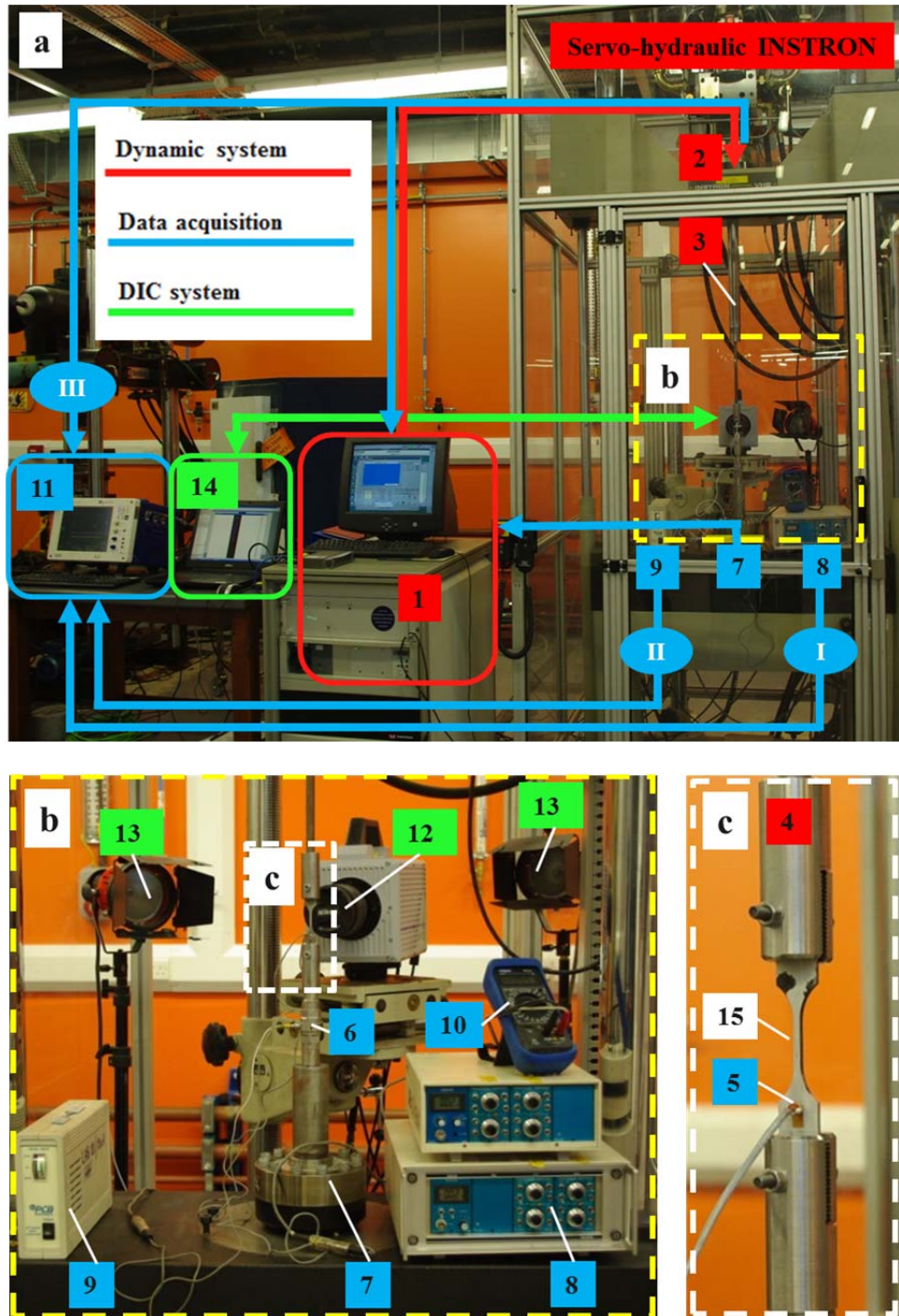
1-Screw driven INSTRON machine; 2-INSTRON control system; 3-Cameras and LED lights;
4-DIC control system; 5-Specimen and the DIC focused gauge section

Figure 4.9 Set-up of facilities and specimen for low rate tensile testing

The enlarged view of No.5 in Figure 4.9 shows the initial state of a specimen with stochastic speckles and the DIC processed strain field on the gauge section. To avoid the geometry effect of the shoulders and ensure uniform deformation distribution before necking, the gauge length was defined as 15mm, which was less than the parallel length of 18mm. Engineering strain in tensile tests is given by:

$$\varepsilon_E = \frac{L}{L_0} - 1 \quad (4.3)$$

where L_0 is initial gauge length and L is the instantaneous gauge length. Values of L could be obtained through DIC post-processing, thus the evolution of engineering strain with time was obtained.



1-Control system of the Servo-hydraulic INSTRON; 2-Actuator; 3-Slack adaptor; 4-Grips;
 5-Strain gauge; 6-Piezoelectric load washer; 7-Strain gauge load cell;
 8-Strain gauge transducer amplifier; 9-Amplifier; 10-Multimeter; 11-Digital work station;
 12-High speed camera; 13-Lighting system; 14-DIC control system; 15-Specimen

Figure 4.10 Set-up of facilities and specimen for dynamic tensile testing

4.4.1.4 Set-up and procedure for dynamic tensile testing

Figure 4.10 shows the experimental set-up for dynamic tensile testing carried out on the servo-hydraulic INSTRON machine. The elements in the figure can be classified into three systems according to their functions: the dynamic system, marked in red, is for the loading of specimens; the data acquisition system, marked in blue, is for recording signals of load and actuator displacement; the DIC (Digital Image Correlation) system, marked in green, is for strain measurement. Arrows indicate the direction of control commands or data flow. Sub-figure (b) is the partially enlarged view of (a), and (c) is the partially enlarged view of (b). Details about each system are explained as follows:

- Dynamic system

For the dynamic loading process, proper input speed and clamping mechanism are critical to ensure the accuracy of data [130]. Figure 4.10 shows the load train which consists of an actuator (No.2, see sub-figure (a)), a slack adaptor (No.3, see sub-figure (a)), a pair of grips (No.4, see sub-figure (c)) and a specimen (No.15, see sub-figure (c)). They were carefully clamped in good alignment to avoid bending moments on the specimen.

In the dynamic system, the input testing speed was defined in the control system (No.1), and the load was applied through the actuator (No.2) driven by hydraulic pressure. To achieve high range of strain rates, the servo-hydraulic machine was in open loop mode which did not have instant feedback for accurate speed control. Nevertheless, the machine could maintain nearly constant speed over a certain distance in open loop. Therefore, the initial position of the actuator was adjusted, such that the dynamic testing was performed within the constant speed window. In addition, because that constant speed wasn't exactly equal to the input speed, the input speed was calibrated through trial and error for each testing condition. The deviation in the real testing speed and the required speed has been controlled within $\pm 5\%$ error.

The slack adaptor (No.3) is normally a critical device for high rate testing in open loop system [130]. It consists of a hollow tube connected to the actuator (No.2) and a sliding bar connected to the top grip (No.4). In the testing, the hollow tube travels freely to accelerate before its end contracts the top of the sliding bar, thus a specific testing speed could be reached before loading the sample. A rubber washer, placed at the end of the hollow tube, was used to dampen oscillations from the impact [133].

The specimen (No.15) was mounted by a pair of lightweight grips (No.4) which was specially designed in order to reduce the inertia effects.

- Data acquisition

All signals of load and actuator displacement were fully integrated within the data acquisition system. Shown in Figure 4.10, three items for stress measurement were aligned in the load train: a strain gauge transducer (No.5, see sub-figure (c)), a piezoelectric load washer (No.6, see sub-figure (b)), and a machine-equipped strain gauge load cell (No.7, see sub-figure (b)). The signal from the strain gauge (No.5) was converted and amplified through a strain gauge transducer amplifier (No.8); the signal from the piezoelectric load washer (No.6) was amplified by another amplifier (No.9). See Figure 4.10 (a), both the signals from No.5&8 (Channel I) and No.6&9 (Channel II) were monitored by a digital work station (No.11); the signal from No.7 was monitored by the INSTRON control system (No.1). The position of the actuator (No.2) was tracked internally through a linear variable differential transformer (LVDT) in the INSTRON. This signal was also imported into the digital work station as Channel III and set up for trigger control. During testing, the digital work station was triggered by the actuator displacement, just prior to the contact of the hollow tube and the sliding bar, to realize synchronous recording of the three signal-channels.

To determine the load, conversion from the signals of voltage recorded by the digital work station to forces was required. Regarding Channel I, calibration was made for each specimen right before each testing. The procedure was: first, the strain gauge transducer amplifier (No.8) was connected to a multimeter (No.10). Second, the specimen was gently stretched within the elastic deformation range by controlling the actuator manually, while a range of force and voltage values were recorded. The value of force was read from INSTRON control system (No.1) measured by the strain gauge load cell (No.7), and the corresponding value of voltage was read from the multimeter. Last, the ratio between loading force and the output of strain gauge transduce amplifier was determined through linear regression of the recorded numbers. Regarding Channel II, the ratio between force and voltage was available from calibration results given by the device manufacturer. For tensile testing at strain rate 5/s, the stress was calculated from the measurement of piezoelectric load washer (Channel II). In this case, the strain gauge as well as relevant devices and procedure were not needed. For tensile testing at strain rates 50-500/s, stress was calculated from the measurement of the strain gauge transducer (Channel I). Nevertheless, the piezoelectric load washer was retained for the consistency of set-up.

The signal of actuator displacement in the digital work station (Channel III) was also calibrated. For a certain position of the actuator, the corresponding values of displacement and voltage were read from the INSTRON control system and the digital work station, respectively. Based on a range of reading numbers, the ratio was determined through linear regression. The converted data of actuator displacement was used to check real testing speeds.

- DIC system

DIC system was employed for strain measurement. Shown in Figures 4.10, it consisted of a high speed camera (No.12), a lighting system (No.13) and a control system (No.14). The high speed camera was used to track specimen deformation. The frame rate and resolution of the camera

were adjusted according to test conditions. Limited by the device capacity, for high rate testing, the frame rate could be increased only by reducing resolution. For example, testing on martensite specimen at 500/s strain rate lasted less than 0.3ms, so the frame rate was set as 108,000 fps to obtain about 30 frames of images during specimen deformation, while the corresponding resolution was just 768×64 pixels. The trade-off between sampling rate and image accuracy had to be carefully weighed. To minimise heating of the sample, the lighting system was switched on just prior to testing. The control system was used to run the camera and record images. Images were imported into ARAMIS for DIC post-processing. The way to calculate the strain was same as that for quasi-static testing described in sub-section 4.4.1.3.

4.4.2 The second group: tensile testing over a series of phase compositions

Boron steels with a series of phase compositions (martensite volume fraction from 0 to 100%) were tested under a quasi-static condition (strain rate 0.001/s). Heat treatments were performed to produce specimens having various microstructures; microstructure analysis was conducted to quantify the phase composition of specimens.

4.4.2.1 Specimen design and preparation

Figure 4.11 shows the geometry of the dog-bone type tensile specimen in solid line. It was designed to be consistent with the specimens in the previous group: 3mm gauge width and 18mm parallel length (15mm gauge length). Since no strain gauge was required, the two gripping sections were of the same length.

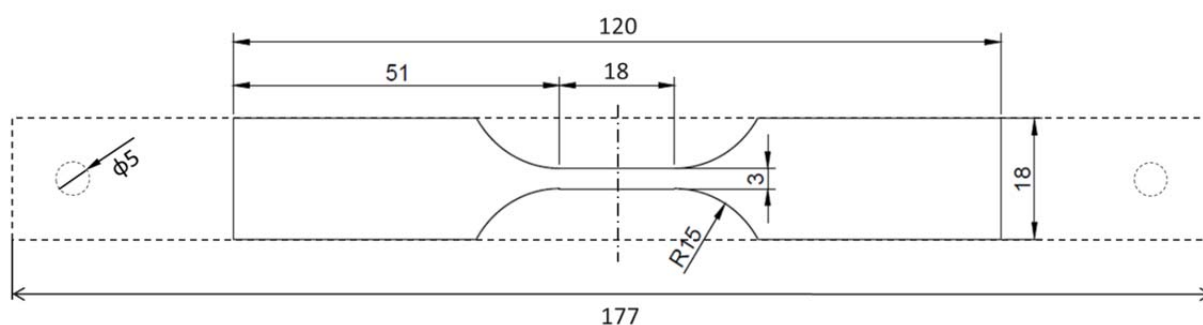


Figure 4.11 Design of specimens (dimensions are in mm) for quasi-static tensile testing (solid line) and Gleeble heat treatments (dash line)

A Gleeble 3800 material simulator was employed for steel heat treatment due to its accurate process control. However, the temperature gradient due to resistance heating was not desirable because the microstructure distribution in the gauge section of tensile specimens had to be uniform. When a dog-bone type specimen was heated in the Gleeble, there were large temperature gradients along the gauge length, especially at the locations close to shoulders. Therefore, a design of rectangular specimen with large length (dashed line in Figure 4.11) was adopted. In addition, stainless steel (instead of copper) grips with smaller thermal conductivity were employed. In this case, the temperature variations in the region 9mm from mid-length, which corresponded to the parallel length of the tensile specimen, were controlled within 5K.

The as-delivered boron steel specimens were heated to different temperatures (993K–1173K) at the heating rate of 15K/s and soaked for 5 minutes, in order to achieve different extents of austenitization. The cooling rate of 50K/s was defined to enable complete transformation from austenite to martensite. Thus, quenched boron steel specimens having different fractions of martensite were obtained.

A series of soaking temperatures (993K, 1023K, 1053K, 1083K, 1113K, 1143K, and 1173K) with the even increment were firstly selected for heat treatments. Based on the preliminary results

of tensile testing, a critical temperature range was identified. Then, more soaking temperatures (1063K, 1068K, 1073K, 1078K, 1093K, and 1103K) were sampled for further investigation.

Heat treated specimens were machined to obtain tensile specimens. Two small pieces cut from the middle section of each specimen were kept. Figure 4.12 shows the test-pieces of different parts used for different testing. The specimen preparations for tensile testing were conducted according to the step 2 and step 4 introduced in subsection 4.4.1.2.

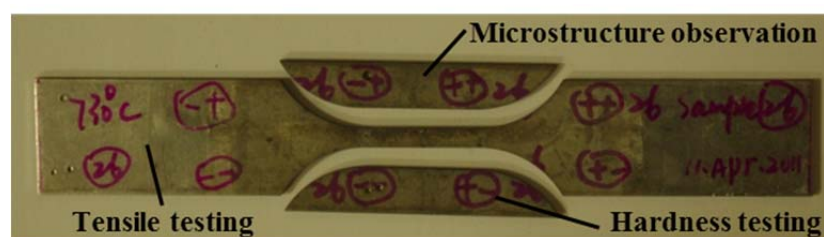


Figure 4.12 Test-pieces for different testing

4.4.2.2 Test procedure

Quasi-static tensile testing of specimens having different phase compositions (corresponding to the 13 soaking temperatures) was conducted at a strain rate of 0.001/s. The test equipment and procedure was same as that described in sub-section 4.4.1.3.

According to tensile results, representative specimens corresponding to soaking temperatures of 993K, 1023K, 1063K, 1068K, 1073K, 1083K, 1113K, 1143K, and 1173K were selected to measure hardness and phase composition. At least five indents were made on each specimen for measuring the hardness. Microscopic images, obtained from SEM observation, were processed using a commercial software Image-J for measuring the volume fraction of martensite.

CHAPTER 5 EXPERIMENTAL RESULTS AND DISCUSSION

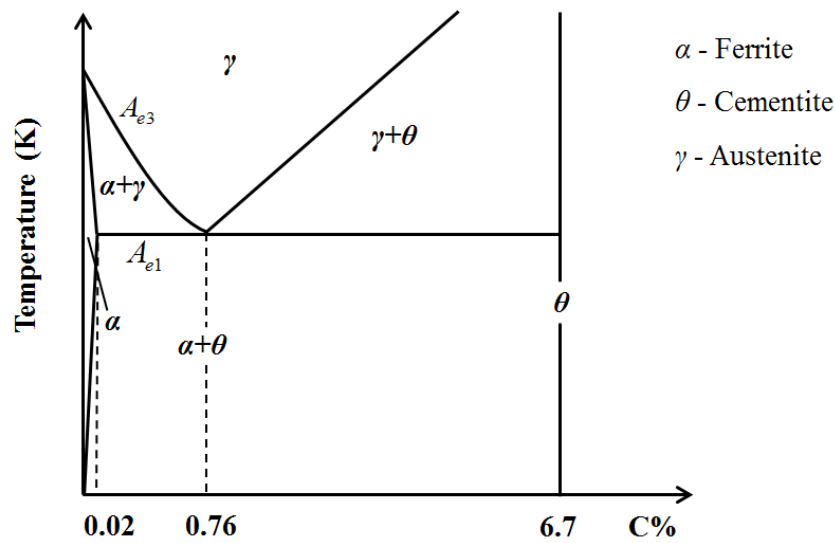
5.1 Introduction

This chapter contains detailed results obtained from the three sets of experiments described in the previous chapter. Moreover, discussion and analysis are conducted to characterise the material behaviour under hot stamping conditions and in automotive crash scenarios. First, based on the results of heat treatment tests, the effects of heating rate and temperature on the austenite formation are rationalised. Second, based on the results of hot tensile tests, the viscoplastic deformation behaviour of boron steels (austenite and initial phase) is discussed in terms of strain rate and temperature dependence. Last, based on the results of tensile tests at room temperature, the strain rate sensitivity of as-formed boron steels (martensite and initial phase) is analysed; combined with the hardness and microstructure measurements, the influence of phase composition on tensile properties is characterised.

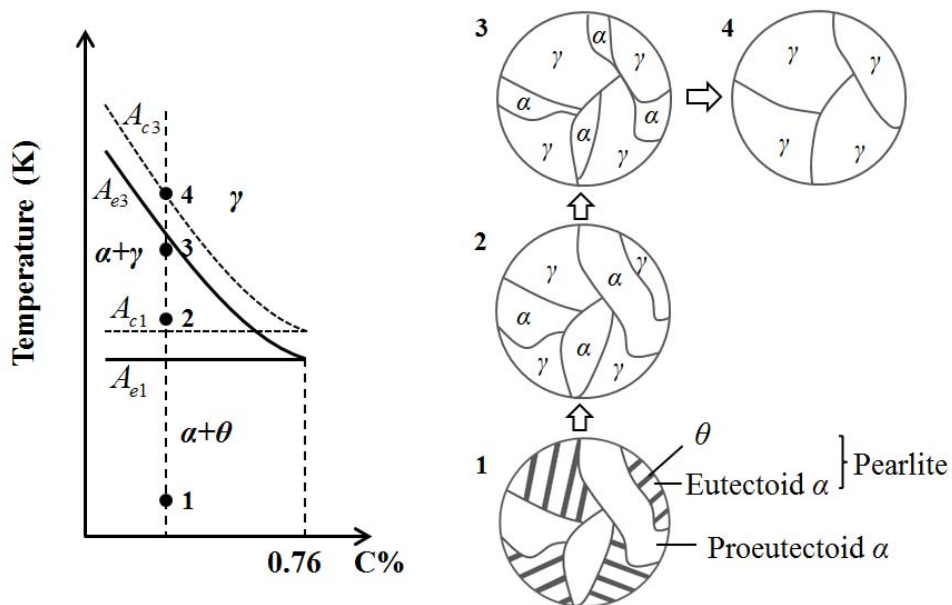
5.2 Austenite formation

The mechanism of austenite formation in hypoeutectoid steels is introduced first for better interpretation of the experimental characterisation. The evolution curves of austenite volume fraction with temperature and time are obtained from dilatometric curves. By analysing the evolution curves, the effects of heating rate and temperature on the progress of austenite formation under both non-isothermal and isothermal conditions are investigated.

5.2.1 Mechanisms of austenite formation in hypoeutectoid steels



(a) Fe-C equilibrium phase diagram



(b) The phase transformation process

Figure 5.1 The formation of austenite in a hypoeutectoid steel (containing less than 0.76 wt% C)

(a) Fe-C equilibrium phase diagram (b) Phase diagram of hypoeutectoid steel and the schematic representations of the microstructure evolution

A study of the constitution and structure of steels normally starts with the Fe–C equilibrium diagram [134]. Figure 5.1 (a) shows the equilibrium condition for thermodynamically distinct phases. According to the carbon content of the studied steel, only the hypoeutectoid part of the equilibrium diagram, where $0.02 < \text{wt\% C} < 0.76$, is studied in this paper. Regarding this part, there are two features which are critical: first, the temperature A_{e1} at which the eutectoid reaction occurs; second, the temperature A_{e3} at which the ferrite (α) can fully transform to austenite (γ). The A_{e1} is normally a single temperature above 973K and does not change with carbon content, whereas the A_{e3} is about 1183K for pure iron and progressively decreases with increase in carbon. This is because the solubility of carbon in ferrite (α) is low and ferrite alone can begin to transform to austenite (γ) only at high temperature, but if cementite decomposes and yields its carbon to the transformation front, the reaction from ferrite to austenite can proceed at lower temperatures [106, 134].

However, preheating steel is a continuous operation for most practical hot forming applications [107]. The formation of austenite in a hypoeutectoid steel generally involves heating an aggregate of ferrite and cementite ($\alpha + \theta$) through two phase ($\alpha + \gamma$) region into a single austenite (γ) phase. In this condition, the equilibrium diagram is not valid and beginning and end of the transformation are shifted to higher temperatures A_{c1} and A_{c3} which are sensitive to the heating rate [106, 134]. Therefore, as shown in Figure 5.1(b), the phase diagram is modified for transformations that occur in continuously increasing temperature conditions [135]. The formation of austenite in a hypoeutectoid steel during continuous heating is schematically illustrated. In Figure 5.1 (b-1), the initial microstructure of the steel is composed of pro-eutectoid ferrite (α) and pearlite, the latter being a composite of eutectoid ferrite (α) and cementite (θ). The phase composition of the mixture is determined by the amount of carbon in the steel. With an increase in atom mobility and driving force during heating, the pearlite regions firstly become unstable above temperature A_{c1} . In a real microstructure, a pearlite region contains numbers of

colonies in which lamellas of ferrite and cementite, variously spaced and oriented, are located. Austenite nucleation primarily takes place at intersections or interfaces of pearlite colonies, and also at interfaces of ferrite-cementite lamellae within a colony [105]. The new grains of austenite grow into pearlite colonies to replace the eutectoid ferrite; at the same time, cementite dissolves in the austenite. Once the pearlite is consumed (Figure 5.1 (b-2)), the reaction proceeds into the remaining pro-eutectoid ferrite. Below temperature A_{c3} , the ferrite can transform to austenite only with additional carbon provided. Carbon atoms diffuse from inside the enriched austenite grains to γ/α interfaces and cross them, which enables the transformation from pro-eutectoid ferrite to austenite. The γ/α interfaces gradually move towards α phase regions (Figure 5.1 (b-3)). This process continues until temperature A_{c3} is reached, when the average carbon content in austenite becomes equal to the carbon content of the steel. The steel is then fully austenitic (Figure 5.1 (b-4)).

5.2.2 Experimental results

When a metal undergoes a phase transformation, the lattice structure changes, which is in principle accompanied by a change in specific volume. The formation of austenite involves the lattice change of iron from a body-centred cubic (BCC) form to a face-centred cubic (FCC) form, which results in a change in density and hence in volume. The evolution of austenitization can thus be deduced from experimental results of dilatometry [97, 134, 136].

Figure 5.2 (a) and (b) show the experimentally measured width change (ΔW) versus temperature and time, respectively. The test was carried out at a heating rate of 5K/s with soaking temperature of 1173K for 15 minutes. The experimental curve can be divided into four stages. As can be seen in Figure 5.2 (a), in the first stage, the dilatometric curve exhibits a linear expansion as the temperature changes. This is a pure thermal expansion of the boron steel with the initial phase mixture. In the second stage, the dilatometric curve deviates from linearity from 1007K (A_{c1}).

This is because the formation of austenite takes place, which contributes to the change of specimen width. For the continuous heating stage, the curve is a result of the competition between the volumetric change induced by phase transformation and thermal expansion. For the isothermal soaking stage, the curve shows only contraction caused by the phase transformation (the vertical part in Stage 2 shown in Figure 5.2 (a)). As shown more clearly in Figure 5.2 (b), the austenite formation rate in the isothermal soaking period decreases with the soaking time. At 15 minutes of the soaking time (Figure 5.2 (b)), the width change rate tends to zero, i.e. $d(\Delta W)/dt \approx 0$. It can be concluded that thermodynamic equilibrium has been achieved. The microstructure ends up as full austenite γ for this case, since the soaking temperature is above A_{e3} . It could be a mixture of austenite and ferrite ($\gamma + \alpha$) if the soaking temperature is between A_{e1} and A_{e3} [99, 102]. In the third stage, the curve is linear again, which reflects the pure thermal contraction of the steel during quenching or rapid cooling. In the fourth stage, volume expansion is shown on the curve, which corresponds to the phase transformation from austenite γ to martensite α' . Since this study is mainly concentrated on the formation of austenite, the analysis is focused on the experimental data in Stage 2 of Figure 5.2. The experimental results, corresponding to the section from 873K to the end of soaking, under different testing conditions are summarised in Figure 5.3.

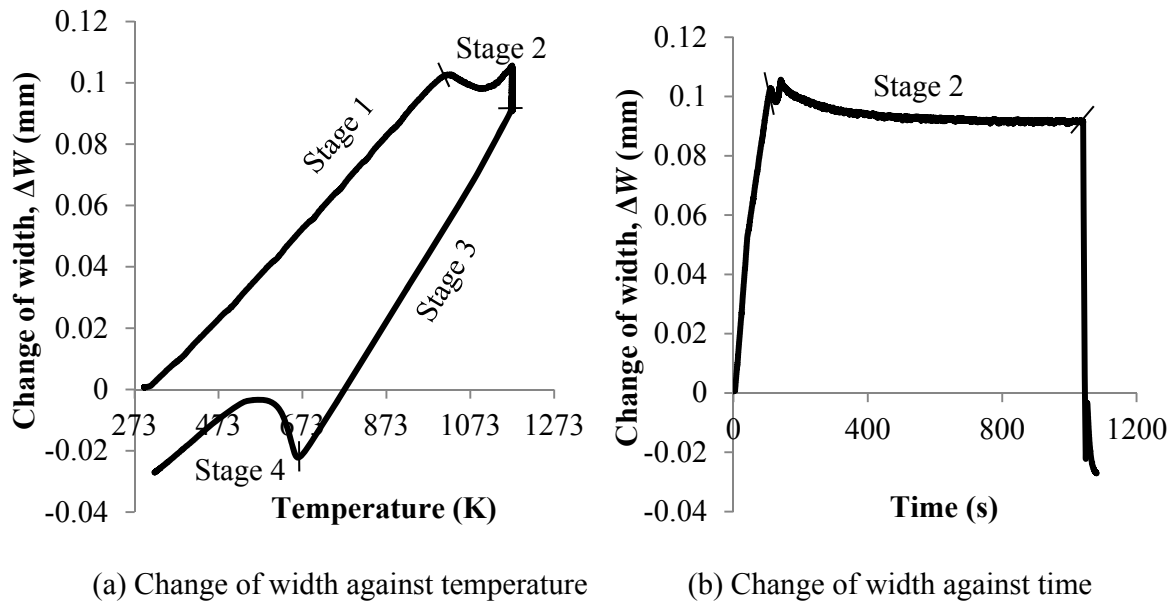
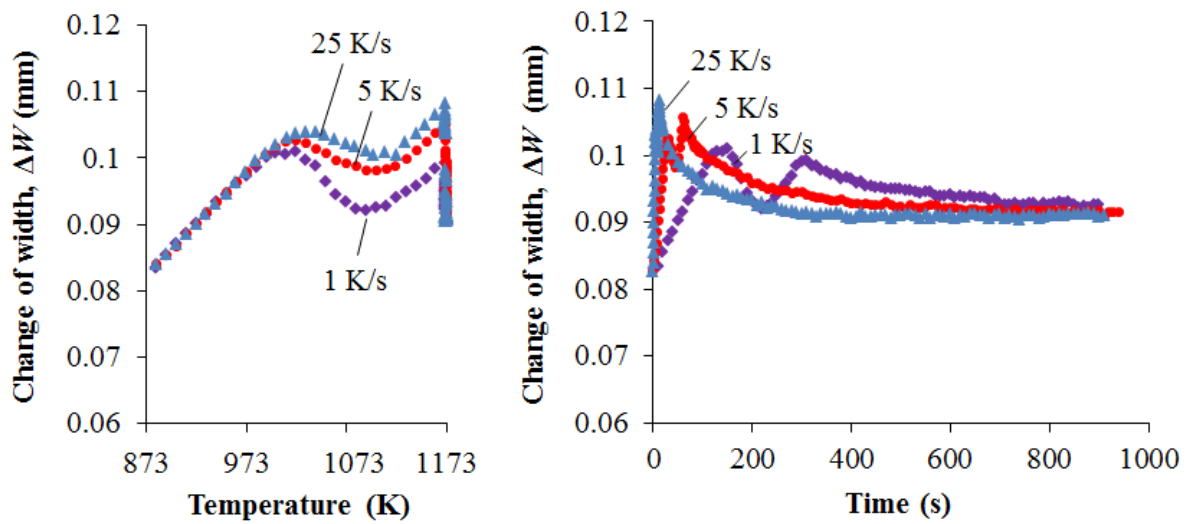


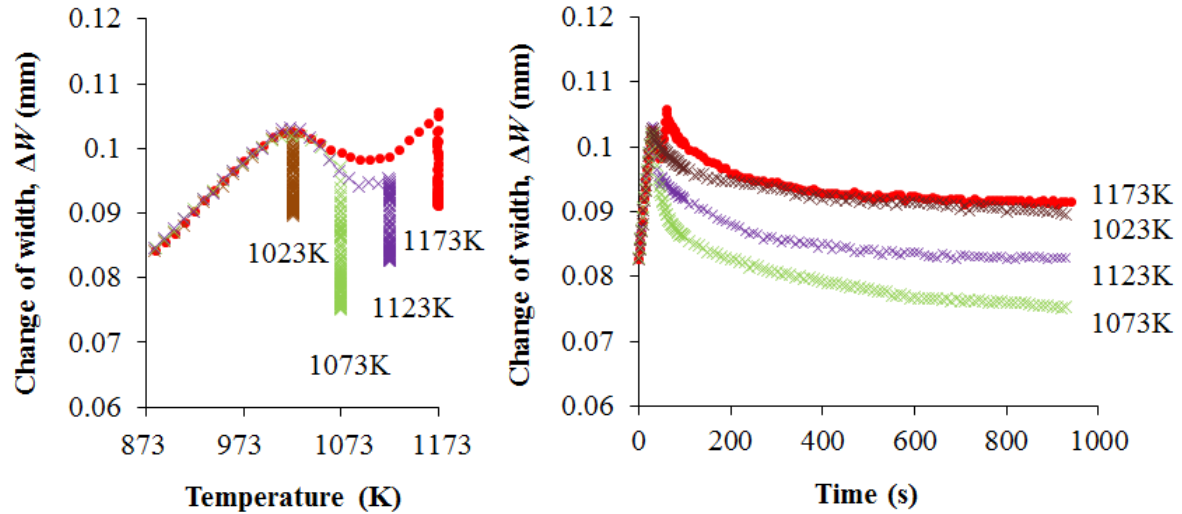
Figure 5.2 Experimental curves showing the width change of specimen against (a) temperature and (b) time during the heat treatment process (heating rate: 5K/s, soaking temperature: 1173K)

Figure 5.3 (a) shows the width changes of specimens (ΔW) with temperature and time, respectively, for different heating rates and constant soaking temperature of 1173K. During the continuous heating period (the left figure) a lower starting temperature (A_{c1}) and more contraction of width due to austenitization are observed for the lower heating rate. During the isothermal soaking period (the right figure) the width change (ΔW) for all heating rates reduces gradually and becomes constant at a common value. This indicates that, given sufficient soaking time, the austenite formation could be completed at a temperature of 1173K. Note, this is higher than A_{e3} . Thus, the austenite formation has been completed for all the three tests. Figure 5.3 (b) again shows ΔW of specimens with temperature and time. However these tests were carried out at a heating rate of 5K/s and held at four different soaking temperatures of 1023K, 1073K, 1123K and 1173K for 15 minutes. During the continuous heating period (the left figure) ΔW for all tests lies almost on the same curve, as the heating rate was common. During the isothermal soaking period (the right figure) all the curves tend to become horizontal eventually, which shows thermodynamic equilibrium has been virtually reached for every isothermal soaking condition. A

different reduction of ΔW can be seen for each of the soaking temperatures; however, the value of the width change (ΔW), is a function not only phase composition but also instantaneous temperature and therefore is not an indicator of the degree of phase transformation alone.



(a) Soaking temperature: 1173K

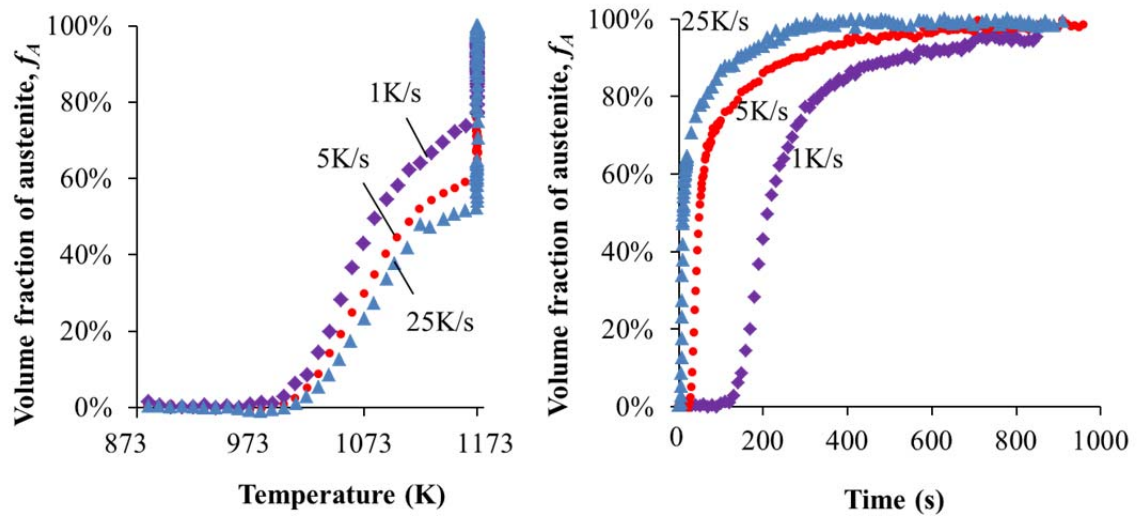


(b) Heating rate: 5K/s

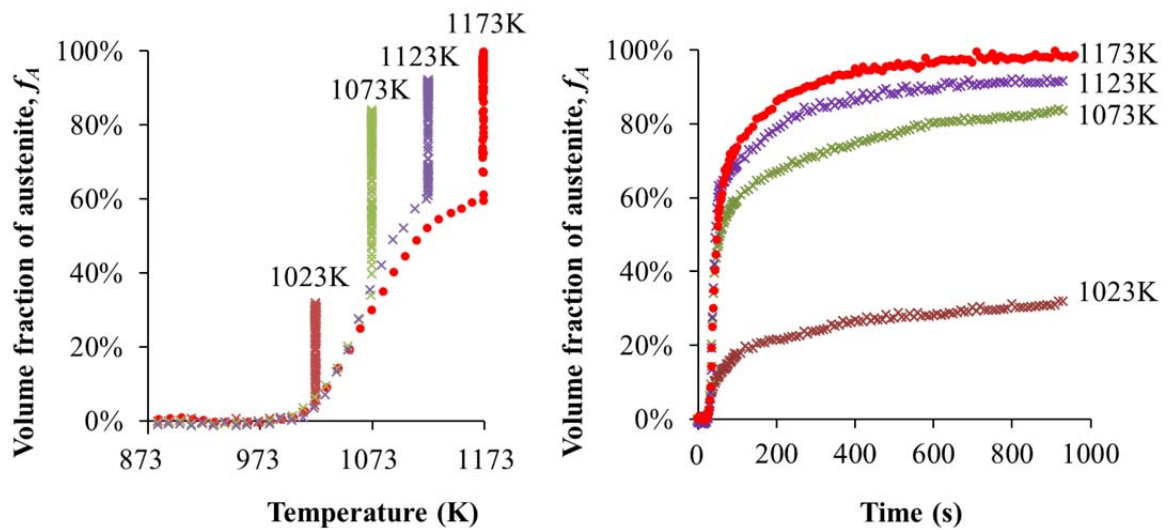
Figure 5.3 Width changes of specimens tested at different (a) heating rates (soaking temperature: 1173K), and (b) soaking temperatures (heating rate: 5K/s)

A transformation method has been developed to calculate austenite volume fraction based on the experimentally measured ΔW in this study. Details are provided in Appendix 1. By using the method, the dilatometric curves shown in Figure 5.3 can be presented in terms of austenite volume fraction, as shown in Figure 5.4, which permits a more rational insight into the progress of austenite formation.

Figure 5.4 (a) shows the first group of test results. The austenite formation firstly progresses differently during continuous heating for different heating rates. When the continuous heating ends at 1173 K, the amount of transformed austenite depends on heating rate: for 1K/s, $f_A = 77\%$; for 5K/s, $f_A = 61\%$; and for 25K/s, $f_A = 54\%$. Subsequently, the volume fractions of austenite (f_A) keep increasing until about 100% at different rates under isothermal conditions, despite soaking temperature being the same. Figure 5.4 (b) shows results of the second group of tests. With increasing soaking time, the volume fraction of austenite (f_A) increases and then becomes almost constant at a value less than 100%, which depends on soaking temperature. The maximum value of volume fraction obtained for each soaking temperature is: for 1023K, $f_A = 32\%$; for 1073K, $f_A = 63\%$; for 1123K, $f_A = 92\%$; and for 1173K, $f_A = 99\%$.



(a) Soaking temperature: 1173K



(b) Heating rate: 5K/s

Figure 5.4 Variations of volume fraction of austenite with temperature and time for different (a) heating rates (soaking temperature: 1173K) and (b) soaking temperatures (heating rate: 5K/s)

5.2.3 Analysis of full austenite formation

Phase transformation in general is controlled by two types of factors: 1) Initial microstructure, including phase composition, chemical composition, grain size and the presence of non-metallic inclusions; that is, the intrinsic properties of an alloy. 2) External conditions, including heating

rate and temperature. Assuming that the intrinsic properties of the tested boron steel were to the supplier's specification and the same for all specimens, this study is focused on the effects of process conditions: heating rate and soaking temperature on the progress of austenite formation.

5.2.3.1 Effects of heating rate on non-isothermal austenite formation

It is stated in Section 2 that certain amounts of superheat above equilibrium temperatures A_{e1} and A_{e3} are required to start and complete the phase transformation under non-isothermal conditions [42, 94]. The temperature and time to start austenite formation and to attain certain volume fraction of austenite ($f_A = 10\%$ to 50%) in the heating-up stage, as measured for different heating rates, are summarised in Figure 5.5, which is normally called a continuous heating transformation (CHT) diagram. It is apparent that less time is required at a higher heating rate, to achieve the same volume fraction of austenite. Figure 5.5 also shows that the starting temperature A_{c1} increases with increasing heating rate. For example, at the heating rate of 1K/s , the temperature for A_{c1} is 996K , but for the heating rate of 25K/s it is 1010K . The same phenomenon can be observed for the other volume fractions ($f_A = 10\%$ to 50%), shown in Figure 5.5. This is mainly due to the fact that a higher heating rate results in less soaking time being required for incubation of austenite formation.

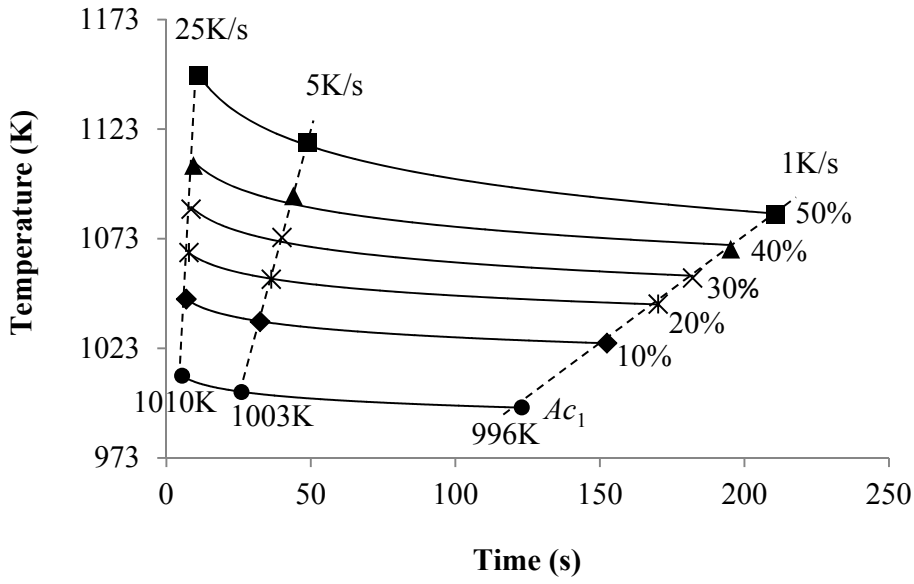
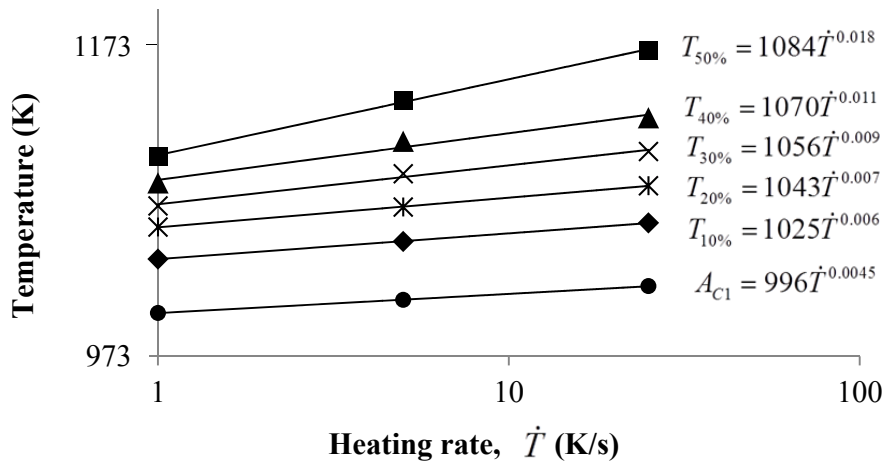
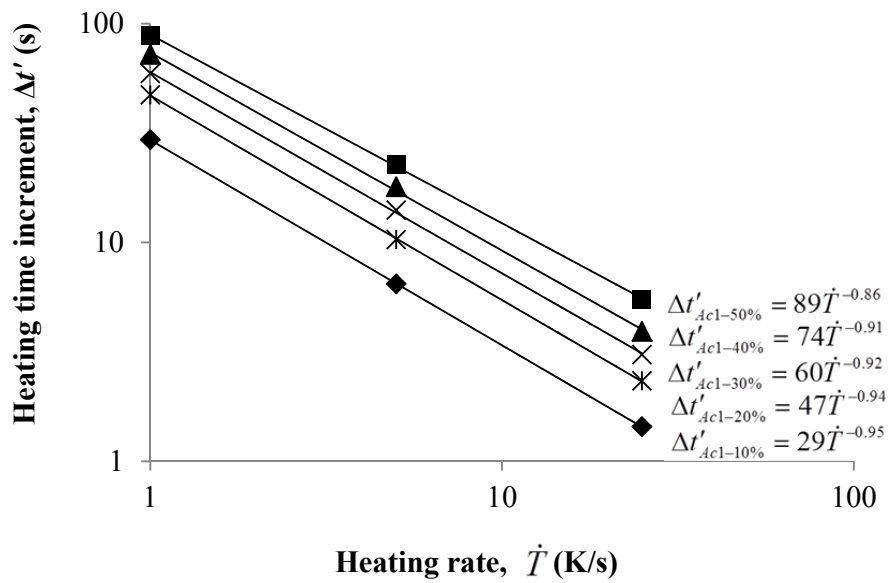


Figure 5.5 Continuous heating transformation (CHT) diagram

Figure 5.6 (a) shows that the relationship of heating rate and temperature for a certain volume fraction of austenite formation ($f_A = 0\%$ to 50%) is linear when plotted on log-log axes. In the equations given for the trend lines, \dot{T} is heating rate in K/s, and T is the absolute temperature in K. For example, for 50% austenite formation, the 3 data points of temperature and heating rate can be approximated by $T_{50\%} = 1084 \dot{T}^{0.018}$ (the top line in Figure 5.6 (a)). The slope of the trend lines for different volume fractions are positive and increase with increment of austenite volume fraction. For example, for $f_A = 10\%$, the slope is 0.006, and for $f_A = 50\%$, the slope is 0.018. These features reveal that the temperature required to attain a certain amount of austenite increases with increasing heating rate. In addition, the effect is greater for greater amounts of transformation.



(a) Effects of heating rate on the transformation temperature to attain certain volume fractions of austenite



(b) Effects of heating rate on the transformation time to attain certain volume fractions of austenite

Figure 5.6 Effects of heating rate on austenite formation under continuous heating conditions

Figure 5.6 (b) shows the relationship between heating rate and required time for various volume fractions of austenite formation are again linear when plotted on log-log scales. On the vertical axis and in the trend line equations, $\Delta t'$ is heating time increment and represents the time

difference from the time starting of austenite formation to the time reaching a given volume of austenite fraction ($f_A = 10\%$ to 50%). For example, $\Delta t'_{Ac1-50\%}$ represents the time increment from the time at temperature A_{c1} to the time when f_A reaches 50% . The slopes of trend lines are negative, which reveals that the transformation time for a certain volume fraction of austenite decreases with increasing heating rate. The absolute value of a slope decreases with the increment of austenite volume fraction, which indicates that the effect on transformation time is weakened as the transformation proceeds.

The linear features shown in Figure 5.6 (a) and (b) provide useful information for modeling austenite formation. Nucleation and growth are the two main mechanisms operating in the phase transformation process. Their rates can be modelled using the equations of [42, 101, 105, 115, 119, 137]:

$$\dot{N} = N_0 \exp\left(-\frac{Q_N}{RT}\right) \quad (5.6)$$

$$\dot{G} = G_0 \exp\left(-\frac{Q_G}{RT}\right) \quad (5.7)$$

where R is the gas constant, T is the absolute temperature; Q_N and Q_G are activation energy of nucleation and growth, respectively; N_0 and G_0 are pre-exponential factors which can be functions representing the effects of influencing factors on nucleation and growth. With respect to the formula of N_0 and G_0 , in addition to the material related parameters, heating rate as a critical thermodynamic factor should also be taken into account in non-isothermal austenite formation. According to the results obtained in this work, it is suggested that it should be integrated in terms of a power law.

5.2.3.2 Effects of heating rate on isothermal austenite formation

Figure 5.7 shows the required time to increase austenite volume fraction by 5% from different stages ($f_A = 80\%$, 85% , and 90%) of the isothermal transformation for different heating rates. The isothermal transformation takes place at a constant soaking temperature of 1173K , at which full austenite formation is achievable. In the Figure, Δt , which is termed as soaking time increment, represents the time difference from the time corresponding to a certain austenite volume fraction (f_A) to the time reaching another higher value of f_A during soaking. For example, $\Delta t_{80\%-85\%}$ represents the time increment from the time when f_A is 80% to the time when f_A reaches 85% . It can be seen, again, that the relationship of heating rate and soaking time increment is linear, when plotted on log-log scales. Similar to Figure 5.6 (b), the slopes of trend lines are negative. This reveals that, for the same stage of transformation, under the same isothermal condition, less time is required for a higher heating rate. This leads to an important conclusion that the thermodynamic effect of heating rate proceeds from the heating-up step and continues through the subsequent isothermal soaking step. This is because the transformation rate at any time depends on both the instant growth rate of new phase grains and the existing quantity of the grains (not only on instantaneous nucleation rate) [119]. During continuous heating, a higher heating rate stimulates a higher nucleation rate, which allows more nuclei used for austenite formation to be generated even within a shorter period [109]. Therefore, during subsequent isothermal soaking at a given temperature, a larger amount of pre-existing grains enables higher overall growth rate of new phase, that is, a higher austenite formation rate. It can be observed that all the trend lines in Figure 5.7 are nearly parallel. This interesting feature indicates that the influence of heating rate on the isothermal transformation remains constant throughout different austenite formation stages. Moreover, another feature shown in Figure 5.7 is that longer time is required to increase austenite volume fraction by 5% at a later stage of transformation, which reveals the impingement mechanism in the steel [119].

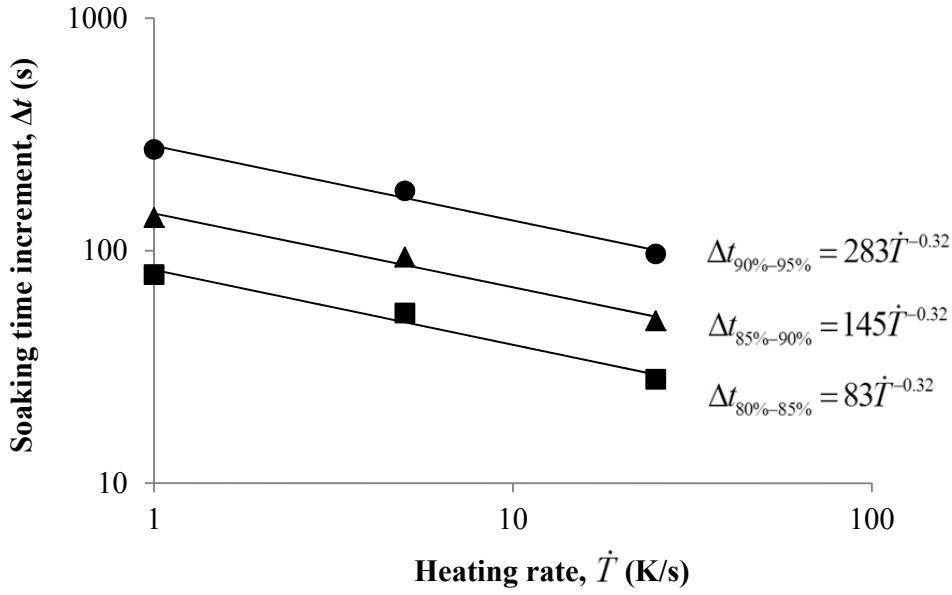
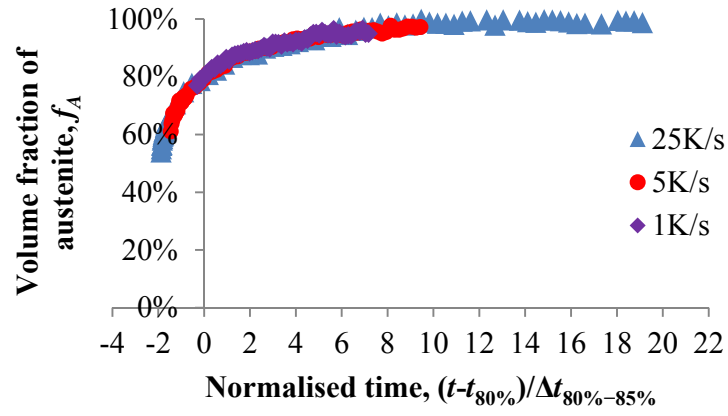


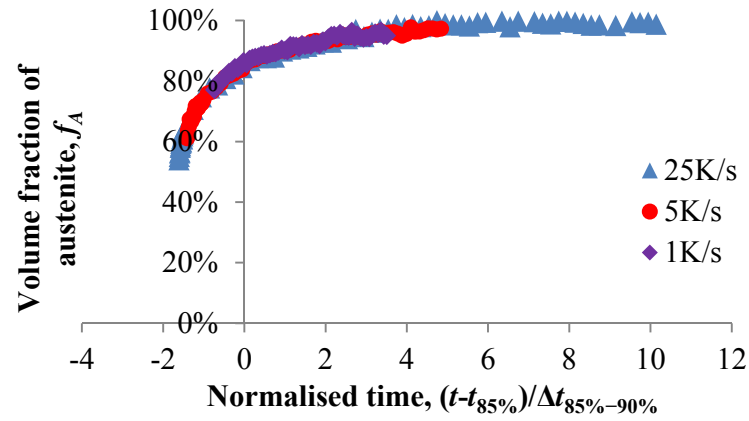
Figure 5.7 Effects of heating rate on the transformation time to increase austenite volume fraction by 5% from 80%, 85% and 90% during soaking at 1173K

The evolution curves of austenite volume fraction, corresponding to a period of 10 minutes starting from isothermal soaking, for each of the three testing conditions, are plotted on the base of normalised time in Figure 5.8. Regarding Figure 5.8 (a), for each heating rate, the time for $f_A = 80\%$ is taken as the origin of the horizontal axis, the soaking time increment $\Delta t_{80\%-85\%}$ is taken as a unit for time normalization. The normalised time is given by $(t - t_{80\%}) / \Delta t_{80\%-85\%}$, where t is the instant time at a time scale starting from the time at temperature of 873K, $t_{80\%}$ is the time for $f_A = 80\%$ for the same time scale, $\Delta t_{80\%-85\%}$ is the transformation time to increase austenite volume fraction by 5% from 80%. The condition for this normalization is the influence of temperature and heating rate being constant throughout the interested progress. With time normalization, the feature of an evolution curve should be determined only by metallurgical properties which control the transformation kinetics. Its dependency on temperature and heating rate has been eliminated automatically. As shown in Figure 5.8 (a), the evolution of austenite volume fraction, with normalised time with the starting point of $f_A = 80\%$, for all heating rates lies on a same curve

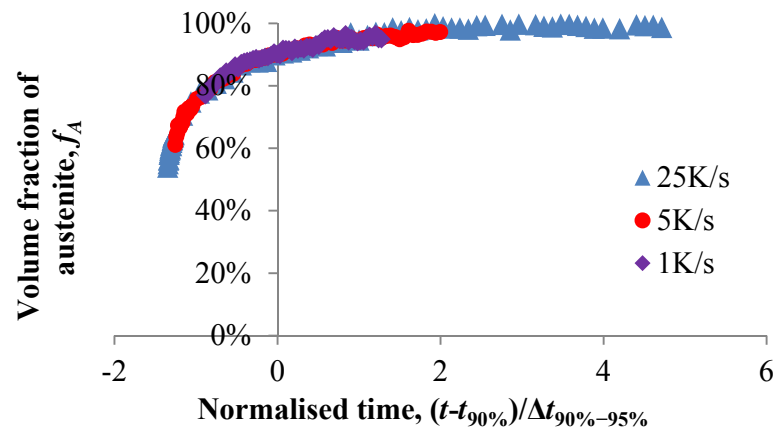
and slows towards a volume fraction of 100%. This indicates that the impingement mechanism under the isothermal transformation stage does not depend on heating-up conditions in the considered range. Moreover, the figure shows a comparison of austenite formation progress for different heating rates. For example, the curve for the highest heating rate, 25K/s, even starting with the lowest volume fraction of austenite, is the one that most approximates to equilibrium after the same transformation time. This once again shows that a higher heating rate enables a higher rate of subsequent isothermal transformation in the studied steel. In Figures 5.8 (b) and (c), the time for $f_A = 85\%$ and 90% is taken as the origin of the horizontal-axis respectively, and is normalised by soaking time increments $\Delta t_{85\%-90\%}$ and $\Delta t_{90\%-95\%}$, respectively, which is similar to the horizontal axis in Figure 5.8 (a). The same features shown in Figure 5.8 (a) can be found in figures 5.8 (b) and (c). The only difference of the three figures is the normalised time scale, since the value of Δt (normalised) becomes higher at the later stage of the transformation as shown in Figure 5.7. Figure 5.8 indicates that the effect of heating rate on austenite formation can be eliminated if the transformation time is normalised using the method introduced here.



(a) Normalised by $\Delta t_{80\%-85\%}$



(b) Normalised by $\Delta t_{85\%-90\%}$



(c) Normalised by $\Delta t_{90\%-95\%}$

Figure 5.8 Volume fractions of austenite for different heating rates with time normalised by the soaking time increments for different austenite volume fractions, during soaking at 1173K

5.2.4 Analysis of intercritical annealing

In the second group of tests, the specimens were heated at the same rate of 5K/s to different temperatures (1023K, 1073K, 1123K and 1173K), and then kept at these individual temperatures for a sufficient period (15 minutes in this work) to enable an equilibrium condition of austenite formation to be achieved at each temperature. This provides insight into the kinetics of austenite formation during isothermal soaking at intercritical temperatures.

5.2.4.1 Saturated volume fraction

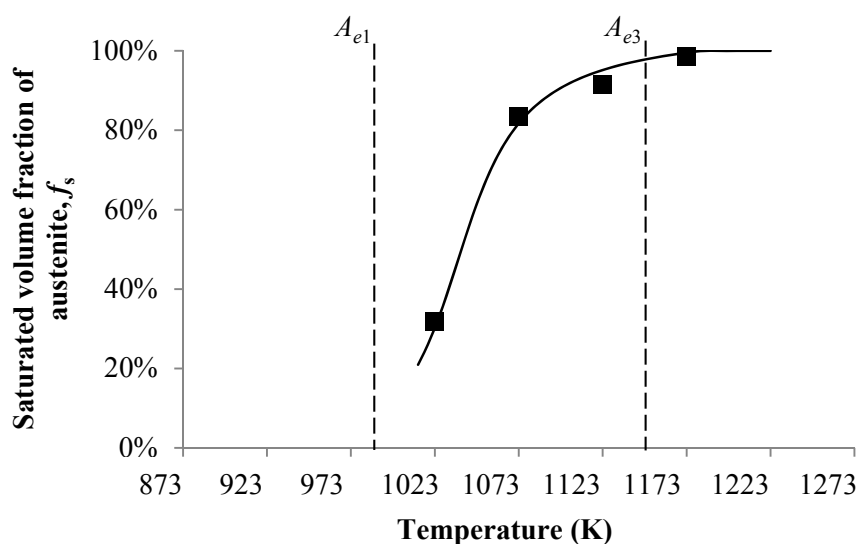


Figure 5.9 Saturated volume fractions of austenite at different soaking temperatures

If the steel is soaked at an intercritical temperature between A_{e1} and A_{e3} , shown in Figure 5.1, the volume fraction of transformed austenite can never reach 100% [99, 104]. In this work, the value of austenite volume fraction that can ultimately be achieved at any given soaking temperature, T , is known as saturated volume fraction f_{As} [99, 104]. Referencing the austenite formation and saturation features shown in Figure 5.4 (b), the saturated austenite volume fraction f_{As} for different soaking temperatures (between A_{e1} and A_{e3} , or above A_{e3}) can be obtained and are shown in Figure 5.9. The experimental results show a typical S-type of relationship on f_{As} - T axes. The

reference A_{e1} and A_{e3} for the type of studied steel provided by alloy supplier are 993K and 1118K, respectively. However, these values have tolerances since the chemical composition and starting microstructure of the alloy may vary from batch to batch. The result obtained in this study is slightly different from the reference: when soaking temperature is 1123K, f_{As} is 92%, which is acceptable for the study. Therefore, in this study, A_{e3} is taken as a temperature between 1123K and 1173K.

According to the analysis in subsection 5.2.3, it is also known that, although heating rate affects the austenite formation rate, it does not affect the maximum obtainable value of austenite fraction at a given soaking temperature, i.e. f_{As} is a function of only temperature.

5.2.4.2 Effects of temperature on isothermal austenite formation

Figure 5.10 shows the transformation time to increase austenite volume fraction by 10% of f_{As} from 80% of f_{As} (i.e. $f_A = 80\%f_{As}$ – $90\%f_{As}$) for different soaking temperatures. Again, Δt is the soaking time increment, $\Delta t_{80\%f_{As}-90\%f_{As}}$ represents the time increment from the time when f_A is 80% of f_{As} to the time when f_A reaches 90% of f_{As} . It can be seen that less transformation time is required at a higher temperature; in addition, the relationship between logarithmic soaking time increment, $\ln(\Delta t)$, and inverse temperature, $1/T$, approximately follows a straight line, which can be given by:

$$\Delta t = C \exp\left(\frac{Q_c}{RT}\right) \quad (5.8)$$

where C is a material constant, Q_c activation energy, R the gas constant, and T absolute temperature. The regularity can be explained as follows: In the studied steel, it can be expected that the nucleation of austenite occurs only in pearlite colonies and all the nucleation sites are consumed quickly at the beginning of the transformation [42, 96, 109]. Thus, having the same heating rate, same amount of nuclei is supposed to be generated in the tests. Then, the

transformation rate is controlled by only the growth rate of the austenite phase. Thus, it is determined by only the soaking temperature under isothermal conditions. This is the reason that, considering transformation time and rate are in inverse proportion, the formula (5.8) is consistent with equation (5.7).

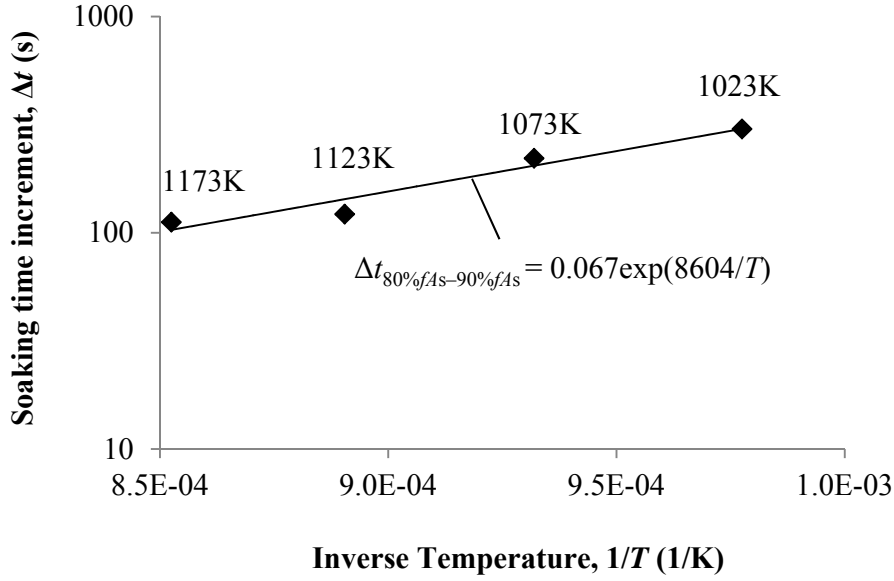
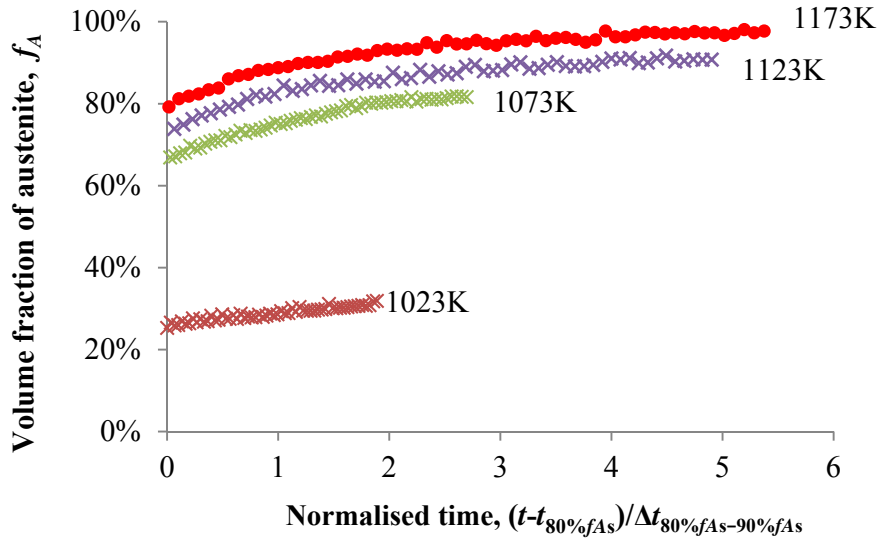


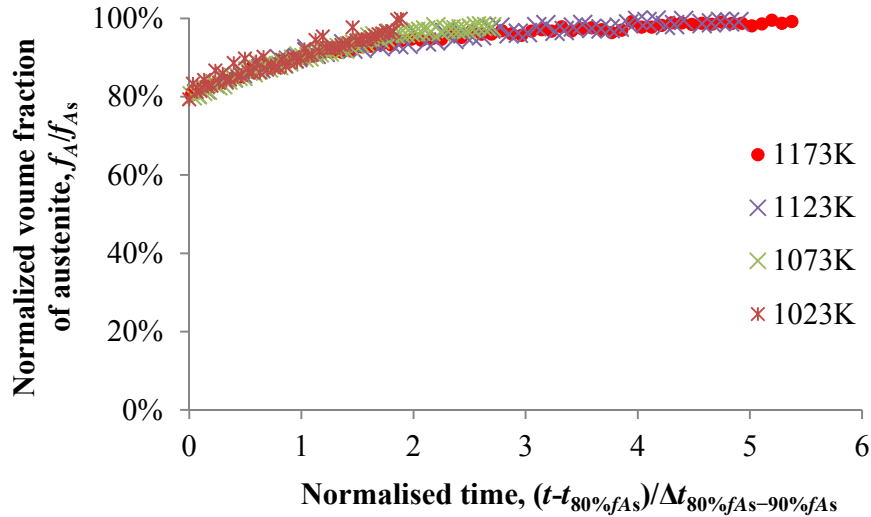
Figure 5.10 Effects of soaking temperature on the transformation time to increase austenite volume fraction by 10% of f_{As} from 80% of f_{As}

The evolution curves of austenite volume fraction, corresponding to a period of 10 minutes starting from 80% of f_{As} for each of the four soaking temperatures, are plotted on the base of normalised time in Figure 5.11 (a). For each test, the time for $f_A = 80\% f_{As}$ is taken as the origin of horizontal axis, the soaking time increment $80\% f_{As}(T) - 90\% f_{As}(T)$ is taken as a unit for time normalization. Thus the normalised time can be given as $(t - t_{80\% f_{As}}) / \Delta t_{80\% f_{As}-90\% f_{As}}$. In the figure, the different progressing rates of austenite formation within a same time period are illustrated. This again indicates that higher soaking temperature enables faster transformation progress towards equilibrium.

In Figure 5.11 (b), the same horizontal axis as Figure 5.11 (a) is employed. For the vertical axis the austenite volume fraction, shown in Figure 5.11 (a), is normalised by f_{As} of the corresponding soaking temperature. Similar to Figure 5.8, it is seen that the trends of curves are almost identical, which reveals that the isothermal austenite formation at different intercritical temperatures obeys the same kinetics of growth and impingement approaching equilibrium.



(a) Time is normalised by $\Delta t_{80\% f_{As}-90\% f_{As}}$



(b) Time is normalised by $\Delta t_{80\% f_{As}-90\% f_{As}}$ and volume fraction of austenite is normalised by f_{As}

Figure 5.11 Evolution curves of austenite volume fraction for different temperatures under isothermal transformation conditions

5.3 Thermo-mechanical properties of boron steels under hot stamping conditions

The flow stress-strain relationships of the austenite and initial phase of boron steel under hot stamping conditions are obtained from hot tensile test data. To improve accuracy of results, the test data corresponding to necking stage is corrected using a method described in Appendix 2; in addition, the real strain rate for each test is evaluated, as suggested in Chapter 4 (subsection 4.3.2.3). Based on the results, the effects of strain rate and temperature on the deformation behaviours of boron steel in the both phase states are characterised.

5.3.1 Results: flow stress-strain curves

5.3.1.1 Strain rate and temperature dependence of austenite

- Strain rate dependence

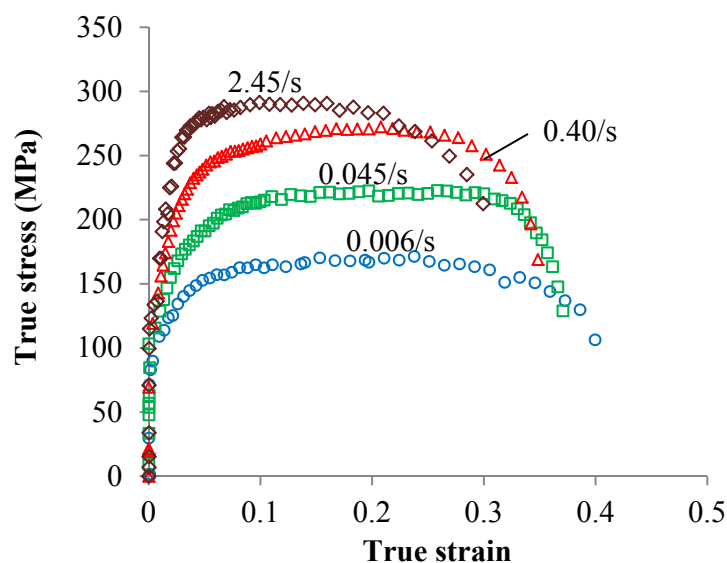


Figure 5.12 Experimental flow stress-strain relationships for austenite for different strain rates at a deformation temperature of 973K

The strain rate dependence of the tensile behaviour of boron steel in the austenitic state has been investigated for a deformation temperature of 973K. Figure 5.12 shows a set of true stress-strain

curves for different strain rates (the real values of true strain rates are 0.006/s, 0.045/s, 0.40/s, and 2.45/s). The peak flow stress is higher for a higher strain rate, which indicates the viscoplastic nature of material under the test conditions.

For viscoplastic solids at elevated temperatures, the pure elastic deformation is quite small and the initial yield stress is difficult to determine [138], thus analysis of this experimental data focuses on the plastic deformation. At the initial stage of plastic deformation, the steep increase of flow stress is mainly attributed to the viscous stress, which is strain rate dependent. Since initial yield strength is a function of temperature [138], the values of it should be the same for this group of flow curves due to the same deformation temperature. Thus, the fact that flow stress levels for different strain rates vary little at a small deformation (true strain $\varepsilon_T < 0.005$) may suggest that the strain rate sensitivity of viscous stress for the austenite of boron steel is relatively low. Subsequently, the gradual increase of flow stress with increasing strain is mainly related to work hardening, caused by dislocation accumulation and interactions [138]. Concurrently, the increasing trend is slowed down due to dynamic and static recovery processes, through annihilation of dislocations and relaxation of internal stresses [62]. Since static recovery is a function of time [62], for a lower strain rate, dislocation density is more reduced so that apparent hardening is not as great as that for higher strain rates, which is clearly manifested in the trend of flow curves in the figure. Significant variations in the hardening exponent for different strain rates can indicate that the static recovery for the material at the tested temperature is pronounced. The plateau of flow curves reveals the achievement of a steady state between strain hardening and recovery [57]. Larger extended ductility after the peak flow stress can be seen for a lower strain rate. Towards the end of deformation the softening mechanism of micro-damage dominates deformation [139], which is reflected by the dramatic drop of flow stress.

- Temperature dependence

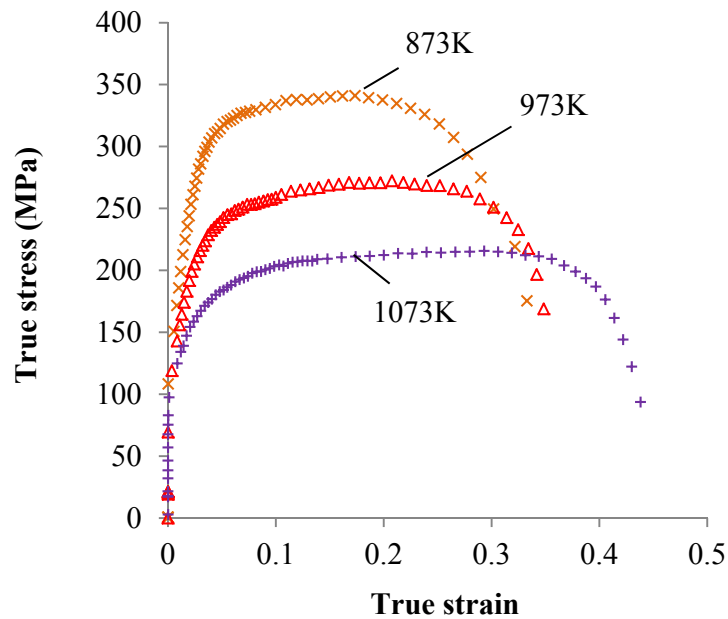


Figure 5.13 Experimental flow stress-strain relationships for austenite for different deformation temperatures (designed strain rate: 0.50/s)

The temperature dependence of the tensile behaviour of austenite has been investigated for a designed strain rate of 0.50/s, which is a typical rate that the material is subjected to in hot stamping practice. Figure 5.13 shows a set of true stress– strain curves for different deformation temperatures of 873K, 973K, and 1073K. The real strain rates for each test are: 873K-0.30/s, 973K-0.40/s, 1073K-0.50/s. The variations are negligible for the analysis here. Strong temperature sensitivity of the material is revealed by the curves: with increasing temperature resulting in significant reduction of initial strain hardening and peak flow stress, as well as increase of ductility. The result is typical of most metals, in which deformation associated processes are thermally activated. For a higher temperature, dislocation mobility is higher due to increased thermal vibration of the lattice and decreased strength of obstacles to dislocation movement, thus lower flow stress is required to facilitate further straining [140]. In addition,

grain-boundary sliding and rotation, as well as microstructural recovery are more activated with the increasing temperature [141], which enables larger ductility.

5.3.1.2 Strain rate and temperature dependence of initial phase

- Strain rate dependence

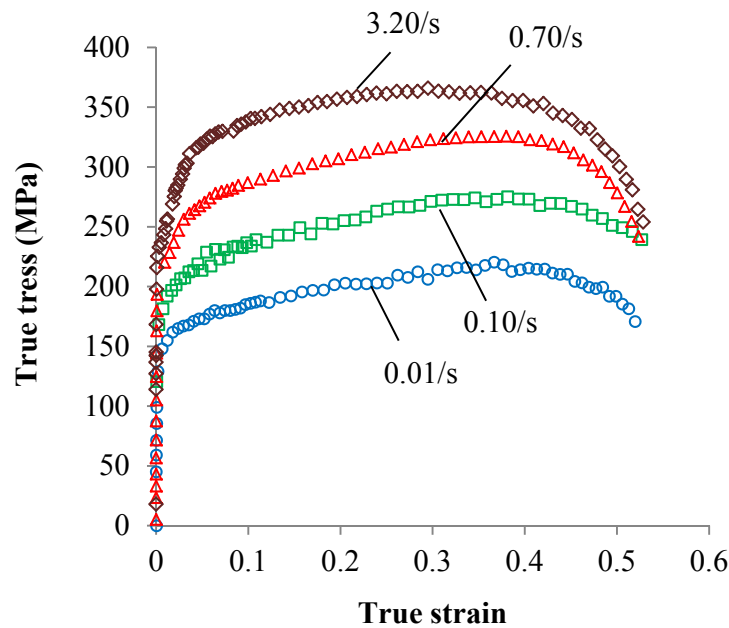


Figure 5.14 Experimental flow stress-strain relationships of the initial phase for different strain rates at a deformation temperature of 923 K

The influence of strain rate on the tensile behaviour of boron steel in the initial phase state has been investigated for a deformation temperature of 923K. Figure 5.14 illustrates the viscoplasticity of the alloy through a group of true stress-strain curves for strain rates of 0.01/s, 0.10/s, 0.70/s, and 3.20/s. A large increase in flow stress level with the increasing strain rate is shown at a small plastic deformation ($\epsilon_T < 0.005$), which reveals significant strain rate sensitivity of viscous stress for the initial phase of boron steel. For higher strains, flow stress keeps increasing gently for all strain rates, until the damage mechanism becomes dominant. Fracture takes place at almost the same strain level regardless of that value of strain rate. These features

suggest that microstructural recovery may not be pronounced for the initial phase of boron steel at the tested temperature.

- Temperature dependence

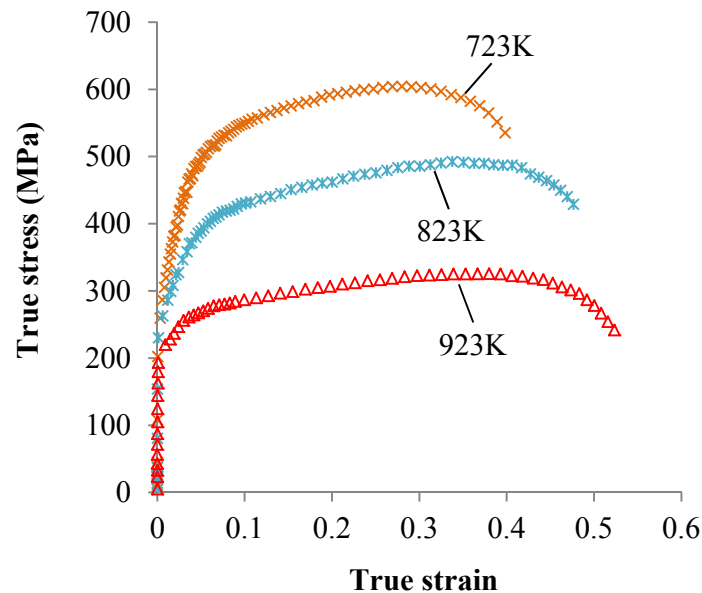


Figure 5.15 Experimental flow stress-strain relationships of the initial phase for different deformation temperatures (designed strain rate: 0.50/s)

The influence of temperature on the tensile behaviour of the initial phase has been investigated for a designed strain rate of 0.50/s. Figure 5.15 shows a group of true stress-strain curves for different deformation temperatures of 723K, 823K, and 923K. The real strain rates for each test are: 723K-0.35/s, 823K-0.50/s, 923K-0.70/s. The variations are negligible for the analysis. Similar to the curves for austenite in Figure 5.13, a lower strain hardening and peak flow stress level, but greater ductility, can be seen for a higher deformation temperature.

5.3.2 Characterisation of flow stress response

Further analysis has been carried out to quantify the effects of strain rate and temperature on the flow stress response of both phase states, which can provide necessary information for material

modelling. Moreover, the influence of flow stress features on deformation uniformity is discussed.

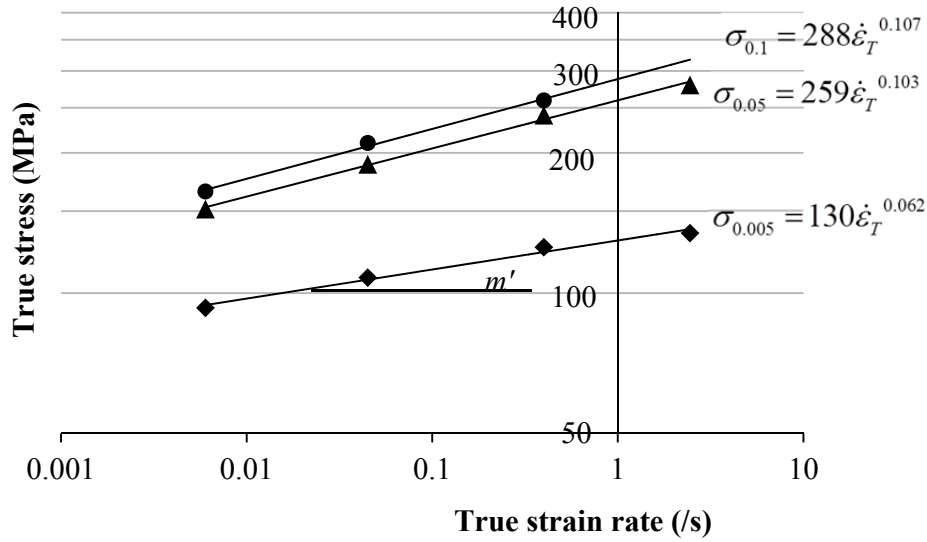
5.3.2.1 Effects of strain rate

Since a uniform thickness reduction is desired in hot stamped panels for automotive applications, deformations during forming normally correspond to low strains before the peak stress is achieved. The features of stress response during the hardening stage are critical to the deformation mode of the alloy. Flow stress at strain levels of 0.005, 0.05, and 0.1 are chosen for analysis in this study.

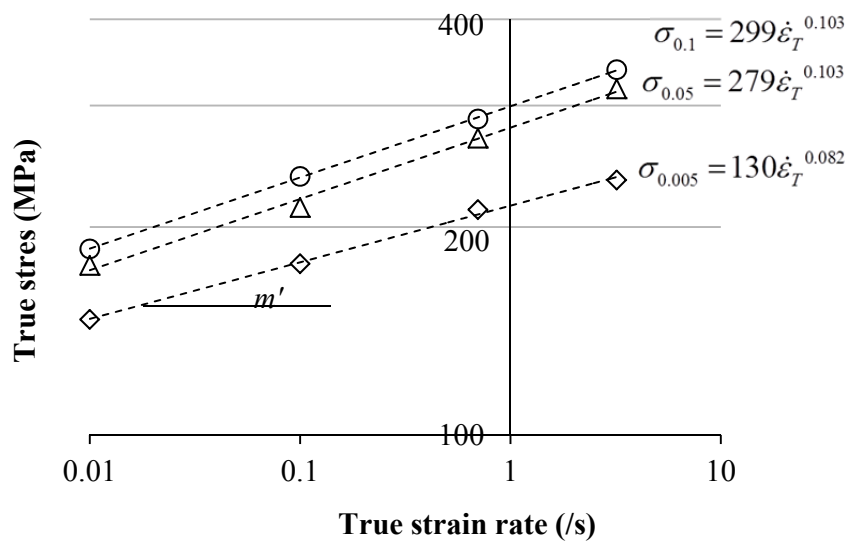
Figure 5.16 summarises stress values at the three strain levels for various strain rates: the subfigure (a) is for austenite tested at a temperature of 973K, and (b) is for the initial phase tested at 923K. By plotting logarithmic stress against logarithmic strain rate, linear fits have been obtained, which suggests the power law viscoplastic response of both phase states.

In both sub Figures 5.16 (a) and (b), for any strain rate, the stress increments with increasing strain level reveal the strain hardening characteristic; with respect to any strain level, the increase of stress with increasing strain rate exhibits the strain rate hardening characteristic. The strain rate hardening exponent is represented by the slope of trend lines, m' , and corresponds to the power exponent in the equations. For example, in subfigure (a), m' is 0.062 at $\varepsilon_T = 0.005$ and increases to 0.107 at $\varepsilon_T = 0.1$. It is a critical factor influencing the uniformity of deformation during forming processes. Generally, a larger m' value indicates a higher tendency to reduce the strain rate gradient within the material flow. When m' changes with strain, the flow condition is complex and the consideration of the trend of m' is important. For instance, austenite has a smaller m' value at $\varepsilon_T = 0.005$ compared with the initial phase, but larger m' increments for subsequent straining (from 0.005 to 0.05 and from 0.05 to 0.1). In this case, the locally larger deformation, which is deformed at a relatively greater strain rate, can be strongly impeded from

further developing. Therefore, for the two phase states deformed at their respective temperatures, there is possibility for austenite to achieve better deformation uniformity.



(a) Austenite tested at 973K, strain rates: 0.006/s, 0.045/s, 0.40/s, and 2.45/s



(b) Initial phase tested at 923K, strain rates: 0.01/s, 0.10/s, 0.70/s, and 3.20/s

Figure 5.16 Flow stress at different strain levels (0.005, 0.05, and 0.1) for different strain rates

5.3.2.2 Effects of temperature

Figure 5.17 summarises the flow stress values at true strain levels of 0.005, 0.05, and 0.1 for different deformation temperatures at the same designed strain rate of 0.50/s: the subfigure (a) is for austenite tested at temperatures of 873K, 973K, and 1073K; (b) is for the initial phase tested at 723K, 823K, and 923K. By plotting logarithmic stress against inverse temperature, the linear fit in subfigure (a) indicates that the temperature dependence of flow stress for austenite follows the standard Arrhenius activation energy equation; however, small deviations from linearity are observed for the initial phase in subfigure (b).

As can be seen, at strain levels of 0.05 and 0.1, the flow stress gradients with temperature are more pronounced for ferrite deformed in the temperature region (723K–923K) than austenite deformed between 873K–1073K. It suggests that the austenite is more likely to be deformed uniformly under selective heating and press hardening conditions.

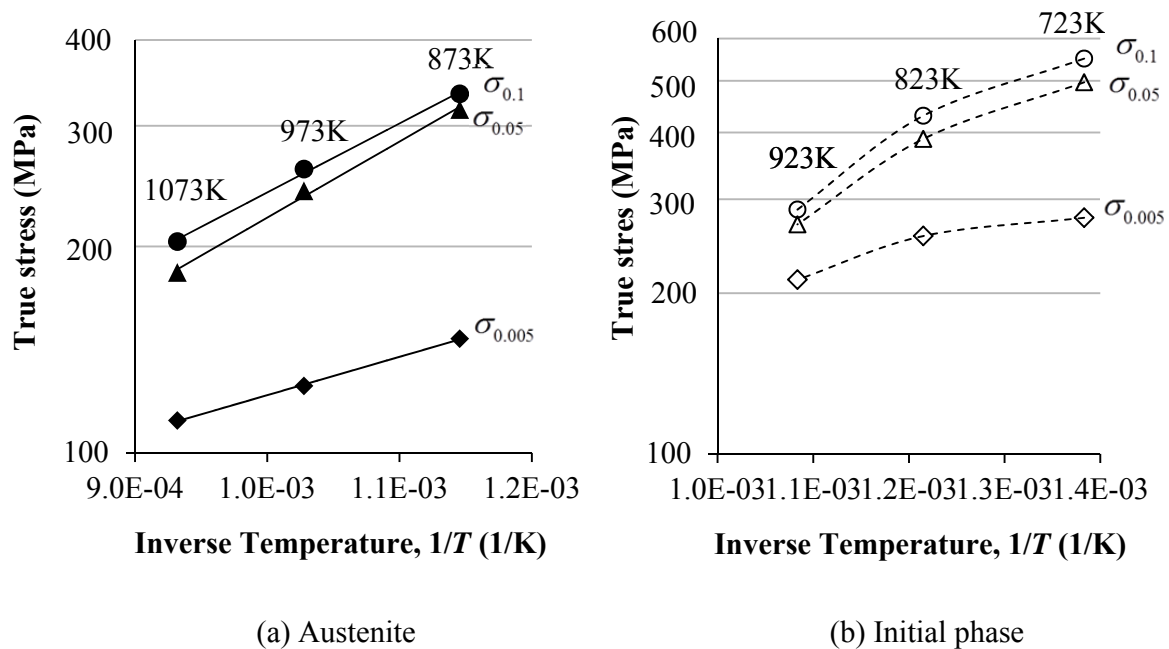


Figure 5.17 Flow stress at different strain levels (0.005, 0.05, and 0.1) for different deformation temperatures (designed strain rate: 0.50/s)

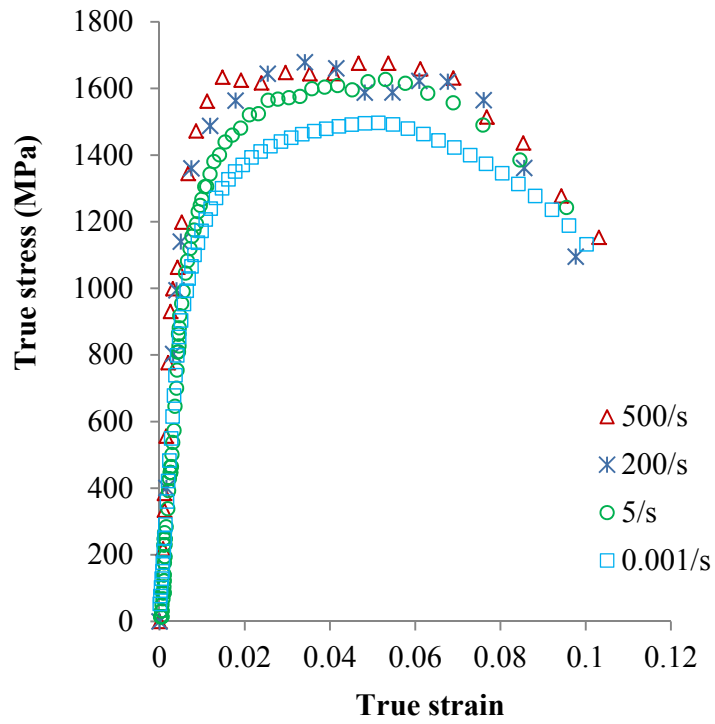
5.4 Mechanical properties of boron steels at room temperature

The flow stress-strain relationships for boron steel having various microstructures are obtained from tensile tests at room temperature. First, the dynamic tensile behaviour of martensite and initial phase over a wide of strain rates (up to 500/s) is discussed. Second, the mechanical properties of boron steels over a series of phase compositions (martensite volume fraction: $f_M = 0\%$ to 100%) are characterised.

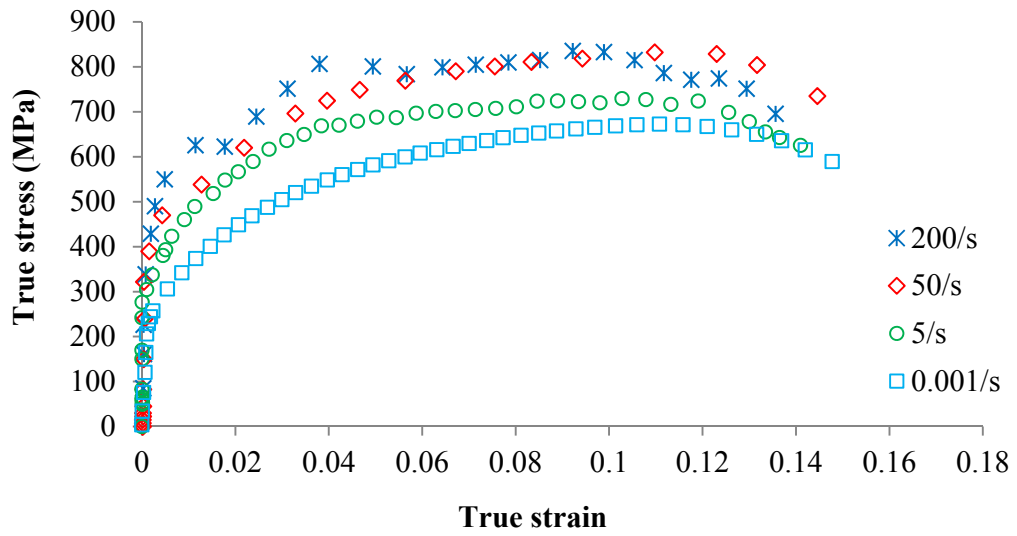
5.4.1 Dynamic tensile behaviour of the martensite and initial phase for boron steel

5.4.1.1 Results: flow stress-strain curves

The true stress-strain relationships of martensite and initial phase (ferrite and pearlite) for strain rate ranging from 0.001/s to 500/s have been achieved. Representative curves for each phase state are shown in Figure 5.18, where data for the high testing rate have been smoothed. It is well-known that martensite is a hard and brittle phase, while ferrite is soft and ductile and this is well manifested in the figure. For the same strain rate of 0.001/s, the true ultimate tensile strength (σ_{UTS}) values are 1499MPa and 620MPa for the martensite and initial phase respectively; while the elongations are 0.1 and 0.163. Here, σ_{UTS} refers to the true stress when the material is subjected to maximum tensile loading; elongation refers to the true strain at failure.



(a) Martensite ($f_M = 100\%$)



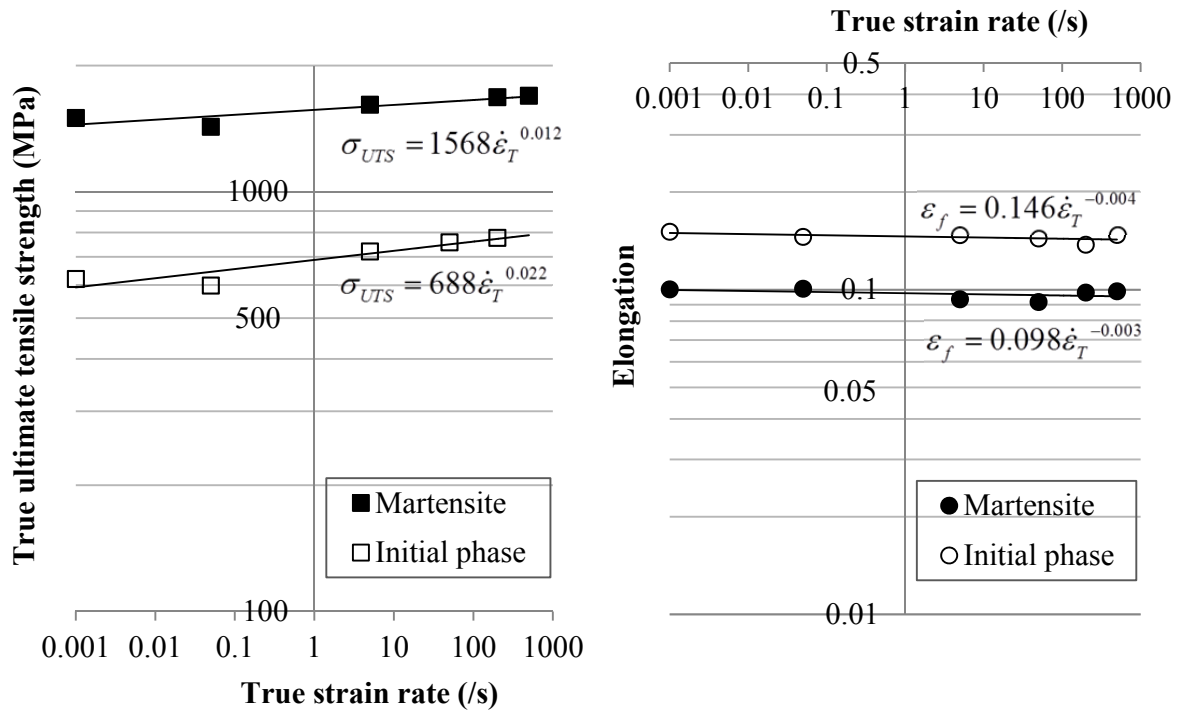
(a) Initial phase ($f_M = 0\%$)

Figure 5.18 True stress-strain curves of the martensite and initial phase of boron steels for different strain rates tested at room temperature

Over the large range of strain rate, viscoplastic properties are observed for both phase states. Both exhibit continuous-yielding at all strain rates for the cold deformations, no upper and lower yield point or yield point elongation can be seen. By comparison, the initial phase has a little higher viscosity and the martensite has stronger work hardening. No static recovery is expected to take place at room temperature [142], thus the increasing trend of flow curves could be the result of simultaneous dislocation hardening and dynamic recovery. For martensite, at all values of strain rate, the flow stress reaches a peak at about half elongation. For ferrite, at all values of strain rate, flow stress increases nearly until fracture. This feature further reveals the advantage of the initial phase in enhancing ductility. It is also consistent with the typical ductile fracture mode that damage accumulation evolves little at lower strain levels but continues at a rapid rate immediately prior to fracture [143]. For both phase states, the reduction of ductility with increasing strain rate can hardly be seen. This would benefit the performance of the alloy during impact.

5.4.1.2 Strain rate sensitivity of the phase states

To rationalise the strain rate sensitivity of the alloy, the trends in true ultimate tensile strength and elongation, as a function of true strain rate are examined in Figure 5.19 (a) and (b), respectively. By plotting logarithmic true ultimate tensile strength (σ_{UTS}) and elongation (ϵ_f) against logarithmic true strain rate ($\dot{\epsilon}_T$), linear fits are obtained, which accords with the power law viscoplastic response of both phase states. The strain rate hardening exponent (same as the definition in Figure 5.16) is found to be 0.012 for martensite and 0.022 for initial phase, which respectively corresponds to about 13% and 23% increase in the σ_{UTS} over 5 orders of magnitude change in strain rate. The ductility in both phase states exhibits very modest strain-rate sensitivity. In general, the initial phase shows more pronounced strain rate dependence, which is consistent with the theory that the strain rate sensitivity decreases with increasing strength level [144].



(a) Effects of $\dot{\epsilon}_T$ on true UTS (σ_{UTS})

(b) Effects of $\dot{\epsilon}_T$ on elongation (ϵ_f)

Figure 5.19 Effects of strain rate (0.001/s, 0.05/s, 5/s, 50/s, 200/s, and 500/s) on the tensile properties of the martensite and initial phase of the boron steel

5.4.2 Effects of microstructure on tensile behaviour of boron steel

5.4.2.1 Relationships between mechanical properties and phase composition

The values of true ultimate tensile strength (σ_{UTS}) under quasi-static testing, hardness (h), and martensite volume fraction (f_M) for representative samples having various phase compositions are summarised in Figure 5.20. The straight trend lines in the figure indicate that any two of the parameters are directly proportional to each other. With the increase of f_M in the boron steel, its strength and hardness increase. The reason to plot σ_{UTS} and f_M as a function of h is that, by adopting their relations, the mechanical-property/microstructural distribution in an as-formed boron steel panel can be easily evaluated by hardness measurement.

In this study, hardness (h) for full martensite and initial phase (78% proeutectoid ferrite and 22% pearlite) are 473HV and 173HV, respectively; when h is between about 285HV and 473HV, the steel is composed of proeutectoid ferrite and martensite; when h is between about 230HV and 285HV, the steel comprises proeutectoid ferrite, martensite, and a small amount of bainite; when h is between about 173HV and 230HV, a ferrite matrix with dispersions of pearlite, bainite and martensite phases, exists. Based on the relationships obtained in the figure, it is reasonable to simplify the multiphase boron steel as dual-phase of ferrite and martensite, and interpolate the value of f_M as the equivalent martensite volume fraction according to the hardness value for the range, 173HV–285HV.

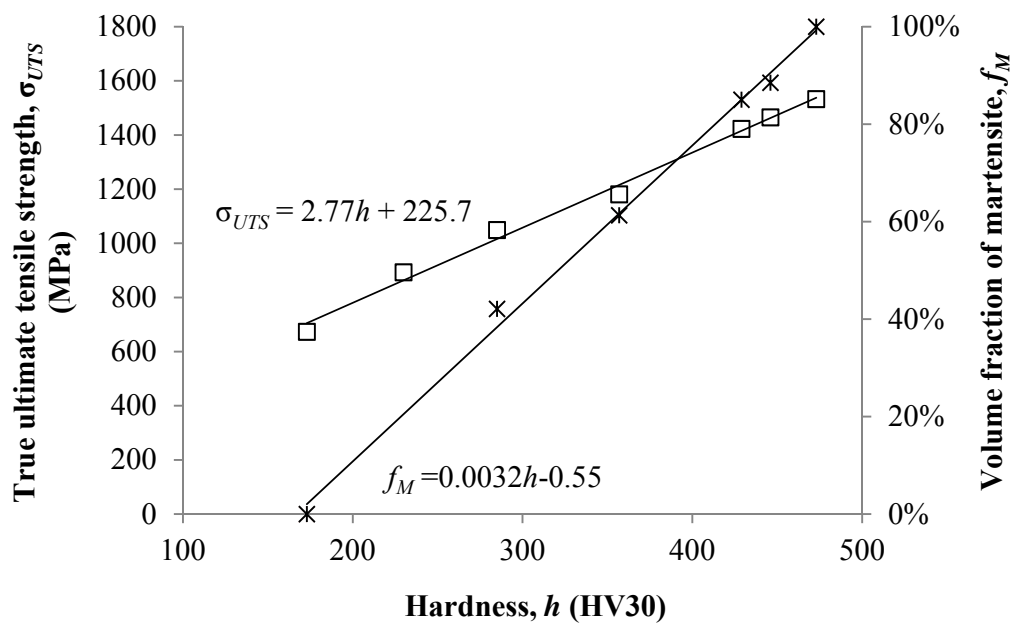


Figure 5.20 The relationships of true ultimate tensile strength and martensite volume fraction with hardness for heat treated boron steel with various phase compositions

5.4.2.2 Effects of phase composition on tensile properties

Figure 5.21 shows a series of representative true stress-strain curves. The volume fraction of martensite (f_M) measured for each phase state is marked on the corresponding curve. All curves

exhibit continuous yielding. With the increasing volume fraction of martensite, the flow stress level increases, and the ductility dramatically decreases first for $f_M = 0\%$ –61.3%. Ductility for $f_M = 61.3\%$ and 88.5% is less than that for full martensite.

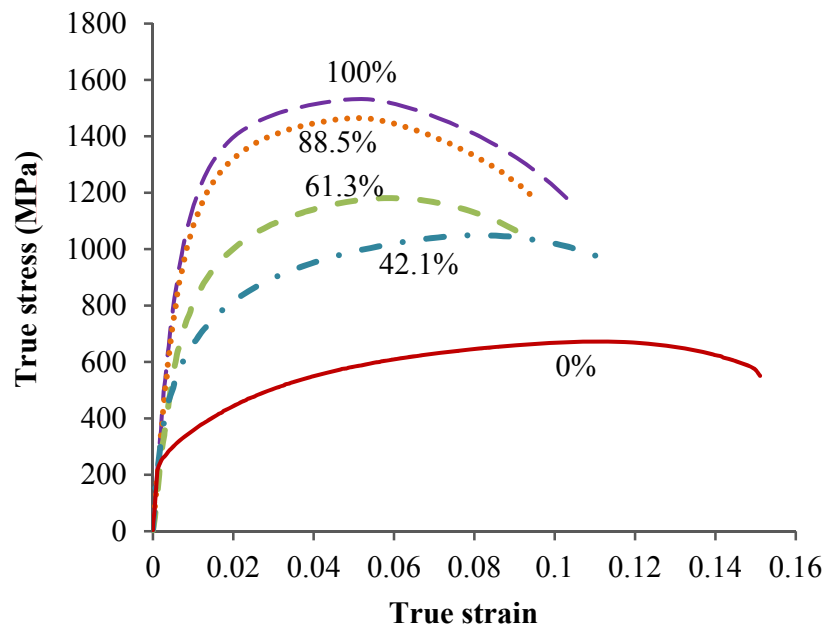


Figure 5.21 True stress-strain curves of heat treated boron steel with various volume fractions of martensite (quasi-static tests for the strain rate of 0.001/s at room temperature)

To further investigate the effects of phase composition on the tensile properties of boron steel, experimental values of true ultimate tensile strength (σ_{UTS}), 0.2% proof stress ($\sigma_{0.2\%}$) and elongation (ε_f), for all phase states, are plotted against the volume fraction of martensite (f_M) in Figure 5.22. The values of f_M for part of specimens without microstructural observation are calculated from their hardness values. Generally, the plastic behaviour (hardening and damage) of multiphase steels is governed by both phase composition in volume fraction and morphological distribution of the phases [145]. For example, several characteristics of the martensite phase have been shown to affect the degree of void damage development including: volume fraction, distribution, grain size, etc. [146, 147]. With respect to this work, since boron steel with different phase states are heat treated from the same initial microstructure, and

subjected to the heating rate and soaking time, variations in morphological factors can be neglected [148]. Therefore, it is reasonable to characterise the tensile properties of the studied boron steels only as a function of f_M .

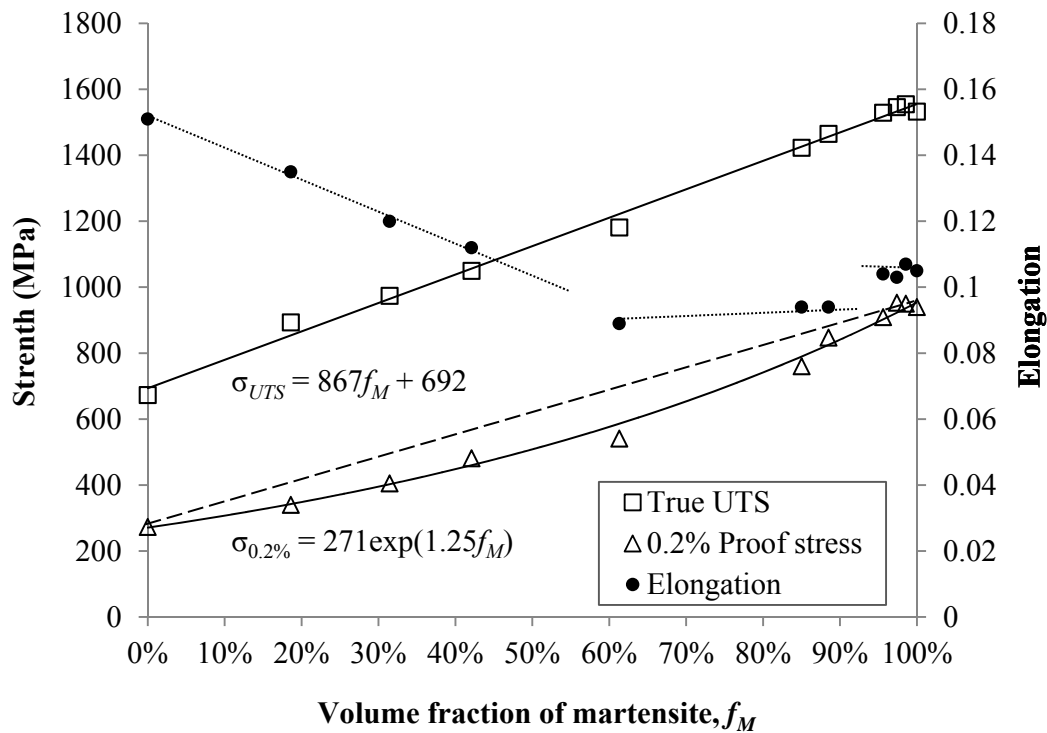


Figure 5.22 Effects of martensite volume fraction on tensile properties of heat treated boron steels (quasi-static tests for the strain rate of 0.001/s at room temperature)

As shown in Figure 5.22, stress level increases with increasing f_M due to the strengthening of hard phase martensite. The relationship between σ_{UTS} and f_M follows a linear fit, which has been presented in Figure 5.20. Interestingly, the relationship between 0.2% proof stress and f_M is found to follow an exponential fit better than a linear fit, which reveals the value of 0.2% proof stress for a multiphase composition is lower than the value expected for a linear fit. This might be explained as: for the multi-phase steels quenched from intercritical temperatures, as austenite is transformed to martensite during quenching, dislocations are formed in the ferrite phase to accommodate the shear deformation and volume expansion associated with the martensitic

transformation [149]. These highly mobile dislocations are responsible for the low yield strength and continuous yield behaviour [150].

The trend of elongation with martensite volume fraction is more complex: for f_M between about 0%–60%, an inversely proportional trend between elongation and f_M can be found; for f_M between about 60%–95%, apparent reductions in elongation are observed; for f_M higher than 95%, the values of elongation are almost identical. The poor ductility of dual phase boron steel corresponding to $f_M = 60\%$ –95% is noteworthy, for which the possible reason is proposed: if steel comprised of multiple phases is subjected to tension, stress concentrations and strain incompatibilities will arise, due to the interactions of different phases having different tensile properties. The mechanism of failure was found to be influenced by deformation localization due to microstructural inhomogeneity [151]. And the second phase can be treated as inhomogeneous inclusions embedded in a matrix [152]. For the studied steel, since pure ferrite and martensite phases have greatly different stress-strain behaviour, voids can be generated between the ferrite boundaries triggered by deformation mismatch with adjacent martensite particles or local stress concentrations, or at intersections of different phases initiated by negative internal pressure [143, 151]. This suggests that more voids are apt to be generated if there are more phase interfaces [31], which enhances damage development.

5.5 Summary

The effects of heating rate and temperature on austenite formation under both isothermal and non-isothermal conditions have been characterised. Rational understanding of the mechanisms which control the austenite formation in the boron steel has been obtained. The mechanisms involved in the deformation of the austenite and initial phase at elevated temperatures have been analysed; at the same time, the effects of strain rate and temperature on the deformation behaviour of the boron steel have been rationalised. The viscoplastic behaviour of the martensite

and initial phase subjected to high strain rate at room temperature has been observed and characterised; in addition, the empirical relations between mechanical properties (True ultimate tensile strength, 0.2% proof stress, elongation, and hardness) and phase compositions (volume fraction of martensite), for boron steel with various microstructures, have been summarised. The results and conclusions achieved in this chapter will be used for materials modelling in the next chapter.

CHAPTER 6 MATERIALS MODELLING

6.1 Introduction

In this chapter, following the tests and result analysis in Chapter 4 and Chapter 5, three sets of physically-based material models are defined: an austenite formation model for the boron steel during selective heating, and two viscoplastic-damage constitutive models respectively for boron steels under hot stamping conditions and in crash scenarios. Based on insight into microscopic mechanisms which act to cause the material changes, phenomenological approaches are adopted by modelling processes to capture the dominant features of phase transformation and mechanical response of boron steels at the macroscopic level.

6.2 Development of austenite formation model for the boron steel during selective heating

A physically-based material model is developed to describe the austenite formation in the boron steel during selective heating in hot stamping processes. The equations are formulated based on three austenite formation mechanisms: nucleation, growth and impingement. The evolution rate of state variables, such as extended volume, saturated volume fraction, and real volume fraction of austenite, are modelled. The data from heat treatment experiments are used to calibrate and validate the equations. Further analysis is made to illustrate the significance of the model in applications.

6.2.1 Model development

6.2.1.1 Extended volume of austenite

At the first step of the modelling, the equations will involve the calculation of extended volume of growing austenite phase. The definition of extended volume is based on a hypothesis assuming that nucleation and growth apply to an infinite volume of untransformed material, where every single nucleus is unaffected by the formation and growth of other nuclei [118, 119]. For this situation, the development of equations for nucleation and growth of austenite is described below.

In classic theory, nucleation rate is defined as the number of nuclei (particles of supercritical size) formed per unit volume, per unit time [96, 119]. It is determined by the number of particles of critical size and the rate of the jumping of atoms through the interface between initial phase and particles of critical size. For large overheating conditions, the nucleation rate of austenite can be formulated in the Arrhenius term [119, 153]:

$$\dot{N} = N_0 \exp\left(-\frac{Q_N}{RT}\right) \quad (6.1)$$

where R is the gas constant, T is the absolute temperature, Q_N is the activation energy for the jumping of atoms through the interface, and N_0 is the pre-exponential factor. This equation describes a nucleation mode of constant rate at a constant temperature without pre-existing nuclei (i.e. when $t = 0$, the number of nuclei: $N = 0$). Both Q_N and N_0 are temperature and time independent.

With respect to the pre-exponential factor N_0 , it can be formulated by characterizing the effects of influencing factors on the austenite formation. The internal influencing factors are related to the starting microstructure of the material, and the external ones are related to heating rate and temperature. For austenite nucleation in pearlite, Roosz et al. have investigated its dependence on

material structure [43, 101, 105, 113]. N_0 was proposed as a morphological function of interlamellar spacing (λ), the edge length of pearlite colony (a^p), and the number of nucleation sites (N_C):

$$N_0 = f(\lambda, a^p, N_C) \quad (6.2)$$

Furthermore, Caballero et al. [43, 101, 105, 113] extended the applications to non-isothermal conditions by adding the effects of heating rate (\dot{T}) into function (6.2):

$$N_0 = f(\lambda, a^p, N_C, \dot{T}) \quad (6.3)$$

In this study, because the model is specialized for a particular steel, the morphological parameters in equations (6.2) and (6.3) can simply be merged. The influence of heating rate on nucleation was suggested to be taken into account in terms of a power law, according to the analysis in the previous chapter. Thus, the nucleation rate can be modelled using:

$$\begin{aligned} \dot{N} &= \left(A_0 + A_1 \dot{T}^{\varphi_A} \right) \exp\left(-\frac{Q_N}{RT} \right) & (f_A \leq f_P) \\ &= 0 & (f_A > f_P) \end{aligned} \quad (6.4)$$

where Q_N is the activation energy for nucleation, R is the gas constant, \dot{T} is heating rate; A_0 , A_1 , and φ_A are constants characterizing the overall effects of internal and external influencing factors; f_A is the transformed volume fraction of austenite, and f_P is the initial volume fraction of pearlite. The austenite formation in the studied steel is via two routes: transformation from pearlite to austenite and from pro-eutectoid ferrite to austenite. It is expected that nucleation of austenite occurs only in pearlite colonies at the beginning of the transformation [42, 96, 109]. Thus equation (6.4) defines continuous nucleation and site saturation modes for the first and second step of the austenite formation, respectively. When dissolution of pearlite has finished ($f_A > f_P$), the saturation of nucleation sites causes a zero nucleation rate for the austenite-ferrite

transformation [119]. The first term in equation (6.4) represents static nucleation of austenite, and, the second is related to the dynamic effect of heating on austenite nucleation for $f_A \leq f_P$.

Similar to the formulation of nucleation rate, the volume growth rate of a nucleus (\dot{v}) is proposed in the Arrhenius term:

$$\dot{v} = v_0 \exp\left(-\frac{Q_v}{RT}\right) \quad (6.5)$$

where, Q_v is the activation energy for the volume growth, and v_0 is the pre-exponential factor.

Analytically, Q_v is a function of the activation energy for the front migration (Q_m), the growth mode parameter (m), and the dimensionality of the growth (d) [118, 119]:

$$Q_v = f(Q_m, m, d) \quad (6.6)$$

At the same time, the pre-exponent factor v_0 is given as [118, 119]:

$$v_0 = f(g, \eta) \quad (6.7)$$

where g is a particle-geometry factor, η is a growth factor determined by solute concentrations of the transformed and initial phases. Depending on the growth mode (interface controlled growth, volume diffusion controlled growth, or mixed-mode growth), the functions (6.6) and (6.7) can be formulated as various equations of great complexity.

Considering the trade-off between modelling comprehensiveness and mathematical simplicity, for the particular steel in this study, a straight forward equation to describe the volume growth rate of an austenite particle is proposed as:

$$\dot{v} = \left(B_0 + B_1 \dot{T}^{\varphi_B}\right) \exp\left(-\frac{Q_v}{RT}\right) \quad (6.8)$$

where Q_v is the activation energy for volume growth independent of temperature and time; B_0 , B_1 , and ϕ_B are material constants to be determined from experimental data. Q_v , B_0 , B_1 , and ϕ_B can be piecewise constants if the growth mode changes during transformation.

Assuming that all austenite nuclei grow at the same rate under same heating conditions, the growth rate of the extended volume of austenite (\dot{V}_e), in a unit of real sample volume, can be calculated by:

$$\dot{V}_e = N\dot{v} \quad (6.9)$$

Equation (6.9) expresses that the extended volume growth rate at any time is determined by both the existing quantity of formed nuclei and the instant growth rate of the nuclei.

6.2.1.2 Real volume fraction of austenite

Normally, since there is more than one nucleus growing during transformation, the extended volume of transformed phase should be correlated to real volume by taking impingement into account. The widely used model proposed by Avrami [96] is presented below:

$$f_A = 1 - \exp(-f'_A) \quad (6.10)$$

where f_A is the real volume fraction of transformed phase, and f'_A is the extended volume fraction which represents the extended volume of transformed phase in a unit of real sample volume (equivalent to V_e in this study). The interpretation of equation (6.10) can be made based on its differential form:

$$\frac{df_A}{dt} = (1 - f_A) \frac{df'_A}{dt} \quad (6.11)$$

For a time increment dt , the extended volume fraction increment of transformed phase is df_A' , but only part (as large as the untransformed volume fraction $(1-f_A)$) will contribute to the change of real volume fraction df_A [119].

This classical theory well accounts for the overlap of growing particles (hard impingement), but equations (6.10) and (6.11) are restricted to the case of hard impingement with all nuclei randomly dispersed [119]. With respect to diffusion controlled transformations, the transformation rate slows down when diffusion fields surrounding the new phase particles start to overlap [118, 119]. This mode is denoted as soft impingement [96, 118, 119], which deviates from the JMA kinetics mentioned above. In order to adapt the theory to complex nucleation and growth modes, appropriate adjustments of the formulation are necessary.

Therefore, for the purpose of correlation, an equation extended from equation (6.11) to describe the real volume fraction of austenite in this study is proposed as:

$$\dot{f}_A = (1 - f_A^m) \frac{\dot{V}_e}{(1 + V_e)^n} \quad (6.12)$$

where f_A is the real volume fraction of austenite, \dot{f}_A is the rate of f_A with time; V_e , as aforementioned, is the extended volume of austenite in a unit of real sample volume which is equivalent to f_A' , in equations (6.10) and (6.11), \dot{V}_e is the rate of V_e . m , which is related to the initial volume fraction of pearlite (f_p), and n are transformation related parameters given by:

$$\begin{aligned} m &= 1 & (f_A \leq f_p) \\ &= 1 - m_0(f_A - f_p) & (f_A > f_p) \end{aligned} \quad (6.13)$$

$$n = n_0 \dot{f}_A^{\varphi_n} \quad (6.14)$$

where m_0 , n_0 , and φ_n are constants.

6.2.1.3 Saturated volume fraction of austenite

If the steel is annealed at intercritical ($\alpha + \gamma$) region, as discussed in Chapter 5, full austenite formation cannot be achieved. Given sufficient soaking time, the volume fraction of austenite at final equilibration is a function of the intercritical annealing temperature [43, 99, 104, 117]. For the boron steel in this study, the phenomenological approach is employed in the development of the transformation models for modelling. According to the experimental investigation in the previous chapter, after isothermal soaking for 10-15 min at a chosen temperature, the growth rate of austenite volume fraction becomes zero. Thus the saturated volume fraction of austenite, f_{As} at that temperature can be modelled using:

$$f_{As} = \frac{C_2}{\pi} \arctan \left(C_1 \left(\frac{T}{T_{As}} - 1 \right) \right) + C_3 \quad (6.15)$$

where C_1 , C_2 , C_3 and T_{As} are constants to be calibrated from experimental data.

The equations developed in subsection 6.2.1.2 are applied for full austenite formation in the γ region. Adjustments are required to adapt the model for intercritical transformations. From experimental observation described in the previous chapter, it was found that isothermal austenite formation at different intercritical temperatures followed the same trend approaching equilibration. Therefore, it is reasonable to substitute the item $(1 - f_A^m)$ in equation (6.12), which indicates the 100% austenite formation, with $(f_{As}^m - f_A^m)$ (partial austenite formation). Then equation (6.12) becomes:

$$\dot{f}_A = (f_{As}^m - f_A^m) \frac{\dot{V}_e}{(1 + V_e)^n} \quad (6.16)$$

6.2.2 Formulation of unified constitutive equations

By introducing variables such as extended volume, saturated volume fraction, and volume fraction of austenite, a set of unified constitutive equations, which are based on the mechanisms of nucleation, growth and impingement, can be formulated to model the austenite formation in the boron steel. For the convenience of discussion, the equation set is given first:

$$\begin{aligned}\dot{N} &= (A_0 + A_1 \dot{T}^{\varphi_A}) \exp\left(-\frac{Q_N}{RT}\right) & (f_A \leq f_P) \\ &= 0 & (f_A > f_P)\end{aligned}\quad (6.17)$$

$$\dot{v} = (B_0 + B_1 \dot{T}^{\varphi_B}) \exp\left(-\frac{Q_v}{RT}\right) \quad (6.18)$$

$$\dot{V}_e = N \dot{v} \quad (6.19)$$

$$\dot{f}_A = (f_{As}^m - f_A^m) \frac{\dot{V}_e}{(1 + V_e)^n} \quad (6.20)$$

where

$$f_{As} = \frac{C_2}{\pi} \arctan\left(C_1 \left(\frac{T}{T_{As}} - 1\right)\right) + C_3 \quad (6.21)$$

is the saturated volume fraction of austenite, and, the parameters m and n are defined as:

$$\begin{aligned}m &= 1 & (f_A \leq f_P) \\ &= 1 - m_0(f_A - f_P) & (f_A > f_P)\end{aligned}\quad (6.22)$$

$$n = n_0 \dot{f}_A^{\varphi_n} \quad (6.23)$$

where \dot{N} and N are the nucleation rate and nuclei quantity of austenite per unit sample volume, respectively; \dot{v} is the volume growth rate of an austenite nucleus; V_e is the extend volume of transformed austenite per unit sample volume, and its growth rate is modelled using equations

(6.19); f_A is the volume fraction of austenite and its formation rate is expressed by equation (6.20); m and n are parameters to characterise the impingement mechanism; R is the gas constant and T is the absolute temperature; f_p is the volume fraction of pearlite in the initial structure; $A_0, A_1, \varphi_A, Q_N, B_0, B_1, \varphi_B, Q_v, C_1, C_2, C_3, T_m, m_0, n_0, \varphi_n$ are constants to be determined from experimental data.

The unified theory is used in this study for the development of the austenite formation model consisting of multiple evolutionary equations. The variables in equations (6.17) – (6.20) have their individual physical meanings related to the microstructural evolution during austenite formation processes. The features and interactive effects of physical phenomena during the transformation can thus be described. It is noted that the morphological parameters of the material are merged and not counted individually in the equations, which allows the simplicity of modelling work. But, in this case, a set of constants fits only a particular steel variant. Re-determination of the constants is required when the initial microstructure of the steel is changed.

The materials model, equations (6.17) – (6.20), is a set of Ordinary Differential Equations (ODE) in terms of time t , which can be solved with given initial values for the variables. Thus this is also known as the solution for an initial value problem. In the numerical integration of solving the equations, at $t=0, N=0, v=0, V_e=0$ and $f_A=2\%$ for the starting temperature of 993K (further explanation about this is given in subsection 6.2.3.1). Below this temperature, austenite formation is not possible.

6.2.3 Determination of the equations

6.2.3.1 Calibration of the constants from experimental data

The model was calibrated by fitting the computed volume fraction of austenite to the experimental results by adjusting the values of constants within the equations. The trial and error method was adopted in the study.

The first step of calibration was to determine the constants from equation (6.21), where the saturated austenite volume fraction f_{As} is a function of temperature. The values of the constants in the equation are adjusted to get the best fit to the experimental points at 1023K, 1073K, 1123K, and 1173K, as shown by symbols in Figure 6.1.

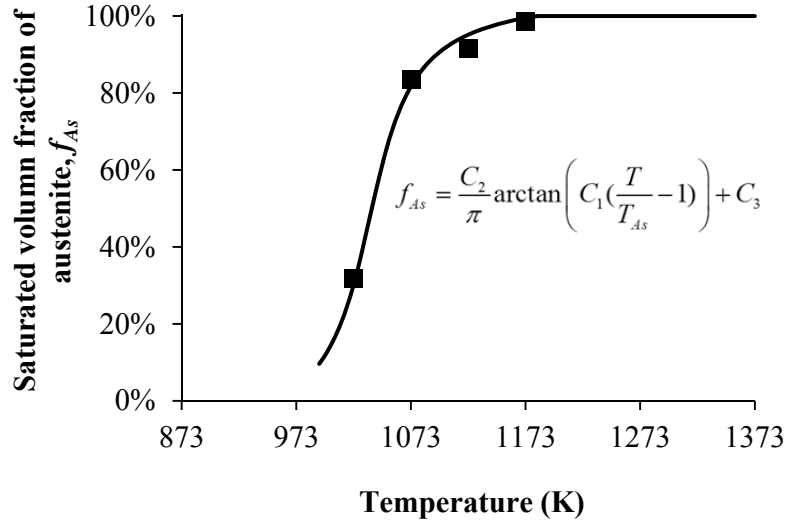
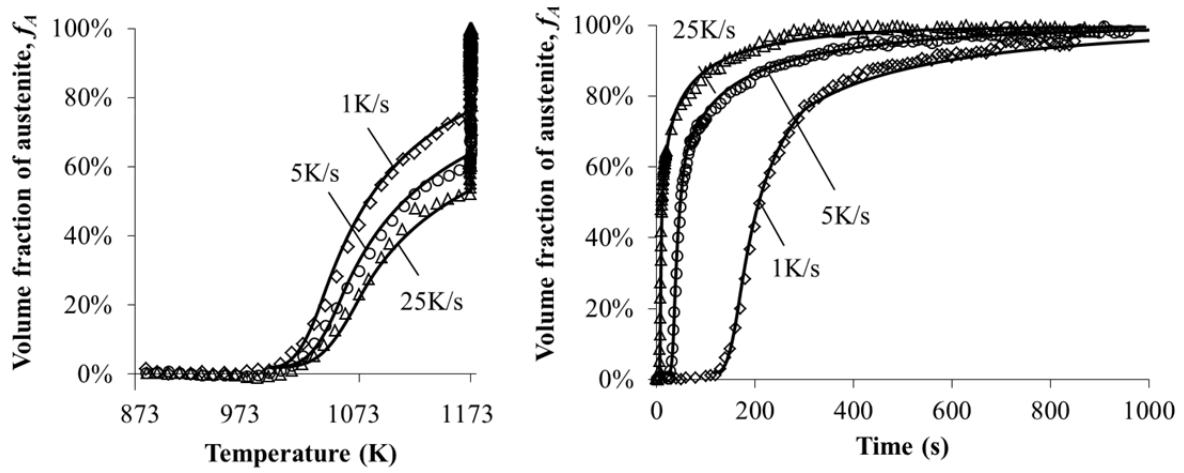


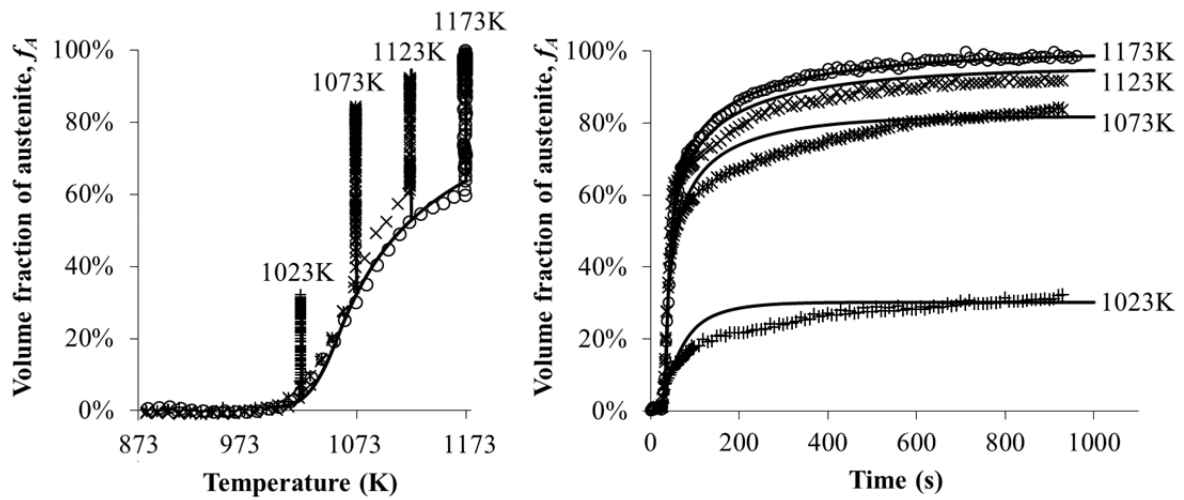
Figure 6.1 Comparison of experimental (symbols) and computed (solid curve) saturated volume fraction of austenite at intercritical annealing temperatures using equation (6.21)

At the second step, the computation was conducted in an iterative and incremental manner. Equations (6.17) – (6.20) were numerically integrated using the forward Euler method. The input was initial values of the state variables and temperature profile. According to information provided by the material supplier, A_{e1} for the steel is 993K, at which about 2% of austenite volume formation is visible. Therefore, the integration starts from 993K with $f_A = 2\%$. At the same time, the initial values of N , v , and V_e are defined as zero, and f_{As} is given by employing equation (6.21). The output was the integrated values of the variables. The evolution of f_A was used for fitting with experimental curves. The calibrated constants are listed in Table 6.1. Figure 6.2 shows the comparison of experimental (symbols) and computed (solid curves) volume fraction of austenite formation with temperature and time under different heating rates and

soaking temperatures. Good agreements have been obtained and the features of experimental data are exhibited clearly from the computed curves.



(a) Different heating rates (soaking temperature: 1173K)



(b) Different soaking temperatures (heating rate: 5K/s)

Figure 6.2 Comparison of experimental (symbols) and numerical integrated (solid curves) volume fractions of austenite formation under different heating conditions for calibration

Table 6.1 Material constants for equations (6.17) – (6.23)

Q_N (J/mol)	Q_v (J/mol)	A_0	A_1	B_0	B_1	φ_A	φ_B	A_{e1} (K)
149000	40000	176000	2.2e5	9.2	9.2	1.4	0.12	993
C_1	C_2	C_3	T_{As} (K)	m_0	f_P	n_0	φ_n	R (J/mol·K)
36.0	1.2	0.475	1037	1.05	0.22	2.1	0.155	8.314

6.2.3.2 Validation and analysis

To validate the material model, a further computation was carried out using the determined material constants listed in Table 6.1 for heating rate 2K/s, soaking at 1273K for 2min. As shown in Figure 6.3, the predicted volume fraction of austenite with temperature and time (solid curves) both agree well with the experimental ones (symbols).

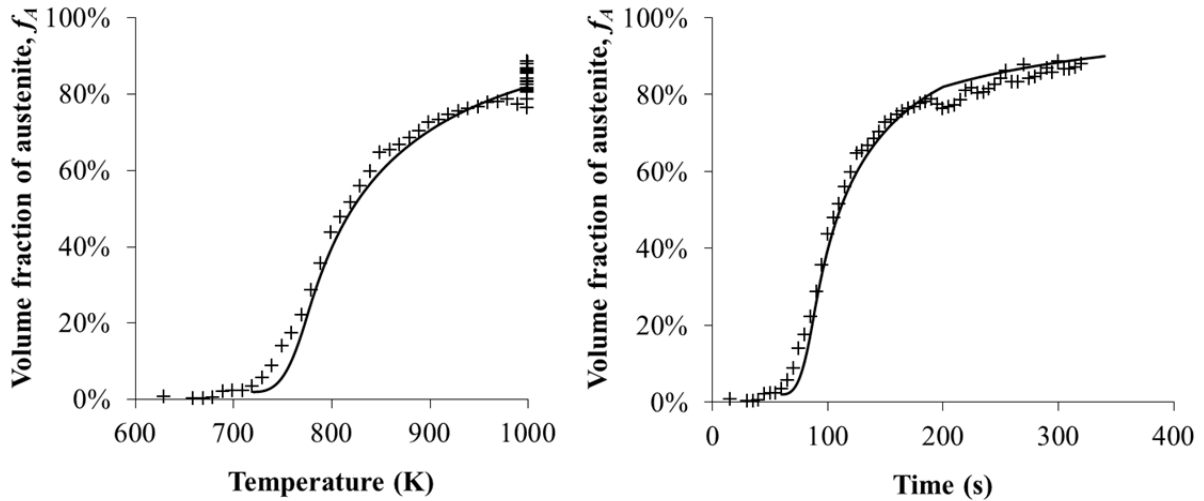


Figure 6.3 Comparison of experimental (symbols) and predicted (solid curves) volume fractions of austenite formation for validation (heating rate: 2K/s, soaking temperature: 1273K)

Prediction of continuous heating transformation (CHT) diagram has great value for guiding the design of heat treatment in practice. In Figure 6.4, the temperature and time to attain chosen volume fractions of austenite (10%–70%) under continuous heating at different heating rates (1–25K/s) have been predicted by using the determined model. The computed CHT data is represented by solid curves. The data points which are available from experimental results are provided in the figure as cross symbols. Most of the symbols lie on or close to the computed curves, which again shows the reliability of the model. The predicted CHT diagram reveals that the temperature to attain chosen proportions of austenite increases with increasing heating rate and the effect is greater for higher austenite volume fractions; at a certain heating rate, the temperature increment to increase austenite volume fraction by 20% is larger from higher austenite volume fraction.

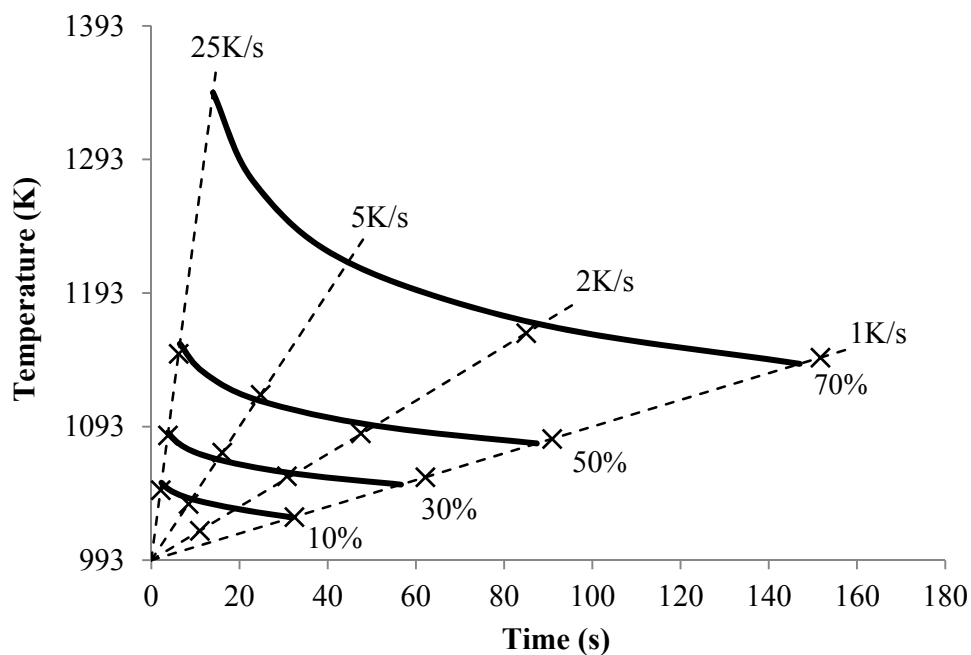


Figure 6.4 Comparison of experimental (symbols) and predicted (solid curves) continuous heating transformation (CHT) data, which are shown for different volume fractions of austenite (10%–70%) with various heating rates (1–25K/s)

Control of soaking time is of great significance in enhancing productivity and reducing cost in practice. In Figure 6.5, the soaking time increments to attain 80%–90% austenite volume fraction at 1173K with different pre-heating rates (1–25K/s) have been predicted and summarised as a solid line. The symbols are experimental data. Good agreement is shown again in this case. The predicted trend indicates that for a chosen stage of transformation and a chosen soaking temperature, less time is required for the steel preheated at a higher rate.

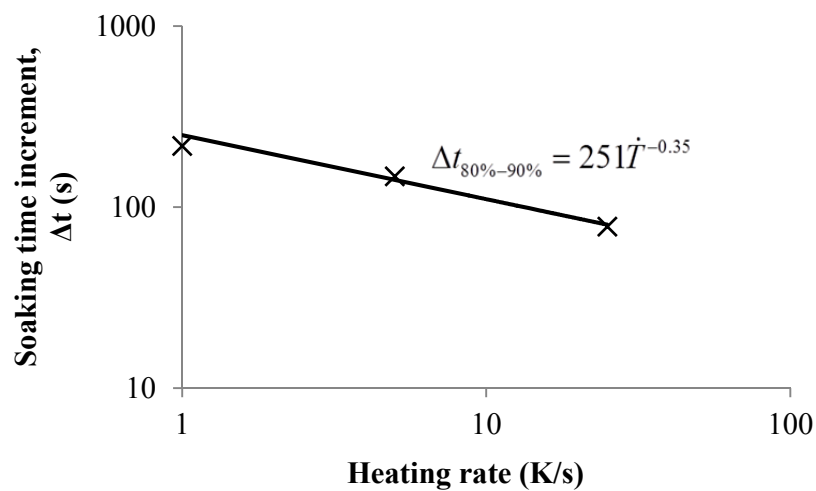


Figure 6.5 Comparison of experimental (symbols) and predicted (solid line) relationships of time increment to attain 80%–90% austenite volume fraction under an isothermal condition (1173K) with various heating rates (1–25K/s)

6.3 Viscoplastic-damage constitutive model

Viscoplastic constitutive equations are normally used to model the behaviour of metals that are subjected to stress at elevated temperatures (normally $T > 0.5T_m$, T_m is melting temperature) or deformed at high strain rates (normally $\dot{\epsilon} > 100/\text{s}$) [154]. In this section, a dislocation-based viscoplastic-damage model based on the work by Lin et al. [155-157] is introduced. The unified theory has been used for the development of the constitutive model consisting of multiple evolutionary equations, through which the evolution rates of state variables, such as plastic strain,

normalised dislocation density, and damage are modelled. The equations are adopted in section 6.4 and expanded in section 6.5, to describe the deformation behaviour of boron steels observed in the hot and cold tensile tests, respectively.

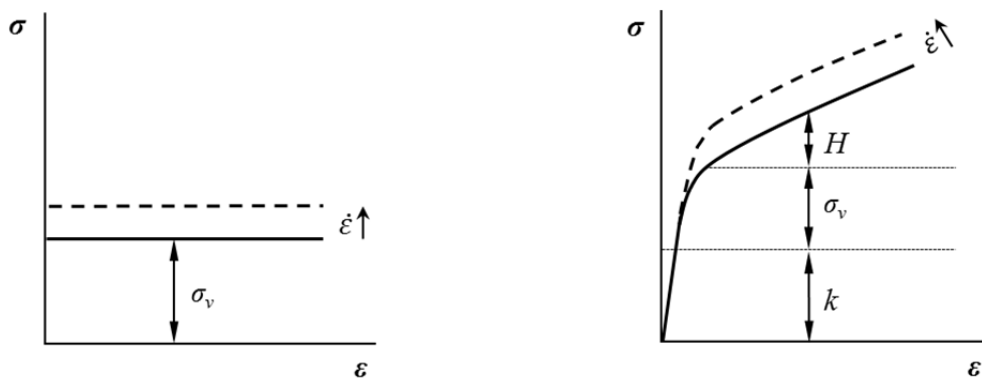
6.3.1 Flow rule

A flow rule normally describes the flow stress response to the rate and extent of plastic straining for viscoplastic solids, incorporating factors such as initial yield, viscoplastic effects, and work hardening.

For a rigid perfect viscoplastic solid, as shown in Figure 6.6 (a), the relationship between flow stress, which is equal to viscous stress σ_v , and plastic strain rate $\dot{\varepsilon}^P$ can be described by Norton's law [138]:

$$\dot{\varepsilon}^P = \left(\frac{\sigma_v}{\lambda^*} \right)^n \quad (6.24)$$

where λ^* and n are temperature dependent material parameters. Although the equation was originally formulated as an empirical fit, similar results have been obtained by studying the motion of dislocations [158, 159].



(a) Rigid perfect viscoplasticity

(d) Elasto-viscoplasticity with isotropic hardening

Figure 6.6 Flow stress-strain responses of viscoplastic solids

In practice, most metals and alloys show plastic yield and work hardening during straining. Thus, as shown in Figure 6.6 (b), the flow stress σ can be taken as the sum of initial yield stress k equal to the elastic limit, viscous stress σ_v representing the viscoplastic effects, and strain hardening H caused by the interaction of dislocations, i.e. $\sigma = k + \sigma_v + H$ [138, 155]. In this case, the σ_v in equation (6.24) can be substituted by $(\sigma - k - H)_+$, where the bracketed terms are used to indicate that only positive results are valid [156]. The flow law is thus expressed as [61, 63]:

$$\dot{\varepsilon}^P = \dot{\varepsilon}^o \left(\frac{\sigma - k - H}{K} \right)_+^{n_v} \quad (6.25)$$

where $\dot{\varepsilon}^o$ is equal to 1 under tension and -1 under compression, K is a parameter related to viscous stress, and n_v is viscous exponent. A higher value of n_v indicates a less variation in stress for a certain change of straining rate, that is, the viscoplastic effects are weaker. When $n_v > 20$, the deformation behaviour of material is closed to plasticity [16, 160]. Both K and n_v are temperature dependent. They are given by Arrhenius-type equations (6.26) and (6.27), respectively, indicating the reduction in viscous stress and increase in viscosity with increasing temperature.

$$K = K_0 \exp\left(\frac{Q_K}{RT}\right) \quad (6.26)$$

$$n_v = n_{v0} \exp\left(\frac{Q_n}{RT}\right) \quad (6.27)$$

where K_0 and n_{v0} are material constants, and Q_K and Q_n are activation energy related to the viscosity of material, R is the gas constant and T is the absolute temperature.

The initial yield stress k decreases as temperature increases, since the external energy required to overcome obstacles to plastic straining decreases [161]. It is also expressed in the Arrhenius term:

$$k = k_0 \exp\left(\frac{Q_k}{RT}\right) \quad (6.28)$$

where k_0 is a material constant, and Q_k is the activation energy associated with initial plastic slip. The hardening term H is formulated in terms of dislocation-based equations in the following subsections.

6.3.2 Isotropic work hardening

The increased dislocation density due to plastic deformation raises the resistance of a metallic material, and the material is thus work hardened. Lin et al. [61-63] used the equation below to describe the isotropic work hardening as a function of normalised dislocation density:

$$H = B \bar{\rho}^{n_R} \quad (6.29)$$

where B is a temperature parameter given by:

$$B = B_0 \exp\left(\frac{Q_B}{RT}\right) \quad (6.30)$$

where B_0 is a material constant, and Q_B is the activation energy associated with hardening mechanisms.

$\bar{\rho}$, termed normalised dislocation density, is used as a practical expression of the dislocation state of material (further details are given in the following subsection) [156].

n_R is hardening exponent. From Nes's study [162], as the dislocation density increases, the average distance that the mobile dislocations migrate before being stored (also called mean dislocation free path, L) decreases. As a result, higher stress is required to continue plastic straining. The mean dislocation free path (L) allowing for dislocation migration is governed by the inverse square of the dislocation density (ρ), i.e. $L \propto \rho^{-0.5}$; at the same time, the hardening

stress (H) is inversely proportional to the mean dislocation free path (L), i.e. $H \propto L^{-1}$. Therefore, the value of n_R is theoretically suggested to be 0.5. However, refinement is needed for particular materials and working conditions. The value $n_R = 0.4$ was adopted by Cai for modelling boron steels under hot stamping conditions [16].

Compared with the classical strain hardening law ($H = B\varepsilon^n$) which is an empirical approximation without physical base, the dislocation-based equations are capable of capturing the material behaviour at the microscopic level. Although still termed hardening laws, equations (6.29) and (6.30) can account for material softening from a reduction in the dislocation density. The evolution of dislocation density and associated recovery mechanisms are introduced in the following subsection.

6.3.3 Evolution of dislocation density

Lin et al. [62] summarised that two mechanisms contribute to net accumulation rate of dislocation for a non-recrystallizing metal: trapping of dislocations during plastic slip and annihilation of dislocations from recovery processes, i.e. $\dot{\rho} = \dot{\rho}_{Store} - \dot{\rho}_{Recover}$.

A normalised dislocation density concept was defined by Lin et al. [61, 62] as $\bar{\rho} = 1 - \rho_0/\rho$, where ρ_0 is the initial dislocation density of material, and ρ is the instantaneous dislocation density during deformation. The normalised dislocation density varies from 0 (the initial state) to 1 (the saturated state of a dislocation network after severe deformation) [62]. Based on the definition, a constitutive equation for the evolution of dislocation density has been proposed as [16, 62, 63, 141]:

$$\dot{\bar{\rho}} = A(1 - \bar{\rho})|\dot{\varepsilon}^P| - C\bar{\rho}^{\gamma_2} \quad (6.31)$$

where A and γ_2 are material constants, C is a temperature dependent parameter. The first term in the equation represents the storage of dislocations during plastic slip and concurrent reduction in dislocations due to dynamic recovery. Dynamic recovery is due to continuous reorganisation of dislocations during deformation, which is in terms of dislocation climb at high temperature and dislocation cross-slip at low temperature [62, 63]. By adopting the dynamic recovery term, the normalised dislocation density can be limited to the saturated state of a dislocation network being 1 [62]. The second term in equation (6.31) represents the effects of static recovery. The static recovery is a function of time and is favoured by thermal activation [19]. At elevated temperatures, annealing can effectively remove dislocations from the matrix [16]. Thus this term is normally taken into account for hot working conditions. To show greater effects for a higher temperature, the parameter C is given as:

$$C = C_0 \exp\left(-\frac{Q_c}{RT}\right) \quad (6.32)$$

where C_0 is a material constant, and Q_c is the activation energy associated with static recovery mechanisms.

By using equations (6.31) and (6.32), the dislocation recovery mechanisms are manifested as a decrease in the hardening at the macroscopic level [138]; the absolute values of dislocation density are not required.

6.3.4 Evolution of damage

The damage concept has to be introduced to model the failure of materials, which is necessary for the prediction of formability under hot forming conditions, and especially important for the load bearing analysis in crash scenarios. By implementing damage evolution equations into elasto-

viscoplastic constitutive equations, ductility and reduction of flows tress in the late stage of deformations can be predicted [139].

Damage mechanisms vary with the microstructure of materials and working conditions, the major type of which for metallic materials have been summarised by Lin et al. [139]. In this study, damage evolution under cold working conditions involves void nucleation, growth, and coalescence [142]; the damage mechanism for hot stamping conditions is associated with both ductile continuum void growth in grains and microwedge cracking at grain boundaries [139]. A ‘plasticity-induced’ ductile damage model, which has been proposed by Lin et al. [139] and applied for both cold working and hot stamping conditions [16, 163], is given as:

$$\dot{\omega} = \beta \frac{\sigma^{\gamma_3} |\dot{\varepsilon}^P|}{(1-\omega)^\varphi} \quad (6.33)$$

where $\dot{\omega}$ is damage evolution rate, which could be influenced by plastic strain rate $\dot{\varepsilon}^P$, flow stress level σ , and the development of damage ω itself. The value of ω lies in the range from 0 to 1, indicating that the state of material changes from undamaged to completely failed. In practice, metals fail at a damage value lower than 1. γ_3 and φ are material constants providing flexibility to the damage model. If the strain-rate-induced flow stress variation does not influence damage evolution (manifested by strain rate dependency of ductility at the macroscopic level), 0 is given to the value of γ_3 . β is given in terms of Arrhenius-type equation for hot working conditions:

$$\beta = \beta_0 \exp\left(\frac{Q_\beta}{RT}\right) \quad (6.34)$$

where β_0 is a material constant, Q_β is the activation energy associated with damage mechanisms.

6.3.5 Modified flow rule and Hooke's law

The damage term should be taken into account in the flow stress-strain relationship. Since the imposed stress is sustained by a decreasing amount of load bearing material as damage accumulates, the material is considered to be subjected to an augmented stress over the undamaged area $1-\omega$, creating an effective stress of $\sigma/(1-\omega)$ for further plastic deformation and damage evolution [156]. Thus, the flow rule of equation (6.25) is modified as:

$$\dot{\varepsilon}^P = \dot{\varepsilon}^o \left(\frac{\left| \frac{\sigma}{1-\omega} \right| - k - H}{K} \right)^{n_f}$$

If $\left| \frac{\sigma}{1-\omega} \right| - k - H \leq 0$, $\dot{\varepsilon}^P = 0$ (6.35)

$$\begin{aligned} \dot{\varepsilon}^o &= 1 & (\sigma > 0) \\ &= -1 & (\sigma < 0) \end{aligned}$$

The deformation of a yielding solid with an imposed stress consists of reversible/elastic strain ε^E and irreversible/plastic strain ε^P , i.e. $\varepsilon^T = \varepsilon^E + \varepsilon^P$. From Hooke's law, flow stress can usually be related to elastic strain as: $\sigma = E(\varepsilon^T - \varepsilon^P)$, where E is Young's modulus of elasticity [138]. Again, by taking the damage softening effects into account, the Hooke's law is given as:

$$\sigma = E(1-\omega)(\varepsilon^T - \varepsilon^P) \quad (6.36)$$

Young's modulus E is temperature dependent, and difficult to determine at elevated temperatures [156]. An Arrhenius-type equation used by Cai [16] for modelling boron steels are adopted here:

$$E = E_0 \exp\left(\frac{Q_E}{RT}\right) \quad (6.37)$$

where E_0 and Q_E are constants.

6.4 Unified viscoplastic-damage constitutive equations for boron steels under hot stamping conditions

The viscoplastic-damage constitutive model introduced in the previous section is adopted to account for the viscoplastic behaviours of the austenite and initial phase (78% ferrite and 22% pearlite) of boron steel under hot stamping conditions. The values of material constants in the equations corresponding to each phase state are calibrated from the respective experimental true stress-strain data. Further analysis on the modelling results is made.

6.4.1 Formulation of unified viscoplastic-damage constitutive equations

Based on the mechanisms of dislocation-driven evolution processes such as hardening, dynamic and static recovery and damage, linked with the experimental characterisation of the effects of forming temperature and strain rate, a set of unified viscoplastic-damage constitutive equations are listed below to model the thermo-mechanical response of boron steels:

$$\dot{\varepsilon}^P = \dot{\varepsilon}^o \left(\frac{\left| \frac{\sigma}{1-\omega} \right| - k - H}{K} \right)^{n_f} \frac{1}{(1-\omega)^{\gamma_1}}$$

$$\text{If } \left| \frac{\sigma}{1-\omega} \right| - k - H \leq 0, \quad \dot{\varepsilon}^P = 0 \quad (6.38)$$

$$\begin{aligned} \dot{\varepsilon}^o &= 1 & (\sigma > 0) \\ &= -1 & (\sigma < 0) \end{aligned}$$

$$H = B \bar{\rho}^{n_R} \quad (6.39)$$

$$\dot{\bar{\rho}} = A(1-\bar{\rho}) \left| \dot{\varepsilon}^P \right| - C \bar{\rho}^{\gamma_2} \quad (6.40)$$

$$\dot{\omega} = \beta \frac{\sigma^{\gamma_3} \left| \dot{\varepsilon}^P \right|}{(1-\omega)^\varphi} \quad (6.41)$$

$$\sigma = E(1 - \omega)(\varepsilon^T - \varepsilon^P) \quad (6.42)$$

where the temperature dependent parameters are defined by:

$$k = k_0 \exp\left(\frac{Q}{RT}\right) \quad (6.43)$$

$$K = K_0 \exp\left(\frac{Q}{RT}\right) \quad (6.44)$$

$$n_V = n_{V0} \exp\left(\frac{Q_n}{RT}\right) \quad (6.45)$$

$$B = B_0 \exp\left(\frac{Q_B}{RT}\right) \quad (6.46)$$

$$C = C_0 \exp\left(-\frac{Q_C}{RT}\right) \quad (6.47)$$

$$\beta = \beta_0 \exp\left(\frac{Q_\beta}{RT}\right) \quad (6.48)$$

$$E = E_0 \exp\left(\frac{Q_E}{RT}\right) \quad (6.49)$$

where R is the gas constant and T is the absolute temperature. Q , Q_n , Q_C , Q_B , Q_E , Q_β , k_0 , A , B_0 , C_0 , β_0 , K_0 , n_{V0} , φ , γ_1 , γ_2 , and γ_3 are constants to be determined from experimental data.

Equation (6.38) is the flow law, representing that plastic strain rate $\dot{\varepsilon}^P$ is a function of flow stress σ , initial elastic limit k , and isotropic hardening H , with damage ω taken into account, where the term $1/(1 - \omega)^{\gamma_1}$ is adopted to provide the equation with higher flexibility. Equation (6.39) is the isotropic hardening law formulated as a function of normalised dislocation density $\bar{\rho}$, where $\bar{\rho}$ is given by equation (6.40). The dislocation density evolution law (6.40) involves dislocation accumulation, and dynamic and static recovery. Equation (6.41) is the evolution law of plasticity-induced damage ω . Equation (6.42) is a modified Hooke's law. The unified equations (6.38) –

(6.42) are a set of non-linear ordinary differential equations that cannot be solved analytically. As discussed in section 6.2, this type of equation set can be solved with given initial values for the variables using numerical integration techniques.

6.4.2 Determination of the equations

6.4.2.1 Calibration of the constants from experimental data

The model has to be determined from fitting the computed true stress-strain curves to the corresponding experimental results by adjusting the values of constants within the equations. Two sets of values were calibrated for the austenite and initial phase of boron steels, respectively.

The forward Euler method was used for the numerical integration and trial and error was adopted based on a deep understanding of the physical base of each state variable and material constant. The real strain rates calculated from experimental results for each testing condition, instead of designed values, were input to the numerical integration code to ensure the fitting accuracy. The values of E_0 and Q_E were determined from Young's modulus values from literature [164]. For computation efficiency, the damage $\omega = 0.7$ was taken as the criterion for the failure of boron steel. The reason is that the value of stress drops sharply with ω above 0.7, which requires tiny time step for the integration and thereupon high computation cost.

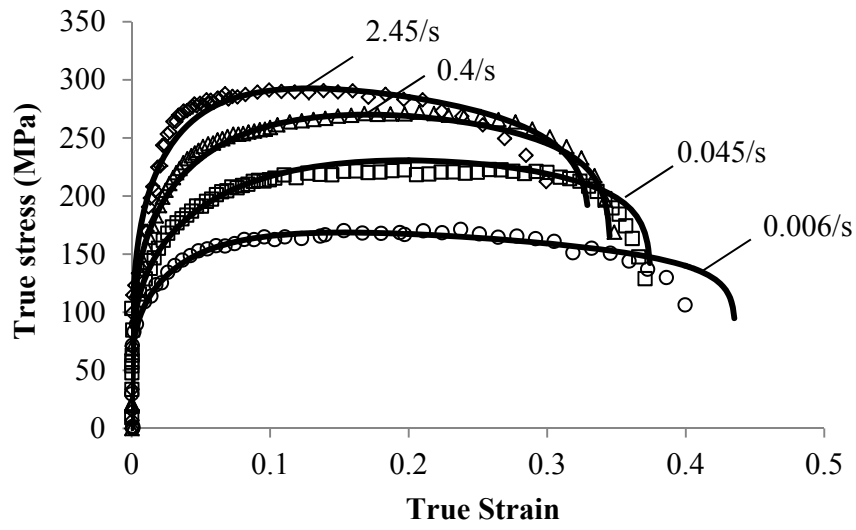
The procedure to determine the material constants mainly consists of two steps (take austenite as an example). At the first step, determine equations (6.38) – (6.42), by taking the temperature dependent parameters k , K , n_V , B , C , β , and E as constants, from fitting the true stress-strain data for different strain rates, for a deformation temperature of 973K; At the second step, by keeping the obtained values of k , K , n_V , B , C , β , and E at 973K as well as other material constants in equations (6.38) – (6.42) unchanged, adjust the 6 pairs of pre-exponent and activation energy associated constants in equations (6.43) – (6.49) to fit the true stress-strain data for different

deformation temperatures, at the strain rate 0.3–0.5/s. More robust checking can be carried out by using the constant values to predict further data sets.

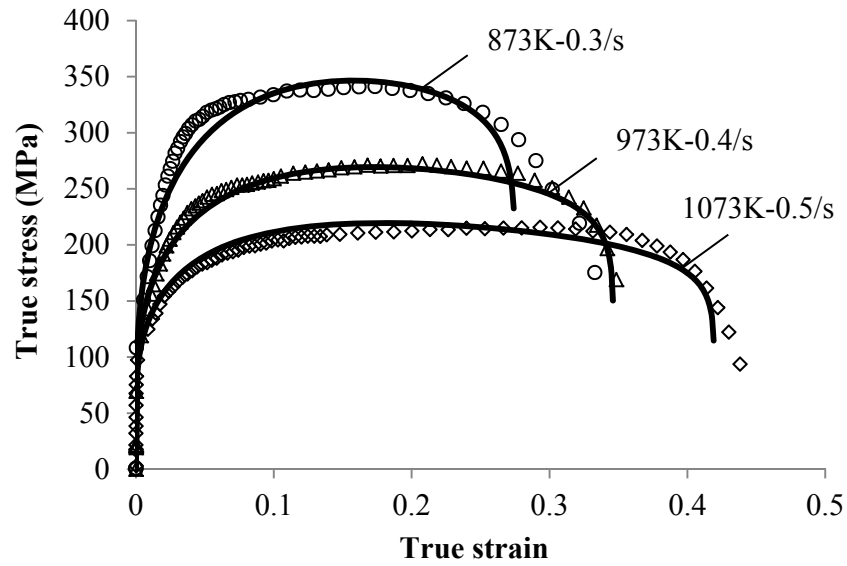
The calibrated material constants for both the austenite and initial phase of boron steels are listed in Table 6.2. Figures 6.7 and 6.8 are comparisons between experimental (symbols) and computed (solid curves) true stress-strain curves for the austenite and initial phase, respectively. Good agreement has been obtained for the austenite at all testing conditions, and for the initial phase at different strain rates. An error for initial phase at different forming temperatures can be seen in Figure 6.8 (b). This feature has been pointed out in the analysis of test results in Chapter 5 (subsection 5.3.2.2). It implies that the thermal-activated mechanisms described by Arrhenius-type equations, which are normally applied for elevated temperatures ($T > 0.5T_m$, T_m is melting temperature, about 1800K for boron steels), may not be suitable for a temperature below 823K, for the boron steel. Further improvement of the model might be needed. However, the current fit can still provide acceptable prediction of material behaviour.

Table 6.2 Material constants for equations (6.38) – (6.49) for the austenite and initial phase of boron steels

	Q (J/mol)	Q_n (J/mol)	Q_C (J/mol)	Q_B (J/mol)	Q_E (J/mol)	Q_β (J/mol)	k_0 (MPa)
Austenite	4000	50000	10000	24000	1400	8000	12.921
Initial phase	14800	1000	5000	27000	1400	7000	5.820
	A	B_0 (MPa)	C_0	E_0 (MPa)	K_0 (MPa)	R (J/mol·K)	φ
Austenite	16	12.084	0.560	143800	31.354	8.314	10.5
Initial phase	0.248	12.224	0.213	150000	24.410	8.314	13.8
	n_{V0}	n_R	γ_1	γ_2	γ_3	β_0 (MPa $^{-\gamma_3}$)	
Austenite	0.0185	0.4	3.4	1.55	0.5	5.996e-3	
Initial phase	4.33	0.4	3.1	1.54	0	0.052	

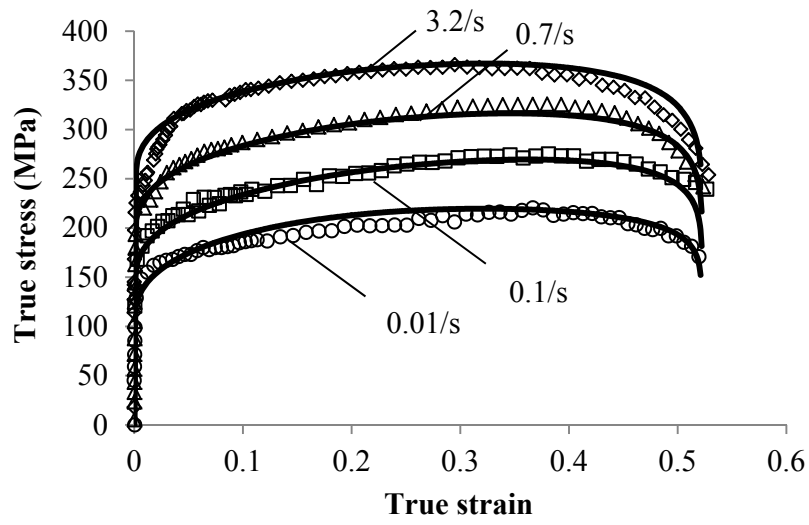


(a) Different strain rates (temperature: 973K)

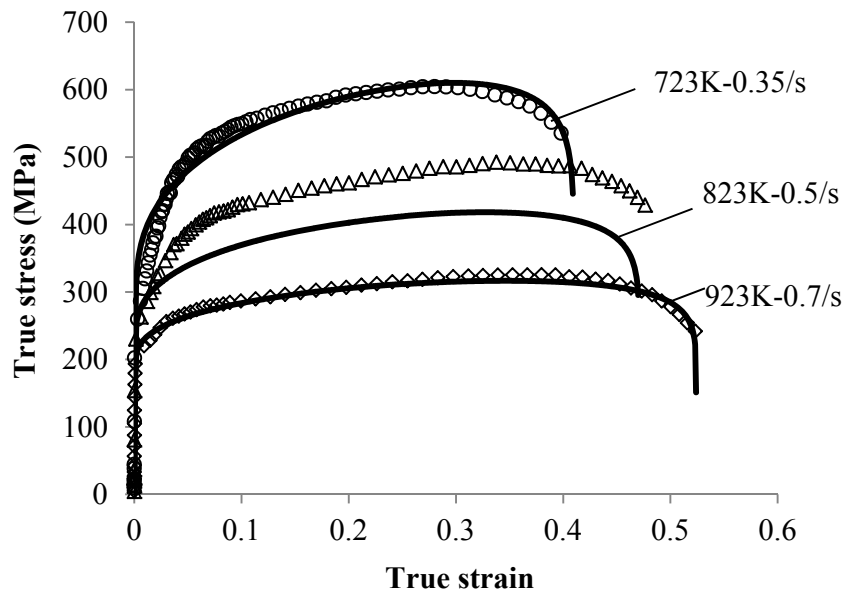


(b) Different temperatures (strain rate: 0.3–0.5/s)

Figure 6.7 Comparison of experimental (symbols) and numerical integrated (solid curves) true stress-strain curves for austenite at elevated temperatures



(a) Different strain rates (temperature: 923K)



(b) Different temperatures (strain rate: 0.35–0.7/s)

Figure 6.8 Comparison of experimental (symbols) and numerical integrated (solid curves) true stress-strain curves for the initial phase at elevated temperatures

6.4.2.2 Analysis on the modelling results

A physically-based constitutive model, as a rationalised form to describe material behaviours, can explicitly reveal the interrelationship of critical mechanisms which act to alter the flow stress response. The analysis of the modelling results here can be mapped to the previous analysis on the experimental results. Two examples are given below:

To facilitate the discussion, because the temperature dependent parameters express physical mechanics more clearly in the constitutive equations than the pre-exponent and activation energy associated constants, the values of temperature dependent parameters for austenite at the temperature of 973K and initial phase at 923K are given in Table 6.3. As discussed in Chapter 5, the initial phase is more strain rate sensitive in viscous stress at 923K than austenite at 973K. This is illustrated by the higher value of K (167.891MPa) and lower value of n_V (4.933) corresponding to 923K for the initial phase, compared with 51.405MPa and 8.934 corresponding to 973K for austenite. Also, it was found in Chapter 5 that austenite shows more pronounced static recovery, which is manifested by the higher value of C (1.927) corresponding to 973K for austenite, compared with 0.409 corresponding to 923K for the initial phase.

Table 6.3 Temperature dependent parameters for the austenite and initial phase of boron steels

	T (K)	k (MPa)	K (MPa)	n_V	C	B (MPa)	E (MPa)	β (MPa ^{-γ_3)}
Austenite	973	21.184	51.405	8.934	1.927	234.681	170965	0.016
Initial phase	923	40.030	167.891	4.933	0.409	412.108	180016	0.129

Analysis of the modelling results can assist further understanding of the mechanisms involved in deformation, and in turn proves the reliability of the model.

6.5 Unified viscoplastic-damage constitutive equations for multiphase boron steels for crashworthiness analysis

In this section, the viscoplastic-damage constitutive model introduced in section 6.3 is expanded by using a phenomenological approach to take the phase composition of material into account, so that the deformation behaviour of boron steels having various microstructures can be modelled by one single equation set. The model is capable of describing the mechanical response of boron steels being subjected to high strain rates at room temperature, which is analogous to crash situations in automobiles. The material constants of equations are calibrated from experimental data.

6.5.1 Formulation of unified viscoplastic-damage constitutive equations

Taken all temperature dependent parameters as constants, the viscoplastic-damage constitutive model can be tailored to describe the deformation behaviour of a material at room temperature. The formulation of unified constitutive equations is listed as below:

$$\dot{\varepsilon}^P = \dot{\varepsilon}^o \left(\frac{\left| \frac{\sigma}{1-\omega} \right| - k - H}{K} \right)^{n_p} \quad (6.50)$$

$$\text{If } \left| \frac{\sigma}{1-\omega} \right| - k - H \leq 0, \quad \dot{\varepsilon}^P = 0$$

$$\begin{aligned} \dot{\varepsilon}^o &= 1 \quad (\sigma > 0) \\ &= -1 \quad (\sigma < 0) \end{aligned}$$

$$\dot{\bar{\rho}} = A(1 - \bar{\rho}) \left| \dot{\varepsilon}^P \right| \quad (6.51)$$

$$H = B\bar{\rho}^{n_R} \quad (6.52)$$

$$\dot{\omega} = \beta \frac{|\dot{\varepsilon}^P|}{(1-\omega)^\varphi} \quad (6.53)$$

$$\sigma = E(1-\omega)(\varepsilon^T - \varepsilon^P) \quad (6.54)$$

Regarding the dislocation density evolution law (6.51), no static recovery is taken into account for cold working conditions.

Based on this equation set, a set of values of material constants k , K , n_V , A , B , β , and φ can be determined for any phase state of the boron steel. In order to integrate the microstructure factor into the model, so as to describe the continuum deformation of a boron steel part having graded microstructure, constants k , K , A , B , and β are expanded to phase composition dependent parameters, in terms of functions of martensite volume fraction as below:

$$k = k_0 \exp(k_x f_M) \quad (6.55)$$

$$K = K_0 + K_x f_M \quad (6.56)$$

$$A = A_0 + A_x f_M \quad (6.57)$$

$$B = B_0 + B_x f_M - k_0 \exp(k_x f_M) \quad (6.58)$$

$$\begin{aligned} \beta &= \beta_0 + \beta_{x1} f_M & (f_M \leq 60\%, f_M \geq 95\%) \\ &= \beta_0 + [\beta_{x1} + \beta_{x2}(1-f_M)] f_M & (60\% < f_M < 95\%) \end{aligned} \quad (6.59)$$

where f_M is the volume fraction of martensite phase, k_0 and k_x are yield strength associated material constants, K_0 and K_x are viscoplasticity associated material constants, A_0 and A_x are dislocation density evolution associated material constants, B_0 and B_x are work hardening associated material constants, and β_0 , β_{x1} , and β_{x2} are damage associated material constants. Equations (6.55) – (6.59) are formulated based on the experimental analysis in Chapter 5 (subsection 5.4.2.2: the effects of f_M on the mechanical properties of boron steels), by using a

phenomenological approach. For example, the yield strength k adopts the exponent fit with f_M ; the damage associated parameter β is given as a piecewise function, describing the low ductility of the steel corresponding to $f_M = 60\%$ – 95% separately.

Assuming that the phase composition dependent parameters don't change with strain rate, equations (6.50) – (6.59) can be formulated as a unified constitutive equation set, capable of modelling the dynamic deformation behaviours of boron steels having various phase compositions.

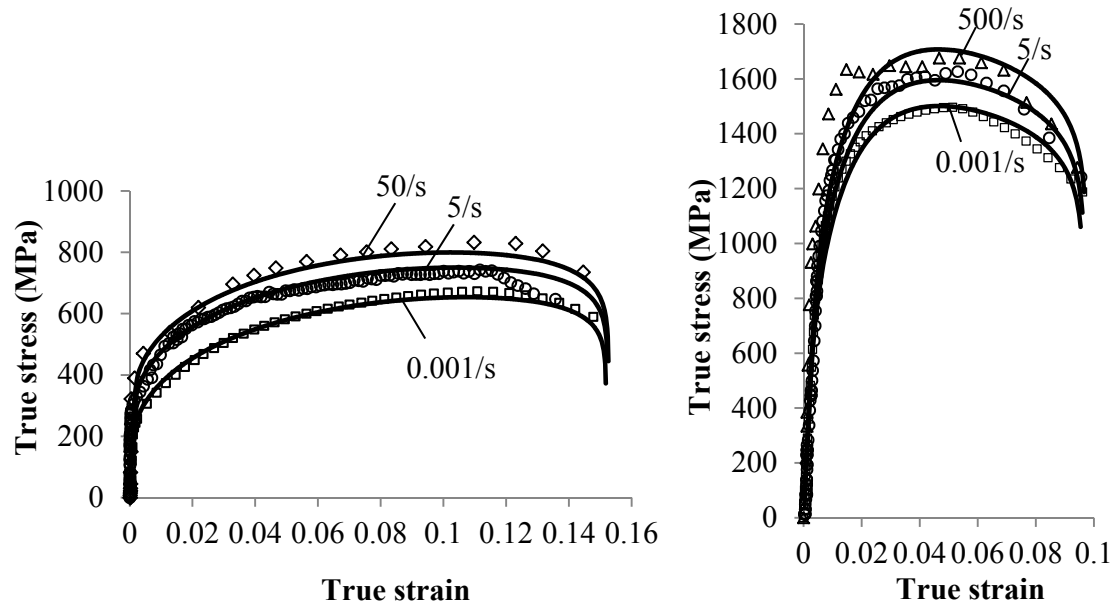
6.5.2 Determination of the equations

The material constants in equations (6.50) – (6.59) are determined by fitting the computed true stress-strain data to experimental results. Again, the non-linear ordinary differential equations were solved in terms of numerical integration by using the forward Euler method. The trial and error method was adopted.

The procedure to determine the material constants mainly consists of three steps. First, a preliminary calibration of k_0 , K_0 , A_0 , B_0 , β_0 , n_V , and φ is undertaken by fitting true stress-strain data for the initial phase ($f_M = 0\%$) at different strain rates. Second, k_x , K_x , A_x , B_x , and β_{x1} are calibrated by fitting true stress-strain data for the full martensite phase ($f_M = 100\%$) at different strain rates (Note: the value of k_x is determined by referring the experimental fit in Figure 5.22, necessary refinements for k_0 , K_0 , A_0 , B_0 , β_0 , n_V , and φ are made). Last, β_{x1} is refined and β_{x2} is determined by fitting true stress-strain data for boron steel having different volume fractions of martensite, at a strain rate of 0.001/s.

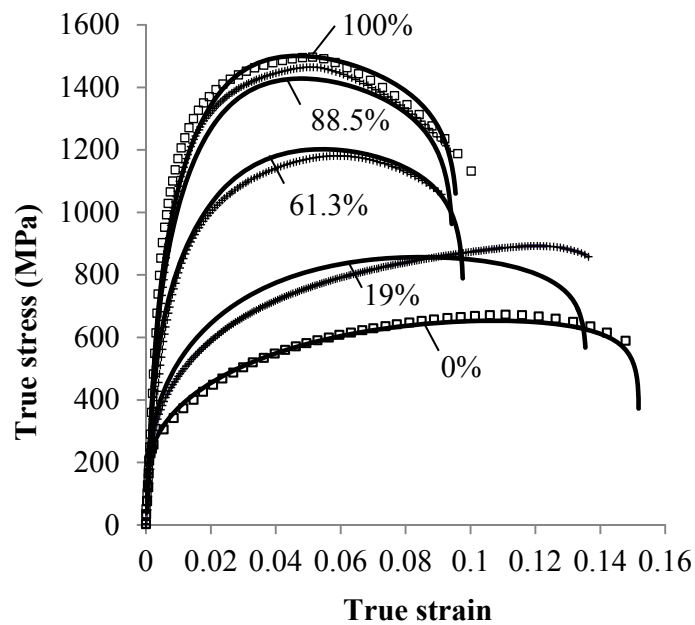
The determined material constants for boron steel are listed in Table 6.4. Figure 6.9 shows a comparison between experimental (symbols) and computed (solid curves) true stress-strain

relationships for boron steel with various phase compositions. Good agreement can be seen for all three groups of data.



(a) Different $\dot{\epsilon}$ for initial phase ($f_M = 0\%$)

(b) Different $\dot{\epsilon}$ for martensite ($f_M = 100\%$)



(c) Different martensite volume fractions, f_M (strain rate: 0.001/s)

Figure 6.9 Comparison of experimental (symbols) and numerical integrated (solid curves) true stress-strain curves for boron steels with various phase compositions at room temperature

Table 6.4 Material constants for equations (6.50) – (6.59)

k_0	K_0	A_0	B_0	β_0	φ	n_V	E
(MPa)	(MPa)		(MPa)				(MPa)
131.5	134.0	10.0	805.5	0.615	10.0	8.0	205000
k_x	K_x	A_x	B_x	β_{x1}	β_{x2}	n_R	
	(MPa)		(MPa)				
1.27	-10.0	58.0	792.0	0.431	0.5	0.5	

6.6 Summary

An austenite formation model has been developed. It is able to characterise the phase transformation process of the boron steel under both non-isothermal and isothermal conditions, where the effects of heating rate and soaking temperature on the austenite formation are rationalised. A viscoplastic-damage constitutive model is introduced. It has been adopted to model the thermo-mechanical properties of boron steels in both the austenite and initial phase states under a range of forming temperatures and strain rates; it has also been tailored and expanded to describe the deformation behaviour of boron steels with various phase compositions under a wide range of strain rates appropriate for impact crashworthiness applications. All the models have been determined from test results in Chapter 5. Good agreement between each set of experimental and predicted data has been obtained.

CHAPTER 7 CONCLUSIONS AND SUGGESTIONS FOR FUTURE WORK

7.1 Conclusions

Hot stamping of UHSS panels with graded microstructure is a promising technology to better meet safety and light weight requirements in automotive applications. A selective heating and press hardening strategy, to grade the microstructural distribution of a press hardened component by selectively heating the blank prior to forming, has been proposed and validated in this study. To enable effective process control of the hot stamping process for forming a part with optimised functional performance, comprehensive understanding and fundamental material models of the austenite formation and deformation behaviour of boron steel under hot forming conditions, as well as the dynamic response of a press hardened part with tailored properties in collision situations, have been developed, based on experimental investigations and mechanism studies. Further conclusions associated with four main aspects of the study are summarised in the following four subsections.

7.1.1 Feasibility of the selective heating and press hardening strategy

The selective heating and press hardening strategy has been successfully implemented in a hot stamping operation. Demonstrator parts, with different microstructural topographies, have been formed in good qualities without visible spring-back. Microstructural distributions in as-formed parts have been exhibited by hardness testing and SEM microscopy. The structural performance of as-formed parts under three point bending has been determined. Based on experimental results, the following conclusions have been drawn:

- Differentially heated blanks can be press hardened with high shape quality, which is essential for commercial viability of the forming process.
- Microstructural distribution in formed parts can be graded by the design of thermal conditions, which provides the basis for optimising structural properties of a part.
- The deformation mode of a part can be adjusted through microstructural arrangement; the energy absorption capacity of a part can be improved through advantageous combination of strong and ductile regions. Thereby, the potential of the selective heating and press hardening strategy in functional optimisation is demonstrated.

7.1.2 Austenite formation in boron steel during selective heating

Heat treatment tests were performed to study the formation of austenite in boron steel during selective heating in hot stamping processes. From analysis of the test results, the effects of heating rate and temperature on progress of austenite formation under both non-isothermal and isothermal conditions were investigated, and the following conclusions have been drawn:

- During the heating step, to attain a given volume fraction of austenite, a higher temperature and less time are required for a higher heating rate. Both temperature and time follow a linear relationship with heating rate, when plotted on logarithmic coordinates. The effects of heating rate are greater on temperature but less on time, for increasing austenite formation.
- The influence of heating rate remains at the same level in the subsequent isothermal (soaking) step. The time to attain given volume fractions of austenite (80%–85%, 85%–90%, and 90%–95%) all follow a linear relationship with heating rate, when plotted on logarithmic coordinates. During soaking, equilibrium can be approached in a shorter period when the heating rate is higher.

- For austenite formation during intercritical soaking situations, equilibrium can be approached in shorter period when the temperature is higher. The logarithm of time to attain a certain percentage of saturated austenite volume fraction, $80\% f_{As}$ – $90\% f_{As}$ at a chosen temperature, follows a linear relationship with inverse temperature.
- Regarding isothermal austenite formation, following a given heating rate or temperature, all evolution curves of normalised austenite volume fraction (f_A/f_{As}) follow the same form and approach equilibrium on a normalised time scale. This shows the mechanisms controlling transformation do not change with conditions, in the range of heating rate and temperature considered.
- An understanding of the austenite formation process can significantly benefit optimisation of thermal conditions in hot stamping practice and the empirical relations extracted through the analysis can provide useful information for material modelling.

A physically-based austenite formation model has been developed to describe the formation of austenite in boron steel under selective heating conditions. The equations are formulated based on three austenite formation mechanisms: nucleation, growth and impingement. The evolution rate of state variables, such as extended volume, saturated volume fraction, and real volume fraction of austenite, are modelled. The data from heat treatment experiments were used to calibrate and validate the equations. Further conclusions are listed as follows:

- The austenite formation under both non-isothermal and isothermal conditions can be described; the effects of heating rate have been taken into account for the subsequent isothermal transformation.
- Both full and partial austenite formation at γ and $(\alpha + \gamma)$ regions can be modelled.

- The determined model gives accurate predictions of the austenite formation progress, which is validated from experimental data.

7.1.3 Thermo-mechanical properties of boron steel under hot stamping

Hot tensile tests were performed to study the thermo-mechanical properties of the austenite and initial phase (78% ferrite and 22% pearlite) of boron steel. From analysis of the test results, the following conclusions have been drawn:

- For both the austenite and initial phase of the boron steel, pronounced viscoplastic properties at elevated temperatures have been observed: the stress level increases with increasing strain rate and decreasing temperature; also, ductility decreases with decreasing temperature. The strain rate effect on ductility is significant for austenite, but negligible for the initial phase.
- The strain rate dependence of flow stress (at true strain levels of 0.005, 0.05, and 0.1) approximates closely to a power law for both phase states. The temperature dependence of flow stress (at true strain levels of 0.005, 0.05, and 0.1) follows closely the Arrhenius activation energy equation for austenite.

A viscoplastic-damage constitutive model, which takes the mechanisms of dislocation-driven evolution processes such as hardening, dynamic and static recovery and damage into account, has been adopted to describe the deformation behaviour of the austenite and initial phase of boron steel under hot stamping conditions. The values of material constants in the equations corresponding to each phase state have been calibrated from the respective experimental true stress- strain data. Further conclusions are listed as follows:

- The effects of temperature and strain rate on the thermo-mechanical response of boron steel are taken into account in the model.

- The damage evolution and material failure can be modelled.
- The predicted stress-strain data show good agreement with the experimental results for the austenite at all testing conditions and for the initial phase at different strain rates. Although the fit for the initial phase at different temperatures has a small deviation, it can still provide acceptable prediction of the tensile behaviour.

7.1.4 Mechanical properties of boron steel with various microstructures at room temperature

Dynamic and quasi-static tensile tests combined with hardness testing and microstructural observation were carried out to study the mechanical properties of press hardened boron steel with various microstructures at room temperature. Based on the test results, the strain rate sensitivity of the martensite and initial phase of boron steel was analysed; the relationships between mechanical properties and phase composition for boron steel with various microstructures were rationalised. The conclusions are given as follows:

- Both the martensite and initial phase of the boron steel exhibit viscoplastic properties over a large range of strain rate (more than 5 orders of magnitude change). Initial phase shows higher strain rate sensitivity than martensite.
- With increase of martensite volume fraction in the boron steel, the hardness and true ultimate tensile strength increases proportionally and the value of 0.2% proof stress increases exponentially. A range of phase compositions for $f_M = 60\%–95\%$ corresponding to dramatically reduced ductility of the steel has been identified.

The deformation behaviour of boron steel having various microstructures has been modelled by one single viscoplastic-damage constitutive equation set. The set was developed by expanding a physically-based viscoplastic-damage model through phenomenological approaches. The values

of material constants in the equations have been calibrated from experimental data. Further conclusions are listed as follows:

- The effects of phase composition, in terms of martensite volume fraction, on the mechanical response of boron steel have been taken into account in the model.
- The model is capable of describing the mechanical response of boron steel being subjected to high strain rates (up to 500/s) at room temperature, which is analogous to collision situations in automobiles.
- Good agreement between experimental and predicted stress-strain data has been achieved.

7.2 Suggestions for future work

- Forming limit

The damage evolution in material is usually associated with stress state and strain path [156, 165]. Taking these factors into account enables better prediction of material failure, which is important for evaluating the forming limit of boron steel under hot stamping conditions. Therefore, improved modelling in the viscoplastic-damage models is recommended. Correspondingly, experimental work, such as biaxial tensile testing, to obtain more comprehensive fundamental data is necessary.

In the selective heating and press hardening process, multiple phases of boron steel are subjected to hot deformation. Both the constitutive deformation behaviour of austenite and untransformed initial phase are modelled in the current study, and it is reasonable to calculate the flow stress response in a multiple phase area using linear interpolation by knowing the volume fractions of each phase. However, damage evolution in the multiphase boron steel during hot deformation was not significantly investigated. A further study on this can be done to realise a more accurate

prediction of material failure at transition zones. This is important for identifying the application scope of the selective heating and press hardening process, in terms of part complexity.

- Phase transformation during quenching

Although significant knowledge on the phase transformation of boron steel during cooling is available in literature, all conclusions and material models are based the decomposition of a full austenite. With respect to the selective heating and press hardening process, the phase transformation of boron steel at transition regions involves austenite decomposition from multiple phase states. The influence of the other phase, ferrite, on the transformation has not as yet been identified. Investigation of this can help to identify the critical cooling rate for martensitic transformation, which is an important parameter in industrial production.

- Process simulation for function-driven-optimisation

The fundamental material models developed in this study allows the function-driven-optimisation concept to be realised. In the next stage, process simulation can be carried out by using FE commercial software, such as LS-DYNA, with the implementation of the material models via user defined subroutines.

Under given thermal conditions, the austenite distribution in a boron steel blank prior to forming can be predicted by simulating the selective heating process using the austenite formation model. Subsequently, the blank, with the information of austenite volume fraction and temperature for each element, is subjected to hot stamping in the thermo-mechanical simulation, where the deformation behaviour of the blank is described using the viscoplastic-damage model of boron steel at elevated temperatures. Provided the quenching rate is sufficient for complete martensitic transformation, the martensite distribution in the as-formed part can be known from austenite distribution. Then, the achieved part is used as an input model for functional assessment

simulation (such as crash), using the viscoplastic-damage model of boron steel at room temperature. By taking the information of martensite volume fraction and thickness for each element into account, the performance of the part is allowed to be predicted accurately. A successful simulation of the whole process will enable a proper selective heating condition to be determined for optimising structural properties of a part.

REFERENCES

1. *Information on the fuel consumption and CO₂ emissions of new cars*. 2010 [cited 2013 5 Nov]; Available from: http://europa.eu/legislation_summaries/internal_market/single_market_for_goods/motor_vehicles/interactions_industry_policies/l32034_en.htm.
2. *Passenger Car (Fuel Consumption and Co₂ Emissions) Regulations 2001*. 2001 [cited 2013 5 Nov]; Available from: <http://www.bury.gov.uk/index.aspx?articleid=2635>.
3. *Reducing CO₂ emissions from passenger cars*. [cited 2013 05 Nov]; Available from: <http://ec.europa.eu/clima/policies/transport/vehicles/cars/>.
4. *EPA, DOT unveil the next generation of fuel economy labels*. 2011 [cited 2013 5 Nov]; Available from: <http://www.greencarcongress.com/2011/05/felabel-20110525.html>.
5. Maikranz-Valentin, M., et al., *Components with Optimised Properties due to Advanced Thermo-mechanical Process Strategies in Hot Sheet Metal Forming*. Steel Research International, 2008. **79**(2): p. 92-99.
6. *World report on road traffic injury prevention*, 2004, World Health Organization.
7. Broughton, J., et al., *The numerical context for setting national casualty reduction targets*, 2000, Transport Research Laboratory.
8. Saidpour, H. *Lightweight High Performance Materials for Car Body Structures*. in *NTI Technology Conference*. 2004.
9. Kleiner, M., S. Chatti, and A. Klaus, *Metal forming techniques for lightweight construction*. Journal of Materials Processing Technology, 2006. **177**(1-3): p. 2-7.
10. Zhang, Y., et al., *Lightweight design of automobile component using high strength steel based on dent resistance*. Materials & Design, 2006. **27**(1): p. 64-68.
11. Kleiner, M., M. Geiger, and A. Klaus, *Manufacturing of Lightweight Components by Metal Forming*. CIRP Annals - Manufacturing Technology, 2003. **52**(2): p. 521-542.
12. Merklein, M. and M. Geiger, *New materials and production technologies for innovative lightweight constructions*. Journal of Materials Processing Technology, 2002. **125-126**: p. 532-536.
13. *The Advanced High-Strength Steels Application Guidelines*. [cited 2013 5 Nov]; Available from: <http://www.worldautosteel.org/projects/ahss-guidelines/>.

14. *An Advanced High-Strength Steel family car*, in *Case study: Automotive steels* 2008, World Steel Association
15. *Automotive Steel Definitions*. 2013 [cited 2013 06 Nov]; Available from: <http://www.worldautosteel.org/steel-basics/automotive-steel-definitions/>.
16. Cai, J., *Modelling of phase transformation in hot stamping of boron steel*, in *Mechanical Engineering* 2011, Imperial College London.
17. Schaeffler, D.J. *Introduction to advanced high-strength steels - Part I*. 2005; Available from: <http://www.thefabricator.com/article/metalsmaterials/introduction-to-advanced-high-strength-steels---part-i>.
18. Mori, K. and Y. Okuda, *Tailor die quenching in hot stamping for producing ultra-high strength steel formed parts having strength distribution*. CIRP Annals - Manufacturing Technology, 2010. **59**(1): p. 291-294.
19. *Sheet Metal Forming-Processes and Applications*. Hot stamping, ed. A. Naganathan and L. Penter. 2012: ASM International.
20. *Steels for hot stamping*. 2008; Available from: http://www.arcelormittal.com/automotive/sheets/E_EN.pdf.
21. ThyssenKruppSteel, *Hot press hardening manganese-boron steels MBW for ultrahigh strengths*, 2008.
22. Naderi, M., et al., *Constitutive relationships for 22MnB5 boron steel deformed isothermally at high temperatures*. Materials Science and Engineering: A, 2008. **478**(1-2): p. 130-139.
23. Merklein, M., J. Lechler, and T. Stoehr, *Investigations on the thermal behavior of ultra high strength boron manganese steels within hot stamping*. International Journal of Material Forming, 2009. **2**(1): p. 259-262.
24. Merklein, M. and J. Lechler, *Investigation of the thermo-mechanical properties of hot stamping steels*. Journal of Materials Processing Technology, 2006. **177**(1-3): p. 452-455.
25. Åkerström, P., *Modelling and Simulation of Hot Stamping*, in *Department of Applied Physics and Mechanical Engineering* 2006, Luleå University of Technology: Luleå, Sweden.
26. Gücker, E.G. and G. Berglund. *From profile hardening to custom made components*. in *1st International Conference on Hot Sheet Metal Forming of High-Performance Steel*. 2008. Kassel, Germany.

27. Parsons, C. *Innovation and Globalization as Factors of Success for Automotive Light-Weighting*. in *CAR Management Briefing Seminars*. 2012. Traverse City, Michigan USA.
28. Billur, E. and T. Altan, *Exploring the 3rd International Conference on Hot Stamping Technology Part I*. STAMPING JOURNAL, 2011(Nov/Dec 2011): p. 12-13.
29. Karbasian, H. and A.E. Tekkaya, *A review on hot stamping*. Journal of Materials Processing Technology, 2010. **210**(15): p. 2103-2118.
30. Bielz, C. and S. Hein. *The new Audi A3*. in *EuroCarBody 2012*. 2012. Bad Nauheim, German.
31. Li, N., et al. *Investigation on the mechanical properties of as-formed boron steels for optimizing process strategies in hot stamping*. in *The 14th International Conference of Metal Forming 2012*. 2012.
32. Guiles, M., et al., *Selectively annealed bumper beam*, 2008, Shape Corporation (Grand Haven, MI, US): United States.
33. Thomas, D. and D.T. Detwiler, *Microstructural optimization of automotive structures*, 2009, HONDA Motor CO., LTD.: United States.
34. Merklein, M. and T. Svec, *Hot stamping: manufacturing functional optimized components*. Production Engineering, 2013. **7**(2-3): p. 141-151.
35. Mori, K., T. Maeno, and K. Mongkolkaji, *Tailored die quenching of steel parts having strength distribution using bypass resistance heating in hot stamping*. Journal of Materials Processing Technology, 2013. **213**(3): p. 508-514.
36. Bardelcik, A., R. George, and M. Worswick, *Transition Zone Tensile Properties within a Tailored Hot Stamping*, in *SAE Technical Paper 2012-01-0531* 2012.
37. Bardelcik, A., *High Strain Rate Behaviour of Hot Formed Boron Steel with Tailored Properties*, in *Mechanical Engineering 2012*, the University of Waterloo: Waterloo, Ontario, Canada.
38. Ertürk, S., et al. *Simulation of Tailored Tempering with a ThermoMechanicalMetallurgical Model in AutoForm plus*. in *The 8th International Conference and Workshop on Numerical Simulation of 3D Sheet Metal Forming Processes*. 2011. AIP Conference Proceedings.
39. George, R., *Hot Forming of Boron Steels with Tailored Mechanical Properties*, in *Mechanical Engineering 2011*, the University of Waterloo: Waterloo, Ontario, Canada.
40. *Tailored Tempering B-pillar MBW 1500*. Available from: http://incar.thyssenkrupp.com/4_01_120_BS06_MBW1500-TT.html?lang=en.

41. Militzer, M., *Phase field modeling of microstructure evolution in steels*. Current Opinion in Solid State and Materials Science, 2011. **15**(3): p. 106-115.
42. Zhang, W., J.W. Elmer, and T. DebRoy, *Integrated modelling of thermal cycles, austenite formation, grain growth and decomposition in the heat affected zone of carbon steel*. Science and Technology of Welding and Joining, 2005. **10**(5): p. 574-582.
43. Azizi-Alizamini, H., *Austenite formation and grain refinement in C-Mn steels*, in *The Faculty of Graduate Studies (Materials Engineering)* 2010, The University of British Columbia.
44. Shtansky, D.V., K. Nakai, and Y. Ohmori, *Pearlite to austenite transformation in an Fe-2.6Cr-1C alloy*. Acta Materialia, 1999. **47**(9): p. 2619-2632.
45. Bardelcik, A., et al., *Effect of cooling rate on the high strain rate properties of boron steel*. International Journal of Impact Engineering, 2010. **37**(6): p. 694-702.
46. He, L., et al., *Research on mechanical properties of 22MnB5 steel quenched in a steel die*. Journal of Shanghai Jiaotong University (Science), 2011. **16**(2): p. 129-132.
47. *Using LS-DYNA To Model Hot Stamping*, 2009, Livermore Software Technology Corp. (LSTC).
48. Berglund, G. *The history of hardening of boron steel in northern Sweden*. in *1st International Conference on Hot Sheet Metal Forming of High-Performance Steel*. 2008. Kassel, Germany.
49. Jonsson, M. *Presshardening, from innovation to global technology*. in *1st International Conference on Hot Sheet Metal Forming of High-Performance Steel*. 2008. Kassel, Germany.
50. Altan, T., *Hot- stamping boron-alloyed steels for automotive parts, Part I: Process methods and uses*. Stamping Journal, 2006: p. 2.
51. Hein, P., *A Global Approach of the Finite Element Simulation of Hot Stamping*. Advanced Materials Research, 2005. **6-8**(2005 Trans Tech Publications): p. 8.
52. Geiger, M., M. Merklein, and C. Hoff, *Basic Investigations on the Hot Stamping Steel 22MnB5*. Advanced Materials Research, 2005. **6-8**: p. 795-804.
53. Altan, T., *Hot-stamping boron-alloyed steels for automotive parts Part I: Process methods and uses*. STAMPING 40 JOURNAL, 2006. **December** p. 40-41.
54. *BORON STEEL 22MNB5*. 2013 [cited 2013 5 Nov]; Available from: <http://www.ruukki.com/Products-and-solutions/Steel-products/Cold-rolled-steels/Hardenable-steels/Boron-steel-22MnB5>.

55. AB, S.S.S., *Docol 22MnB5 cold rolled boron steel for hardening in water or oil*, 2011.
56. Pellegrini, D., *Study on thermal and rheological parameters of high strength steels in hot forming conditions*, in *Dipartimento di Innovazione Meccanica e Gestionale* 2011.
57. Merklein, M., J. Lechler, and M. Geiger, *Characterisation of the Flow Properties of the Quenchenable Ultra High Strength Steel 22MnB5*. CIRP Annals - Manufacturing Technology, 2006. **55**(1): p. 229-232.
58. Naderi, M., et al., *A numerical and experimental investigation into hot stamping of boron alloyed heat treated steels*. Steel Research International, 2008. **79**(2008), No.2.
59. Xing, Z., J. Bao, and Y. Yang, *Numerical simulation of hot stamping of quenched boron steel*. Materials Science and Engineering: A, 2009. **499**(1-2): p. 28-31.
60. Eriksson, M., et al., *Testing and evaluation of material data for analysis of forming and hardening of boron steel components*. Modelling And Simulation In Materials Science And Engineering, 2002. **10**: p. 277–294.
61. Lin, J. and T.A. Dean, *Modelling of microstructure evolution in hot forming using unified constitutive equations*. Journal of Materials Processing Technology, 2005. **167**(2-3): p. 354-362.
62. Lin, J., et al., *Development of dislocation-based unified material model for simulating microstructure evolution in multipass hot rolling*. Philosophical Magazine, 2005. **85**(18): p. 1967 - 1987.
63. Lin, J. and Y. Liu, *A set of unified constitutive equations for modelling microstructure evolution in hot deformation*. Journal of Materials Processing Technology, 2003. **143–144**(0): p. 281-285.
64. Jahazi, M. and J.J. Jonas, *The non-equilibrium segregation of boron on original and moving austenite grain boundaries*. Materials Science and Engineering: A, 2002. **335**(1–2): p. 49-61.
65. BABU, S.S., et al., *Effect of residual boron on the microstructure of low carbon steel resistance seam welds*. Welding Journal, 1998. **77**: p. 249-253.
66. Jandová, D., *Influence of hot and warm deformation on austenite decomposition*. Journal of Achievements in Materials and Manufacturing Engineering, 2006. **18**(1-2): p. 375-378.
67. Jun, H., et al., *Effects of deformation and boron on microstructure and continuous cooling transformation in low carbon HSLA steels*. Materials Science and Engineering: A, 2006. **422**(1-2): p. 157-162.

68. Nikraves, M., M. Naderi, and G.H. Akbari, *Influence of hot plastic deformation and cooling rate on martensite and bainite start temperatures in 22MnB5 steel*. Materials Science and Engineering: A, 2012. **540**(0): p. 24-29.
69. Barcellona, A. and D. Palmeri, *Effect of Plastic Hot Deformation on the Hardness and Continuous Cooling Transformations of 22MnB5 Microalloyed Boron Steel*. Metallurgical and Materials Transactions A, 2009. **40**(5): p. 1160-1174.
70. Naderi, M., A. Saeed-Akbari, and W. Bleck, *The effects of non-isothermal deformation on martensitic transformation in 22MnB5 steel*. Materials Science and Engineering: A, 2008. **487**(1-2): p. 445-455.
71. Min, J., et al., *On the ferrite and bainite transformation in isothermally deformed 22MnB5 steels*. Materials Science and Engineering: A, 2012. **550**(0): p. 375-387.
72. Abbasi, M., A. Saeed-Akbari, and M. Naderi, *The effect of strain rate and deformation temperature on the characteristics of isothermally hot compressed boron-alloyed steel*. Materials Science and Engineering: A, 2012. **538**(0): p. 356-363.
73. Aspacher, J. *Form hardening concepts*. in *1st International Conference on Hot Sheet Metal Forming of High-Performance Steel*. 2008. Kassel, Germany.
74. Muccio, E.A., *Plastic Part Technology*. 1991, U.S.A: ASM International.
75. Billur, E., et al. *Virtual Prototyping of Hot Formed Tailored Light-weight Designs*. in *Hot Sheet Metal Forming of High-Performance Steel*. 2013. Luleå, Sweden.
76. Hein, P. and J. Wilsius, *Status and innovation trends in hot stamping of USIBOR 1500 P*. Steel Research International, 2008. **79**: p. 8.
77. Duque Múnera, D., et al., *Innovative Press Hardened Steel Based Laser Welded Blanks Solutions for Weight Savings and Crash Safety Improvements*. SAE International Journal of Materials and Manufacturing, 2009. **1**(1): p. 472-479.
78. Choi, H.-S., et al. *Development of Hot-stamped Rear Side Member with High Crash Performance Using Tailor Welded Blank*. in *4th International Conference On Hot Sheet Metal Forming of High-Performance Steel*. 2013. Luleå , Sweden.
79. Ausmann, T. *Hot Stamp Technologies - Tailored Rolled Blanks*. in *Benteler Automotive*. 2010. Detroit, Michigan, USA.
80. Vondruska, J. *Golf 7 Tech Highlights*. [cited 2013 5 Nov]; Available from: <http://www.vwvortex.com/features/technical-features/golf-7-technicalpreview/>.
81. Becker, M. and P. Kuhnel. *The body of the new BMW 3 series*. in *EuroCarBody 2012*. 2012. Bad Nauheim: Automotive Circle International.

82. Perez-Santiago, R., et al. *Hot Stamping a B-Pillar with Tailored Properties: Experiments and Preliminary Simulation Results* in *Hot Sheet Metal Forming of High-Performance Steel* 2013. Luleå, Sweden.
83. Cha, S.-H., et al. *Annealing Optimization to Make Tailored-Properties of Body-In-White Part.* in *4th International Conference On Hot Sheet Metal Forming of High-Performance Steel*. 2013. Luleå , Sweden.
84. Yi, X. and L. Mi, *Effect of Dies Temperature on Mechanical Properties of Hot Stamping Square-Cup Part for Ultra High Strength Steel* *Advanced Materials Research* 2010. **129**: p. 390-395.
85. Thomas, D.C., OH, US), Detwiler, Duane Trent (Powell, OH, US), *Microstructural optimization of automotive structures*, 2009, HONDA MOTOR CO., LTD. (Tokyo, JP): United States.
86. Deng, S., et al., *Investigations on numerical simulation of tailored tempering process based on related experiments.* *AIP Conference Proceedings*, 2013. **1532**(1): p. 924-930.
87. Bodin, H., *Method of hot stamping and hardening a metal sheet*, 2010, Gestamp Hardtech AB (Lulea, SE): United States.
88. Kolleck, R., et al., *Investigation on induction heating for hot stamping of boron alloyed steels.* *CIRP Annals - Manufacturing Technology*, 2009. **58**(1): p. 275-278.
89. Mori, K., S. Maki, and Y. Tanaka, *Warm and Hot Stamping of Ultra High Tensile Strength Steel Sheets Using Resistance Heating.* *CIRP Annals - Manufacturing Technology*, 2005. **54**(1): p. 209-212.
90. Mori, K., S. Saito, and S. Maki, *Warm and hot punching of ultra high strength steel sheet.* *CIRP Annals - Manufacturing Technology*, 2008. **57**(1): p. 321-324.
91. Ploshikhin, V., et al., *New heating technology for the furnace-free press hardening process.*
92. Kolleck, R., et al. *Alternative heating concepts for hot sheet metal forming.* in *the 1st International Conference in Hot Sheet Metal Forming of High-performance Steel*. 2008. Kassel, Germany.
93. Law, N.C. and D.V. Edmonds, *The formation of austenite in a low-alloy steel.* *Metallurgical Transactions A*, 1980. **11-A**(0360-2133/80/0111-0033): p. 33-46.
94. Molinder, G., *A quantitative study of the formation of austenite and the solution of cementite at different austenitizing temperatures for a 1.27% carbon steel.* *Acta Metallurgica*, 1956. **4**(6): p. 565-571.

95. Schmidt, E.D., E.B. Damm, and S. Sridhar, *A study of diffusion- and interface-controlled migration of the austenite/ferrite front during austenitization of a case-hardenable alloy steel*. Metallurgical and Materials Transactions A, 2007. **38A**: p. 698-715.
96. Fugarolas, D.G. and H.K.D.H. Bhadeshia, *A model for austenitisation of hypoeutectoid steels*. Journal of Materials Science, 2003. **38**(6): p. 1195 – 1201.
97. Reed, R.C., et al., *Determination of reaustenitisation kinetics in a Fe–0.4C steel using dilatometry and neutron diffraction*. Materials Science and Engineering A, 1998. **256**(1–2): p. 152-165.
98. Garcia, C.I. and A.J. Deardo, *Formation of austenite in 1.5 pct Mn steels* Metallurgical Transactions A, 1981. **12A**(0360-2133/81/0311-052): p. 521-530.
99. Yi, J.J., I.S. Kim, and H.S. Choi, *Austenitization during intercritical annealing of an Fe-C-Si-Mn dual-phase steel*. Metallurgical Transactions A, 1985. **16A**: p. 1237-1245.
100. Yang, J.R. and H.K.D.H. Bhadeshia, *Reaustenitization experiments on some high-strength steel weld deposits*. Materials Science and Engineering A, 1989. **118**: p. 155-170.
101. Martín, D.S., et al., *A contribution to the modelling of the austenitisation process in steels, in METAL 2006*2006: Hradec nad Moravicí.
102. Khaira, H.K., A.K. Jena, and M.C. Chaturved, *Effects of heat treatment cycle on equilibrium between ferrite and austenite during intercritical annealing*. Materials Science and Engineering A, 1993. **161**: p. 267-271.
103. Thibaux, P., A.M. Tenier, and C. Xhoffer, *Carbon diffusion measurement in austenite in the temperature range 500C to 900C*. Metallurgical and Materials Transactions A, 2007. **38A**: p. 1169-1176.
104. Asadi Asadabad, M., M. Goodarzi, and S. Kheirandish, *Kinetics of austenite formation in dual phase steels*. ISIJ International, 2008. **48**(9): p. 1251–1255.
105. Caballero, F.G., C. Capdevila, and C. Garcí'a de Andre's, *Influence of scale parameters of pearlite on the kinetics of anisothermal pearlite to austenite transformation in a eutectoid steel*. Scripta mater., 2000. **42**: p. 1159–1165.
106. Surm, H., et al., *Modelling the ferrite/carbide austenite transformation of hypoeutectoid and hypereutectoid steels*. J. Phys. IV France, 2004. **120**: p. 111-119.
107. Oliveira, F.L.G., M.S. Andrade, and A.B. Cota, *Kinetics of austenite formation during continuous heating in a low carbon steel*. Materials Characterization, 2007. **58**(3): p. 256-261.

108. Illescas, S., J. Fernández, and J.M. Guilemany, *Kinetic analysis of the austenitic grain growth in HSLA steel with a low carbon content*. Materials Letters, 2008. **62**(20): p. 3478-3480.
109. SAVRAN, V.I., *Austenite formation in C-Mn steel*, in *Materials Science and Technology* 2009, the Delft University of Technology.
110. Borgenstam, A., et al., *On the symmetry among the diffusional transformation products of austenite*. Metallurgical and Materials Transactions A, 2010. **42A**: p. 1558-1574.
111. Luo, H., et al., *Experimental and numerical analysis on formation of stable austenite during the intercritical annealing of 5Mn steel*. Acta Materialia, 2011. **59**(10): p. 4002-4014.
112. Gaude-Fugarolas, D. and H.K.D.H. Bhadeshia, *A model for austenitisation of hypoeutectoid steels*. Journal of Materials Science, 2003. **38**: p. 1195 – 1201.
113. Caballero, F.G., C. Capdevila, and C. Garcí'a de Andre's, *Modelling of kinetics and dilatometric behaviour of austenite formation in a low-carbon steel with a ferrite plus pearlite initial microstructure*. Journal of Materials Science 2002. **37** p. 3533 – 3540.
114. Cai, J., et al., *Austenitization mechanisms and modelling methods for steels*. World Journal of Engineering, 2008. **5**(1): p. 10-20.
115. Lee, S.J., D.K. Matlock, and C.J. Van Tyne, *An empirical model for carbon diffusion in austenite incorporating alloying element effects*. ISIJ International, 2011. **51**(11): p. 1903–1911.
116. Parris, D.C. and R.B. McLellan, *The diffusivity of carbon in austenite*. Acta Metallurgica, 1976. **24**(6): p. 523-528.
117. Speich, G.R., V.A. Demarest, and R.L. Miller, *Formation of austenite during intercritical annealing of dual-phase steels*. Metallurgical Transactions A, 1981. **12**(8): p. 1419-1428.
118. Chen, H., et al., *A JMAK-like approach for isochronal austenite–ferrite transformation kinetics in Fe–0.055 wt-%N alloy*. Materials Science and Technology, 2010. **26**(5): p. 572-578.
119. Liu, F., et al., *Analysis of solid state phase transformation kinetics: models and recipes*. International Materials Reviews, 2007. **52**(4): p. 193-212.
120. Savic, V. and L. Hector, *Tensile Deformation and Fracture of Press Hardened Boron Steel using Digital Image Correlation*, in *SAE Technical Paper* 2007. p. 2007-01-0790.

121. Bardelcik, A., et al. *High Strain Rate Properties of Hot Formed Die Quenched Boron Steel*. in *the 3rd International Conference in Hot Sheet Metal Forming of High-performance Steel* 2008. Luleå, Sweden.
122. Bardelcik, A., et al., *A strain rate sensitive constitutive model for quenched boron steel with tailored properties*. International Journal of Impact Engineering, 2012. **50**(0): p. 49-62.
123. Kortenaar, L.t., et al. *The effect of stress triaxiality on the failure response of boron steel quenched to a martensitic and bainitic material condition* in *the 3rd International Conference in Hot Sheet Metal Forming of High-performance Steel*. 2013. Luleå, Sweden.
124. Li, Y., S.H. An, and C.G. Kang, *Investigation on Mechanical Properties of Boron Steel for Variation of Quenching Temperature and its Hot Press Forming Simulation*. AIP Conference Proceedings, 2010. **1252**(1): p. 949-955.
125. Smerd, R., et al., *High strain rate tensile testing of automotive aluminum alloy sheet*. International Journal of Impact Engineering, 2005. **32**(1–4): p. 541-560.
126. Xiao, X. and M. Leach, *Intermediate and High Strain Rate Tensile Testing of Plastic Materials*, in *2005 SEM Annual Conference & Exposition on Experimental and Applied Mechanics* 2005, Society for Experimental Mechanics, Inc. p. 8.
127. Wood, P.K.C., et al., *A model to describe the high rate performance of self-piercing riveted joints in sheet aluminium*. Materials & Design, 2011. **32**(4): p. 2246-2259.
128. Xiao, X., *Dynamic tensile testing of plastic materials*. Polymer Testing, 2008. **27**(2): p. 164-178.
129. Raisch, S.R. and B. Möglinger, *High rate tensile tests – Measuring equipment and evaluation*. Polymer Testing, 2010. **29**(2): p. 265-272.
130. Borsutzki, M., et al., *Recommendations for Dynamic Tensile Testing of Sheet Steels*, 2005, International Iron and Steel Institute.
131. Wang, Q., et al., *Three-dimensional investigation of the dynamics of a propane diffusion flame*. Fuel, 2013. **116**.
132. Crammond, G., S.W. Boyd, and J.M. Dulieu-Barton, *Speckle Pattern Characterisation for High Resolution Digital Image Correlation*. Applied Mechanics and Materials, 2011. **70**: p. 261-266.
133. Hooper, P., *Blast performance of silicone - bonded laminated glass*, in *Department of Mechanical Engineering* 2011, Imperial College London.

134. Garcia de Andrés, C., et al., *Application of dilatometric analysis to the study of solid–solid phase transformations in steels*. Materials Characterization, 2002. **48**(1): p. 101-111.
135. William D. Callister, J., *Fundamentals of Materials Science and Engineering*. Second Edition ed. 2005: John Wiley & Sons, Inc.
136. Reed, R.C., et al., *Determination of re-austenitisation kinetics in a Fe–0.4C steel using dilatometry and neutron diffraction*. Materials Science and Engineering A, 1998. **256**(1–2): p. 152-165.
137. Su, B., et al., *Numerical simulation on austenitization of cast steel during heating process*. IOP Conference Series: Materials Science and Engineering, 2012. **33**(012080).
138. Lemaitre, J. and J.-L. Chaboche, *Mechanics of solid materials*. 1994: Cambridge: Cambridge University Press.
139. Lin, J., T. Dean, and Y. Liu, *A Review on Damage Mechanisms, Models and Calibration Methods under Various Deformation Conditions*. International Journal of Damage Mechanics, 2005. **14**(4): p. 299-319.
140. Bruce, D.M., *Dynamic tensile testing of sheet steels and influence of strain rate on strengthening mechanisms in sheet metals*, 2003.
141. Mohamed, M.S.K., *An investigation of hot forming quench process for AA6082 aluminium alloys*, in *Mechanical Engineering 2010*, Imperial College London.
142. Foster, A.D., et al., *A stress state dependent damage model for the high temperature failure of free-cutting steels*. Journal of Multiscale Modelling, 2009. **1**: p. 369-387.
143. Avramovic-Cingara, G., et al., *Void Nucleation and Growth in Dual-Phase Steel 600 during Uniaxial Tensile Testing*. Metallurgical and Materials Transactions A, 2009. **40**(13): p. 3117-3127.
144. Larour, P., *Strain rate sensitivity of automotive sheet steels-influence of plastic strain, strain rate, temperature. microstructure, bake hardening and pre-strain*, 2010, Diss. Universitätsbibliothek.
145. Taouche, R. and N. Rouag, *Optimization of stress-strain behavior parameters by genetic algorithms method: Application to soft-matrix two-phase alloys*. Computational Mechanics, 2003. **30**(4): p. 297-302.
146. Avramovic-Cingara, G., et al., *Effect of martensite distribution on damage behaviour in DP600 dual phase steels*. Materials Science and Engineering: A, 2009. **516**(1–2): p. 7-16.

147. Sarwar, M. and R. Priestner, *Influence of ferrite-martensite microstructural morphology on tensile properties of dual-phase steel*. Journal of materials science, 1996. **31**(8): p. 2091-2095.
148. Adamczyk, J. and A. Grajcar, *Heat treatment and mechanical properties of low-carbon steel with dual-phase microstructure*. Journal of Achievements in Materials and Manufacturing Engineering, 2007. **22**(1): p. 13-20.
149. Matlock, D.K., G. Krauss, and F. Zia-Ebrahimi, *Strain Hardening of Dual-Phase Steels: An Evaluation of the Importance of Processing History*. Deformation, Processing, and Structure, ed. G. Krauss. 1984, Ohio: ASM.
150. Krauss, G., *Steels: Heat Treatment and Processing Principles*. 1993: ASM International.
151. Kadkhodapour, J., A. Butz, and S. Ziaei Rad, *Mechanisms of void formation during tensile testing in a commercial, dual-phase steel*. Acta Materialia, 2011. **59**(7): p. 2575-2588.
152. Masaharu Kato, T.F., Susumu Onaka, *Effects of shape and volume fraction of second phase on stress states in two-phase materials*. Materials Science and Engineering: A, 2000. **285**(1): p. 144-150.
153. Marzbanrad, J., M. Alijanpour, and M.S. Kiasat, *Design and analysis of an automotive bumper beam in low-speed frontal crashes*. Thin-Walled Structures. **47**(8-9): p. 902-911.
154. Bower, A.F., *Applied Mechanics of Solids*. 2012: CRC Press.
155. Lin, J., et al., *On microdamage in hot metal working Part 2: Constitutive modelling*. Engineering Transactions, 2007. **55**: p. 1-18.
156. Foster, A.D., *Modelling damage evolution during the hot deformation of free machining steels*, in *Mechanical and Manufacturing Engineering*2007, The University of Birmingham.
157. Cai, J., *Modelling of phase transformation in hot stamping of boron steel*, in *Mechanical Engineering*2011, Imperial College London.
158. Lardner, R.W., *Mathematical theory of dislocations and fracture*. 1974, Toronto: University of Toronto Press.
159. Gillis, P.P. and J.M. Kelly, *An ideally viscoplastic analysis of the yield point phenomenon*. Acta Materialia, 1973. **21**: p. 343-346.
160. Bai, Q., *Development of a New Process for High Precision Gas Turbine Blade Forging*, in *Mechanical Engineering*2012, Imperial College London.

161. Dunne, F.P.E., D.R. Hayhurst, and J. Lin, *Physically-based temperature dependence of elastic-viscoplastic constitutive equations for copper between 20 and 500C*. Philosophical Magazine A, 1996. **74**: p. 359-382.
162. Nes, E., *Modelling of work hardening and stress saturation in FCC metals*. Progress in Materials Science, 1997. **41**(3): p. 129-193.
163. H, L., et al., *Modelling mechanical property recovery of a linepipe steel in annealing process*. International Journal of Plasticity, 2009. **25**: p. 1049–1065.
164. *Young Modulus of Elasticity for Metals and Alloys*. [cited 2012; Available from: http://www.engineeringtoolbox.com/young-modulus-d_773.html].
165. Tasan, C.C., J.P.M. Hoefnagels, and C.H.L.J.t. Horn. *Strain Path Dependent Ductile Damage Mechanics and Forming limits*. Available from: http://www.tatasteelautomotive.com/file_source/StaticFiles/Automotive/Strain%20Path%20Dependent%20Ductile%20Damage.pdf.

APPENDIX 1 CALCULATION OF AUSTENITE VOLUME FRACTION

A method has been developed to calculate the volume fraction of austenite from the experimentally measured ΔW . Referencing the natural strain definition, the relative volume change during the thermal-expansion/contraction and phase transformation can be expressed as:

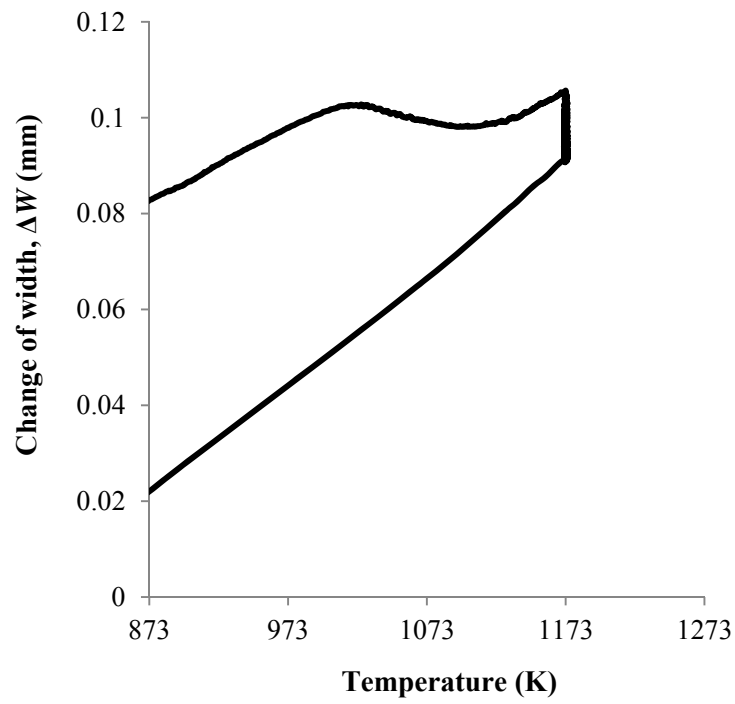
$$v = \ln \frac{V}{V_0} \quad (\text{A1.1})$$

where V_0 is the initial volume of the specimen, and V is the volume at any time during the thermal cycle.

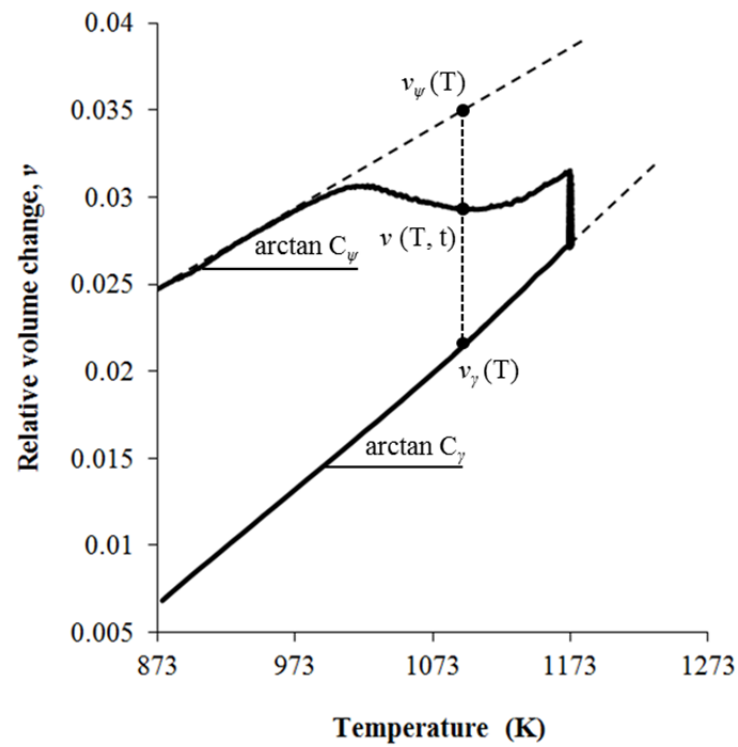
Assuming that the specimen expands isotropically, i.e. $v = W^3$, the relative volume change can thus be related to ΔW as follows:

$$v = 3 \ln \frac{W}{W_0} = 3 \ln \left(\frac{\Delta W}{W_0} + 1 \right) \quad (\text{A1.2})$$

Based on Equation (A1.2), the width change curve can be converted to a relative volume change curve. An example, for the test condition of heating rate 5K/s and soaking temperature 1173K, is given in Figure A1.1.



(a) The width change against temperature



(b) The relative volume change against temperature

Figure A1.1 Conversion from width change curve to relative volume change curve

Regarding the pure thermal expansion and contraction stages, the following relationship is proposed:

$$v_{\psi}(T) = v_{\psi 0} + C_{\psi} \Delta T; \quad v_{\gamma}(T) = v_{\gamma 0} + C_{\gamma} \Delta T \quad (\text{A1.3})$$

where $v_{\psi 0}$ and $v_{\psi}(T)$ are the relative volume change of the initial phase (ferrite and pearlite mixed microstructure, represented by ψ in this study) at 873K and any temperature T , respectively. $v_{\gamma 0}$ and $v_{\gamma}(T)$ are the relative volume change of austenite phase (γ) at 873K and any temperature T , respectively. ΔT is the temperature increment from 873K. C_{ψ} and C_{γ} are the thermal expansion coefficients of the material with the initial phase mixture and austenite. Corresponding to the slopes of the linear regions in Figure A1.1 (b), they have been measured as: $C_{\psi} = 4.41056 \times 10^{-5} / \text{K}$, $C_{\gamma} = 6.82215 \times 10^{-5} / \text{K}$.

Regarding the phase transformation stage, the relative volume change, which is the function of both temperature and time, can be given as:

$$v(T, t) = (1 - f_A) v_{\psi}(T) + f_A v_{\gamma}(T) \quad (\text{A1.4})$$

where f_A is the volume fraction of austenite. Thus the extent of phase transformation can be calculated as:

$$f_A = \frac{v_{\psi}(T) - v(T, t)}{v_{\psi}(T) - v_{\gamma}(T)} \quad (\text{A1.5})$$

where $v_{\psi}(T)$ and $v_{\gamma}(T)$ are calculated according to equation (A 1.3), and $v(T, t)$ is obtained from the relative volume change-temperature curve in Figure A1.1 (b). Based on Equations (A1.2), (A1.3), (A1.5), the dilatometric curves can be transformed to austenite volume fraction curves.

APPENDIX 2 STRAIN CORRECTION AT NECKING

STAGE

For tensile testing, when failure doesn't occur at the specimen centre section where the dilatometer is clamped, the strain obtained from dilatometer measurement cannot accurately present the deformation behaviour of specimen after onset of necking. Therefore, a method has been defined to correct measured strain data to represent that at the necking position.

Figure A2.1 schematically shows the longitudinal area of interest between the centre section and failure section of a tensioned specimen. At the time just before onset of necking (at the peak load), the area has a rectangular shape (light grey). The specimen width and the distance between centre section and failure section are W_{c0} and l_0 , respectively. When localised deformation takes place, the shape of the area deviates from rectangular, and in this method, it is simplified as a trapezium: the trapezium drawn in dashed lines represents an instantaneous shape during necking, where the widths of centre section and failure section are W_{ci} and W_{fi} , respectively, and the distance between centre section and failure section is l_i ; the trapezium in dark grey represents the final shape of the area when the specimen fails, where the corresponding dimensions are W_{cn} , W_{fn} , and l_n . The angle α represents the deviation of specimen edge from its original direction. It equals zero in the beginning, and for a constant strain rate, it is assumed to increase proportionally with time during necking.

The target is to map the evolution of W_{ci} to W_{fn} , thus the corrected true strain at necking stage can be given by:

$$\varepsilon_T = -2\ln\left(\frac{W_{fn}}{W_0}\right) \quad (\text{A2.1})$$

where W_0 is the initial width of specimen. The calculation of W_{fi} is given in detail as follows:

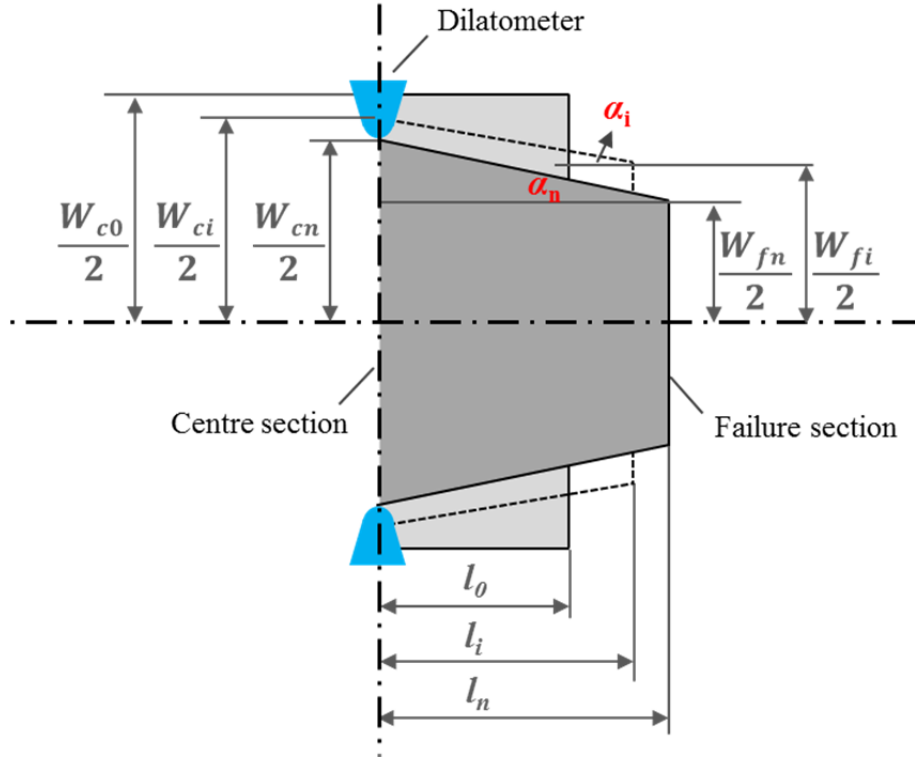


Figure A2.1 Strain correction method at necking stage

The instantaneous width of the failure section W_{fi} can be formulated as:

$$W_{fi} = W_{ci} - 2l_i \tan \alpha_i \quad (\text{A2.2})$$

where W_{ci} is obtained from dilatometer measurement, and

$$l_i = l_0 + \frac{i}{n}(l_n - l_0) \quad (\text{A2.3})$$

$$\alpha_i = \frac{i}{n} \alpha_n \quad (\text{A2.4})$$

where n is the total number of time intervals for the necking stage in data acquisition, i represents an instantaneous time interval.

Regarding equation (A1.2), l_0 is given by:

$$l_0 = l_n \frac{S_0}{S_n} \quad (\text{A2.5})$$

where S_0 and S_n correspond to the strokes (data from Gleeble data acquisition) at the onset of necking and failure, respectively. The value of l_n can be manually measured from the fractured specimen.

Regarding equation (A1.3), the final angle α_n can be calculated by:

$$\alpha_n = \arctan \frac{W_{cn} - W_{fn}}{2l_n} \quad (\text{A2.6})$$

where W_{cn} is read from dilatometer measurement, W_{fn} and l_n are manually measured from the fractured specimen.

Figure A2.2 is an example showing the true stress-strain curves before and after correction. A correct failure strain and improved flow stress accuracy can be ensured by using the method.

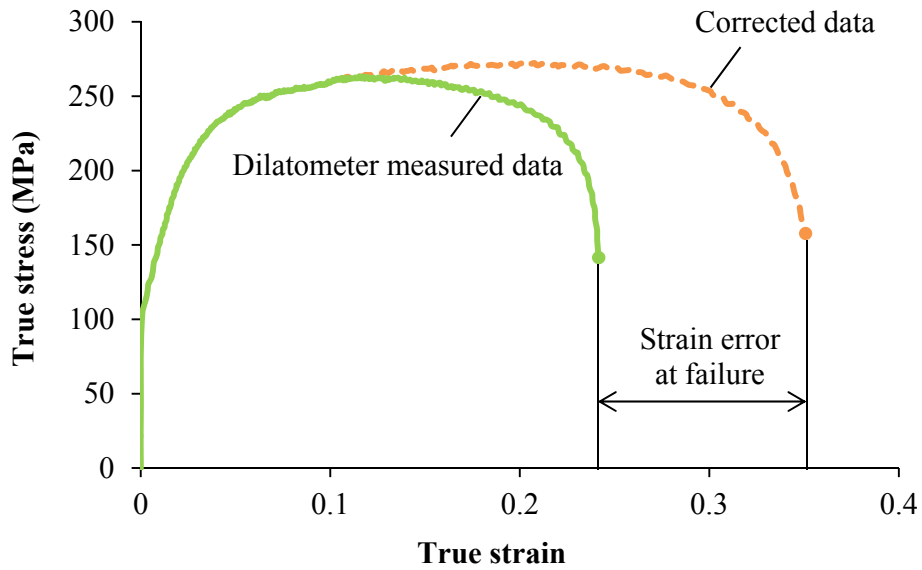


Figure A2.2 An example true stress-strain curve showing the correction at necking stage